Fall 2021

Development of Acoustic Metamaterial Noise Barriers and Simultaneously Harvesting Energy Using Smart Materials

Fariha Mir

DEVELOPMENT OF ACOUSTIC METAMATERIAL NOISE BARRIERS AND SIMULTANEOUSLY HARVESTING ENERGY USING SMART MATERIALS

by

Fariha Mir

Bachelor of Science
Military Institute of Science and Technology, Bangladesh, 2014

Master of Science
University of South Carolina, 2019

Submitted in Partial Fulfillment of the Requirements

For the Degree of Doctor of Philosophy in

Mechanical Engineering

College of Engineering and Computing

University of South Carolina

2021

Accepted by:

Sourav Banerjee, Major Professor

Lingyu Yu, Committee Member

Tanvir Farouk, Committee Member

Juan Caicedo, Committee Member

Tracy L. Weldon, Interim Vice Provost and Dean of the Graduate School

Dedication

This work is dedicated to my parents Mir Imdadul Haque and Syeda Afsana Ahsan. I would also like to dedicate it to my husband Ahmed Shehab Khan and our daughter Ruzainah Manha Khan.

Acknowledgements

I would like to express my sincere appreciation and respect to my advisor Dr. Sourav Banerjee for his cordial support and valuable advice in my research. I also would like to thank all the members of iMAPS for their continuous help and support. Finally, I would like to thank my husband, daughter, and my parents for their support, constant encouragement, and unconditional love for me.

Abstract

In our surroundings abundant energy, we either feel through component vibration or hear noises from acoustic sources. Harvesting these unused and untapped green energy in the form of ambient vibration, and acoustic sounds is an emerging field of research in recent years. Utilization of the energy within a wide band of the frequency spectrum originated from the vibrational sources alone stands as one of the most promising ways to power small electronic devices, smartphones, local structural health monitoring sensors, home, and workshop appliances. These abundant sources of green energy are available in almost all the engineering industries, workshops, manufacturing facilities, construction zones, and in our daily operations. Particularly aerospace, mechanical, and civil sectors have plenty of such scenarios where the energy used is lost through vibration and acoustic noises. Continuously running machinery in a workshop, ambient vibration in a manufacturing facility, vibrating wings of an aircraft, high dB aircraft noise near airports, noise in metallurgical plants, power plants, vehicle noise near a roadside facility, etc. are few examples of the ambient source of energy that can be harvested which are otherwise wasted. If a suitable mechanism is devised, the vibration and acoustic noise sources can be equipped to trap and reclaim the energy to create local power sources.

Researchers proposed many such methods in the past two decades. However, only recently researchers including us proposed that carefully engineered metamaterials can also be used for energy harvesting. Metamaterials are man-made materials that behave uniquely

and possess exclusively desired properties that are not found in natural materials. Usually, it is the combination of two or more materials and can be engineered to perform specific tasks that are not possible with traditional materials. These were initially discovered in photonics while working with electromagnetic radiation. An electromagnetic counterpart of wave propagation in mechanics, i.e. phononics with acoustic waves were found to be affected by the metamaterials. These acoustic metamaterials when carefully designed are also capable of affecting the wave propagation characteristics through fluids such as air. Many acoustic metamaterials have gone beyond its definition but still, characterize the waveguiding properties. They are classified under the passive modalities of acoustics to affect the sound and vibration mitigation. Incorporation of smart materials while constructing acoustic metamaterial, can enhance the multifunctionality of these materials in both passive and active ways. A prospective application field for such acoustic metamaterials is energy harvesting from low-frequency vibrations. Conventionally, passive acoustic metamaterials are visualized as noise barrier materials to filter roadside and industrial noises. This application can get extended to the aerospace application where mitigation of engine noise inside the cabin is challenging. Irrespective of their target applications, acoustic metamaterials integrated with smart materials can scavenge the very green energy that they are designed to absorb and mitigate.

First, in this research work, a recently proposed method of creating Acoustoelastic Metamaterial (AEMM) is used to investigate further if that can be used to harvest energy from the industrial noise barriers. It is known that noise barriers are designed to minimize noise outside the boundary like the noise barriers seen beside the highways. Construction materials like concrete, steel, vinyl, wood, or earth mounds are used in the industrial sound

barriers that can reduce the sound pressure level (dB) on the other side of the barriers. In this work, a novel metamaterial wall (MetaWall) is proposed to redefine the industrial sound isolation wall using the integrated AEMM units. In this part, wave isolation and energy harvesting capabilities of the acoustic metamaterial is fused to propose MetaWall unit bricks, which are made of rubber-metal-concrete composite, as an industrial building material.

Secondly, it is proposed that such acousto-elastic metamaterial (AEMM) models can also be used in the aerospace industry to power the online NDE/SHM sensors, e.g. piezoelectric wafer active sensors which are widely used. Hence, further in this part, a rigorous study is made to find the actual power required by the online NDE / SHM sensors such that a similar amount of power can be harvested by the AEMM model and stored in a battery for scheduled scans. The ultimate goal of this second study is to minimize the size of the proposed AEMM model to make it suitable for aerospace applications on-board. With changes in the materials of the cell constituents, it is shown that the power outputs from a similar model can be significantly altered and further optimized. A parametric study is also performed to show the variation of the output power. Finally, based on the learning a plate-type metamaterial is proposed to harvest a required optimum amount of energy from the ambient vibration with dominant frequency as low as 100Hz.

In the third section, a spiral-shaped acoustic metamaterial is proposed which has dual functionality of noise filtering and energy harvesting over a wider range of frequencies. A work in progress presented with a proposed timeline to complete the dissertation. This acoustic metamaterial has a comparatively high reflection coefficient closer to the anti-resonance frequencies, resulting in high sound transmission loss. The filtered noise is

trapped inside the cell in the form of strain energy. The spiral design is also sensitive to the vibration due to trampoline shaped in highly flexible polymeric piezoelectric material attachments inside the cell. This also makes it capable of harvesting energy using vibration. This is a promising acoustoelastic metamaterial with multifunctionality properties for future applications.

Hence, it is claimed that if metamaterials are employed to reduce or suppress the noise and make use of the trapped energy which is any way wasted could be harvested to power the local electronic devices. The new solution could make a transformative impact on the 21st century's green energy solutions. Calculated placement of smart materials in the cell-matrix can help to extract the strain energy in the form of power. The acoustic metamaterial cell designs presented in this research have the capability of isolating noise and reducing diffraction by trapping sound in a wide range of frequencies and at the same time recover the trapped abundant energy in the form of electrical potential using piezoelectric materials.

Table of Contents

List of Tables

List of Figures

CHAPTER 1

Introduction

1.1. Background

A worldwide spike in industrialization has led to an increasing amount of noise and now reached to the level of noise pollution. Noise pollution is termed as the unwanted propagation of noise creating physiological problems. Airborne sound travels through the air and it can transmit, reflect, or be absorbed by an obstruction. At times, it gets difficult to track sound since it is invisible. As a result, the methods and instruments used to track, and filter sound is difficult to develop. Hence, constant research is being carried out at various scales to treat such sound-related problems. Innovative and efficient noise barrier materials are being designed to filter unwanted noise in various environments and reduce noise pollution.

Energy is a vital element in the growth of modern society. From a light bulb to outer space missions, we need energy everywhere. Some energy is visible to us, such as light, but most of the existing energies in nature are not visible. Among all these, electric energy is the most used form. Due to the high electricity demand, measures are being taken to convert other forms of energy to electricity. The process which derives energy from external sources is called Energy Harvesting. Converted energy can be stored in a capacitor or battery for later use. This stored energy could work as a power source for low energy

electronics. Interest in converting ambient vibration energy into power has increased dramatically in the last few years. The goal of such research is to power wireless remote sensors which are usually powered by batteries. Batteries have a finite lifespan which creates problems with frequent replacement during emergencies. In some situations, it is not feasible to replace batteries. So, in these situations, if ambient energy in the atmosphere can be utilized to harvest electric potential to power these batteries concurrently, then most of the existing problems could be solved. Various transduction mechanisms can be employed to harvest such kind of energy. One of these is the use of piezoelectric materials to harvest energy from the unused, trapped, or lost vibration energy of the host structure.

Not only ambient vibration but also the sound and noise created by the modern machinery and vehicles can be used to harvest energy by trapping them in a medium. In recent years road traffic has increased tremendously. It is without any doubt, one of the most widespread sources of noise annoyance. Industries with heavy machinery also introduce a significant amount of noise into the atmosphere. Acoustic noise barriers can be developed to reduce the outbreak of such unwanted noise. But the efficiency of these barriers is a question for a long time. Researchers are working to improve the efficiency of the barriers, but till now the maximum reported efficiency of noise barriers is around ~50%. Concerning the traditional industrial barriers, new materials and designs are combined to create a more effective noise filtering system. Sound-absorbing materials are being used to trap the sound inside the material and decrease the reflection of noise. The law of conservation of energy states that energy can neither be created nor destroyed - only converted from one form of energy to another. So the energy that the sound barriers absorb, is trapped inside the cells. This trapped energy is not being used anywhere. If measures can

be taken to use this trapped acoustic energy in certain ways, then this can be an energy harvesting source too.

For all these special applications, conventional materials don't show much promising output. So, metamaterials can be used for such applications. ***Metamaterials*** are engineered materials that possess unique properties that cannot be found in naturally occurring materials. Metamaterials can be constructed by assembling multiple materials or polymers. The properties of the metamaterial are different from the constitutional material properties and they originate from the design assembly of the pieces. ***Acoustic metamaterials*** are kinds of metamaterials designed to control, direct, and manipulate sound waves as these might arise in gases, liquids, and solids. The acoustic metamaterial follows the theory and outcome of negative index material. Since the acoustic metamaterial is one of the branches of the metamaterials, the basic. The principle of the acoustic metamaterials is similar to the principle of metamaterials. These metamaterials usually gain their properties from structure rather than composition, using the inclusion of small inhomogeneities to enact effective macroscopic behavior. A negative refractive index of acoustic materials can be attained by altering the bulk modulus and mass density.

When we talk about using metamaterials to work as noise absorbers, we should consider what is the safe level of sound and how much sound needs to be filtered by the metamaterial in a noisy environment. The unit that measures the amount of sound is known as ***Decibel(dB).*** Decibel is the unit used to measure sound on a logarithmic scale. It is a logarithmic way of expressing a ratio. The logarithmic scale is used to scale down the range of audible sound. The more decibel a sound has, the more forceful it is. Acoustic metamaterials absorb the impacted sound and minimize the decibel on the receiver side.

The amount of sound intensity that decreases when passed through a structure is known as ***transmission loss***. The higher the transmission loss, the quieter the environment is on the receiver side. There is a universal integer rating that explains how well a noise barrier material minimizes sound. It is called ***Sound Transmission Class*** or ***STC***. A Higher STC rating indicates better sound isolation. A standard material will have an STC between the 20s (such as glass) and 30s (the average wall). Effective sound insulation appears at STCs around the 50s. STC testing standards are always updated, so an STC rating from two decades ago will not be the same today. Any material with an average STC rating of 30 or higher is considered better for noise barrier. STC rating is officially approved by the American Society of Testing and Measurement. But this rating has few shortcomings. One is that this rating does not consider frequencies lower than 125Hz. Another is that it is not used in other parts of the world. A material can have a high STC number, but not block specific sounds such as rumbling traffic, reverberating construction, or the droning hubbub of office voices. So, an alternative to STC is required that is acceptable throughout the world and does not have major drawbacks. R_w is the best alternative to STC and used by most of the world. ***R_w*** is the ***Weighted Sound Reduction Index*** which is used to measure the sound insulation abilities of walls, floors, windows, or doors. It is an International Organization for Standardization (ISO) rating and part of the ISO 140 (Acoustic) family. R_w ratings are like STC in that they follow familiar testing methods. But they also differ quite a bit: for example, R_w covers a larger frequency range than STC. R_w rating can not be directly compared to an STC rating. Some professionals prefer R_w because it corresponds to the decibel scale. Any material with R_w rating of 50 means you could expect the noise you want to 'block' to be reduced by 50 decibels if you use that specific material.

Another number is used when constructing or choosing noise barrier material which is known as ***Noise reduction Coefficient*** or ***NRC.*** It is a number between 0.0-1.0. It indicates the average sound absorption performance of a material. If an NRC rating of a material is 0, that means the object reflects sound. If the rating is 1, it indicates that the material absorbs 100% of the impacted sound energy. In nature, it is not possible to find material with NRC rating of 1.

If a metamaterial is designed in such a way that it absorbs most of the impacted sound, then it is possible that the absorbed sound energy is trapped inside the metamaterial. Since energy can not be destroyed, it is possible to change the form of the energy and harvest it using piezoelectric material as electrical potential. ***Piezoelectric materials*** generate an electrical charge when mechanical stress is applied to it. Barium Titanate, Lead titanate, Lead Zirconate titanate(PZT), Polyvinylidene fluoride (PVDF) are some common piezoelectric material. Strategic placement of piezoelectric material inside a noise barrier cell enables it to harvest the trapped or impacted energy. The process of obtaining electrical energy from other external sources such as solar, sound, vibration, wind, kinetic energy, etc. is known as ***energy harvesting.***

In this research, the development of an acoustic metamaterial noise absorber which uses piezoelectric materials to harvest energy simultaneously is studied and analyzed.

1.2. Problem Statement

To date, low-frequency noise remains a problem in the industrial and residential environment. Existing noise control methods can be considered to address the problem. Each method used so far has a unique set of advantages and disadvantages such that one of the methods may be preferred over the rest in a given scenario but less suitable for

another. In some scenarios, the existing noise control practices may not be entirely feasible. Therefore, it is the interest of this research to look for an alternative solution with good low-frequency acoustical performance. The acoustic noise that is filtered by the metamaterial is actually trapped inside the cells. Another interest of this research lies in utilizing the trapped acoustic energy by harvesting it in the form of electrical power.

1.3. Aim and Objectives

This research aims to develop and propose an alternative solution for noise control in various industries by using acoustic metamaterials. Simultaneous power harvesting from the blocked noise is also part of the goal. To progress towards the aim, the objectives of this research are as follows:

- To review the current noise control mechanisms used in noise barriers in the industry.
- To review the different classes of acoustic metamaterials and propose a model that may be viable for effective noise control.
- To identify and address the manufacturing challenges posed by the design with a new class of acoustic metamaterial.
- To develop the metamaterial with air flow capability and aesthetic appeal.
- Utilize the trapped noise in the metamaterial to harvest electrical energy
- To minimize the size and weight of the model and increasing its efficiency

CHAPTER 2

Literature Review

Rapid development in technology and industry has led to an increased amount of noise in the environment. So, controlling unwanted interference is necessary to ensure efficiency of the people these days. Hence researchers have developed various means of noise control using basic control mechanisms. This chapter reviews the noise control mechanisms that have been developed so far for effective noise reduction in various atmospheres. This chapter aims to strategically review the existing noise-blocking techniques used by various researchers. Numerical formulas are kept at a minimum here unless necessary for the explanation.

2.1. Noise Control Mechanism

Since noise control has become an essential measure that needs to be taken in this current situation, this section reviews the various noise control mechanisms used in the noise control industry these days. Noise is measured in decibel scale. **Figure 2. 1** represents the relationship between the noise in decibel and sound pressure in pascals. To understand the level even better, real-life examples on certain sound levels are also added to the chart. Below 85dB, the sound heard is tolerable. When the sound level crosses 85dB, it can cause serious health hazards. In such places with loud sound above 85dB, personal ear protection or some kind of noise barrier needs to be installed. The chart below also explains the levels

which are considered safe and addresses the levels above which personal precautions are advised.

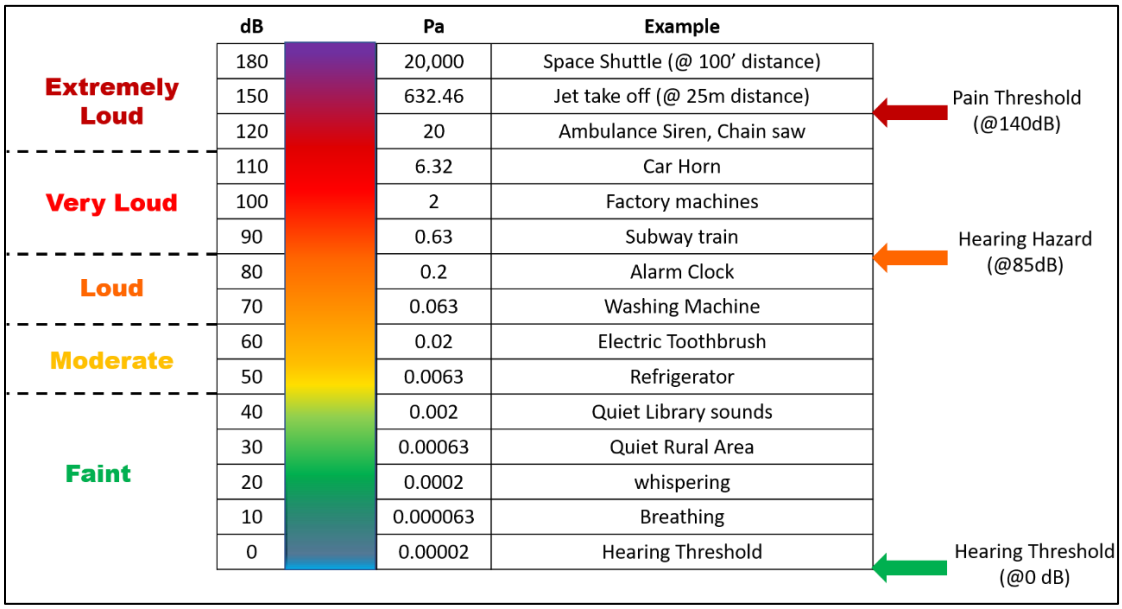

Figure 2. 1: Comparison of Noise level with daily life examples.

Considering the chart values, it is necessary to develop mechanisms to control noise and minimize it when it reaches above safety levels. Based on the sound control mechanism, the approaches can be divided into two sections: active and passive control. Active control uses the electro-acoustical approaches to control noise. There can be two types of electro-electrical approaches; one is to control the sound by creating an anti-phase signal using speakers when it emerges from the source and the other is to suppress the structural vibrations which cause the sound. Passive control uses various methods to modify the environment around the source or receiver. Passive control includes engineered materials that absorb, diffuse, or redirects the impacting sound. Both active and passive control mechanisms can be divided into further sub-sections based on the physics they use for noise filtration. The flow chart shown in **Figure 2. 2** helps to visualize the classification

of the control mechanism easily. This chapter categorically reviews and discusses the mechanisms shown in the chart in further detail.

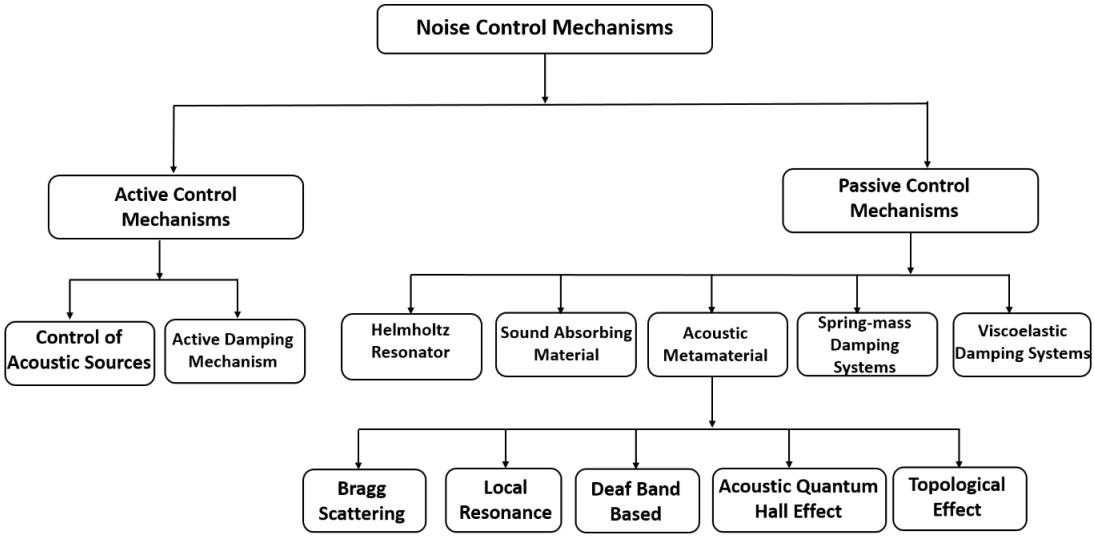

Figure 2. 2: Classification of noise control mechanism

2.1.1. Active Control Mechanisms

Modifying and canceling sound field by electro-acoustical approaches is called active noise control. There are two methods for active control. First by utilizing the actuators as an acoustic source to produce completely out of phase signals to eliminate the disturbances. The second method is to use flexible and Vibro-elastic materials to radiate a sound field interfering with the disturbances and minimize the overall intensity. A passive noise control mechanism is good for high-frequency noise sources, for noises with lower frequency, active noise control mechanisms work better. This section reviews the active noise control mechanisms used for low-frequency noise control.

2.1.1.1. Control of Acoustic Sources

Control of acoustic sources is also known as Active Noise Control (ANC). This concept uses three basic components - speaker, microphone, and controller as reported by Elliott[1]. In this method, the noise created from a primary source is passed through a controller to generate an anti-phase signal. This anti-phase signal is transmitted by a secondary source. Here microphone is the primary source and loudspeaker is the secondary source. This method works best in an enclosed environment. An increased number of primary and secondary sources can improve the noise reduction efficiency of the system. But total noise cancellation is impossible due to various technical reasons such as phase lag and others. Elliot also proposed that a feedforward controller can be installed to overcome the problems but apparently, such systems face challenges during installation.

The ANC has been the interest of the researchers since the late 80s where researchers claimed that this method would transform future cabin noise control[2, 3]. ANC is mostly used to reduce aircraft noise. In the past, ANC has been studied inside an actual aircraft cabin by numerous researchers[4-6]. Among all these, a maximum of 14dB noise reduction was achieved. It was also reported that the efficiency of the ANC mechanism depends highly on the presence and distribution of secondary sources. Additionally, Elliott et al. found that at localized field points, their model could achieve up to 35dB of noise reduction. Based on these basic experimental studies, Martin et al. numerically validated the results but added that there should be no more than 30 secondary sources in this scenario[7]. Few potential problems related to this method are that it increases the weight of the structure and these work best if the source is nearby the sound source. To solve this problem, Kestell et al. proposed to adjust the transmitted signal[8].

Though ANC is common in aircraft, it has been recently considered for trains and automobiles [9-12]. Lately, the development of ANC systems was summarized in a review article by Samarasinghe et al.[13]. This article provides various reasons why ANC has not yet been widely adopted by people. The reasons include the higher cost of implementation, the complexity of the hardware requirement, poor stability, etc. This is still a developing field and researchers are working to overcome the drawbacks shortly.

2.1.1.2. Active Damping Mechanism

From the discussion in the previous section, it is evident that the ANS systems have various drawbacks. To overcome the faults, a new system is proposed which not only controls the cabin noise but also works towards reducing the structural vibrational reduction. The main difference of this mechanism is that it controls the noise indirectly where ANC controls noise directly. Sensing accelerometers are used to measure the vibration level and send it to the controller. Another set of accelerometers is placed near the control region to provide feedback and minimize error. The entire process runs in a loop and reduced the sound developed from specific locations. This active damping mechanism is also known as Active Structural Acoustic Control (ASAC).

Like the acoustic source control mechanisms, ASAC has also been studied rigorously in the late 80s. the initial fundamental work on such systems was published by Fuller and Jones[14] where they achieved around 20dB of cabin noise reduction. This study was extended by a few other researchers considering an actual aircraft cabin[15, 16]. This extended research had some loophole where they did not consider the effect of the actuator position. Later this issue was addressed by a comprehensive study done on a rectangular enclosed space. This study suggested that the actuator location need not be limited to a

specific location[17-19]. This study has made the ASAC systems capable of cabin noise control in aircraft. Constant study on this system has improved the mechanism by multiple folds. Since the ANC had a problem being bulky because of the presence of shaker attachment, Fuller et al. proposed to replace the shaker with piezoelectric patch[20] and after that other researchers also validated the concept[16, 21]. The use of piezoelectric patches revolutionized this system. These patches were lightweight, could undergo large strain deformation, had low power requirements, and affordable. The only drawback with these was the brittleness of the patches. A huge amount of study has been done on ASAC since then[22-25] to better understand and improve the mechanism.

Though active noise control can be done employing ANC or ASAC, very few studies have been done where both the approaches have been deployed. Recently, Sas et al. used ANC and ASAC both in a cabin of a station wagon[26]. They concluded that ASAC provided a global stable cabin noise control compared to ANC. They suggested that both methods are suitable for local noise control but ASAC is preferred for global noise control. Since ASAC controls noise and minimizes structural vibration, it is in every way better than ANC. Still, research is being conducted to improve the methods by addressing the drawbacks.

Table 2. 1: Summary of Active noise control

	Author	**Suggestions/strategies/method**
Control of acoustic sources	Elliott[1]	Feedforward or feedback control using reference signal, error signal and secondary microscope.
	J. Tichy[2]	Necessity of developing optimization techniques in secondary sources and controlling microphone locations
	Silcox et al[3]	Sound attenuation of ~15dB observed inside thin, elastic, cylindrical shell with fixed discrete monopole sources.

	Elliott et al[5]	~13dB sound reduction measured during in-flight experiments using 16 loudspeakers and 32 microphones.
	Martin et al[7]	Testing various aircraft models using number of secondary sources to calculate sound attenuation.
	Kestell et al[8]	Analytical model used to predict and compare the virtual sensor's performance and experimental validation.
	Oh et al[10]	~6dBA sound pressure reduction inside an automobile using active feedforward control system model.
	Botto et al[11]	Fuzzy and neural modelling paradigms integrated in active noise reduction scheme to minimize noise in railway coach
	Liu et al[12]	~4dBA noise reduction in electric locomotive cab using proposed ANC system based on whole cab space.
Active damping mechanism	Fuller and Jones[14]	Structural-acoustic coupling between the shell and the field shows global attenuation of interior noise at resonant and forced vibration frequencies.
	Simpson et al[15]	Effectiveness of active vibration control methods to minimize aircraft cabin noise
	Mathur and Tran [16]	Experimental investigation results of sound minimization inside aircraft cabin using active structural acoustic control
	Pan et al [17]	Acoustic characteristics and sound absorption properties of different boundary conditions in well damped enclosed rectangular space is measured and experimentally verified.
	Pan and Hansen [18]	Optimum location selection of a point force actuator to control sound through a panel with cavity.
	Fuller et al [20]	10-15dB of interior noise control using piezoceramic actuators.
	Sun et al [21]	Piezoelectric actuators used to reduce both structural vibration and interior noise.
	Grewal et al [23]	~28dB noise reduction and ~16dB vibration reduction for propeller induced noise and vibration achieved using ASAC.
	Palumbo et al [24]	A control algorithm for ASAC in airplane to control blade passage frequency using 21 actuators and 32 microphones.
	Niezrecki and Cudney [25]	PZT actuators used to control fairing vibration and internal acoustic environment.
	Sas & Dehandschutter [26]	Adaptive feedforward control algorithm to reduce road noise inside car cabin under different road conditions.

2.1.2. Passive Control Mechanism

Passive noise control refers to those methods that aim to suppress the sound by modifying the environment close to the source. Since no input power is required in such methods, Passive noise control is often cheaper than active control, however, the performance is limited to mid and high frequencies. active control works well for low frequencies hence, the combination of two methods may be utilized for broadband noise reduction.

2.1.2.1. Helmholtz Resonator

Helmholtz resonators are referred to as a fluid-filled (usually air) hollow container with a narrow neck. The Helmholtz resonator effect is caused by the motion of the air at its neck. The inside fluid acts a spring which helps the neck air to oscillate. This can be denoted as a spring-mass system. This phenomenon of air resonance in a cavity with a narrow neck is known as Helmholtz resonance. Helmholtz resonator and its effects on acoustic media have been studied for a very long time but around three decades ago Fahy and Schofield[27] presented some disagreement with the existing designs. They experimentally proved the existence of two modes on either side of the resonator's fundamental frequency. This study is considered as a foundation for Helmholtz resonator design.

Helmholtz resonance is being utilized in passive noise control mechanisms by modifying their design parameters which allow the structure to dampen sound. Numerous research endeavors have been undertaken to determine the most effective way to use adaptive Helmholtz resonators. Though Fahy and Schofield's study is considered the foundation, later Cummings showed that their study lacks practicality since they used only a single resonator. Cummings proved analytically that the use of an array of resonators are

required in cases where multiple frequencies of sound are involved[28]. This study of Cummings was later investigated further with advanced computational power tools[29]. From these studies, it could be concluded that change in incident frequency can change the effectiveness of the resonator. So, a unique resonator design is required to address the noises of various origins. Koopman and Neise[30] studied adjustable resonators to dampen the centrifugal fan noise. Their experiment demonstrated a drop of about 29dB. But they did not suggest ant conclusive method.

Helmholtz resonators have been used widely in the automobile industry to reduce cabin noise. Since they might decrease the aesthetic appeal of the automobile, Franco proposed that the boot compartment can be used for such installations[31]. He suggested creating a slit in between the boot and the passenger cabin. Few other researchers have also studied the installation of Helmholtz resonator to minimize cabin noise in automobiles [32-36]. Apart from automobile cabin, Helmholtz resonator has also been used to minimize aircraft cabin noise. Initially, Laudien and Niesl[37] introduced the concept of adding perforation behind the seat of a helicopter and creating Helmholtz resonators without increasing the weight of the aircraft. Similarly, Helmholtz resonators have also been used as a noise barrier material to minimize industrial noise. Functionally graded Helmholtz resonators are used by Zhao et al. [38] in a spiral bio-inspired pattern for rainbow trapping (**Figure 2. 3**). They utilized the passive noise controlling feature of the Helmholtz resonators and arranged them in a space-saving design. Their design is suitable for places where weight and space are a constraint. They numerically and experimentally proved that a spiral array of Helmholtz resonators can filter broadband acoustic waves.

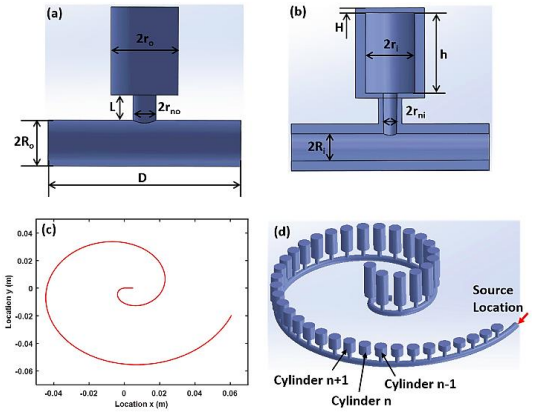

Figure 2. 3: Schematic illustration of the cochlear-inspired structure. (**a**) Front view of Helmholtz resonator unit cell. (**b**) Cross-sectional view of the Helmholtz resonator unit cell showing the hollow interior of the cylinder and spiral tube. (**c**) Archimedean spiral and (**d**) isometric view of the entire structure [38].

On the other hand, Helmholtz resonance is utilized by Isozaki et al. on a planar notch filter with sub-wavelength thickness[39]. Their designs include multiple Helmholtz resonators connected to a hole created in a plate (**Figure 2.4**). They arranged the HRs around the hole in a hexagonal pattern. Their numerical and experimental results agreed to each other and helped them to conclude that increasing the number of uniformly arranged Helmholtz resonators decrease the transmission at the notch frequency.

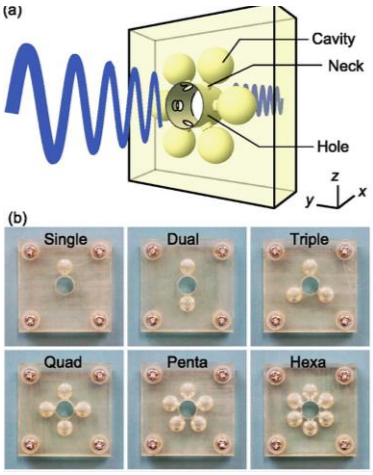

Figure 2.4: (a) Schematic illustration of the proposed planar acoustic filter. (b) Photographs of the fabricated filters [39].

Another interesting application of Helmholtz resonator has been reported by Wang et al. [40] where they developed a noise barrier for high-speed railways. They used a hexagonal Helmholtz resonator as the noise filtering structure. This article studies and compares two models of the same design but one with and another without a noise collection input module. They have also incorporated PVDF film inside the cavity to harvest power from the acoustic pressure. Their results indicate that model with noise collection input module works best in all the circumstances as the input module helps magnify the sound pressure. This design looks promising and can be utilized as a low frequency noise barrier material (**Figure 2. 5**).

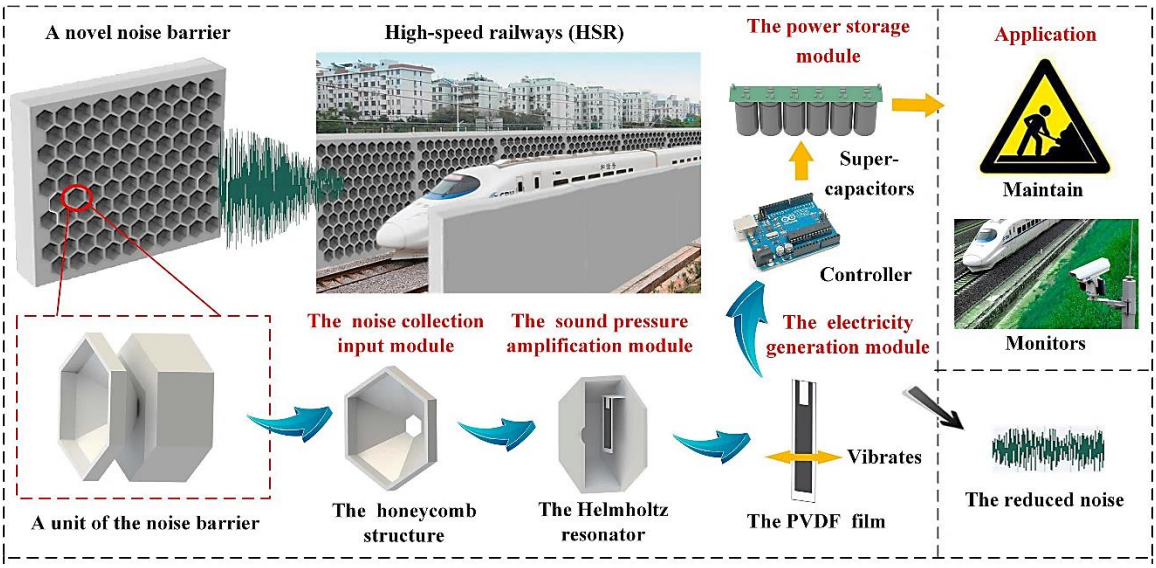

Figure 2. 5: Architecture of the acoustic energy harvesting noise barrier[40].

From the study done by Wang et al and Isozaki et al. it is evident that the change in the dimension of the resonator cavity, neck parameters can change the performance of HR. As changing the neck parameters is easier compared to the change of other resonator dimensions, various researchers have manipulated the neck material and parameters of HR to optimize the design's performance[41-44].

Some researchers have gone one step further to incorporate an HR inside a bigger HR or adding double-walled resonators. Double-walled resonators are tuned to filter as much noise as possible and increase transmission loss[45].

2.1.2.2. Sound Absorbing Material

Since sound can cause double trouble if the barrier material reflects the incident sound creating more problems. From such needs, sound-absorbing materials have been developed for noise barriers which allow the barricade to absorb most of the incident sound and keeping the environment clean. Earlier, membrane type sound-absorbing materials were most popular for indoor and cabin noise mitigation [46-48]. Cai et al reported ultrathin coiling based metamaterial panel which absorbs low-frequency sound with minimal thickness[49]. **Figure 2. 6**(a) represents the design developed by Cai et al. On the other hand, Cavalieri et al.[50] reported a 3D multi resonant design which has an average transmission loss of 16.8dB (**Figure 2. 6**(b)). Parallelly, for low-frequency noise mitigation, double negative meta structures were reported by Kumar et al. [51] This study reported a 1D acoustic metastructure capable of exhibiting double negative parameters. This material can absorb an average transmission loss of 45dB for frequencies below 500Hz. The flexibility of the design allows it to be used for lowering aircraft cabin noise. The design is represented in **Figure 2. 6**(c). Another ultrathin metastructure is proposed by Li and Assouar where a thin perforated plate with holes is placed on top of a rigid squared air cavity with a coiled chamber[52]. This structure can achieve perfect sound absorption at a frequency of 125Hz (**Figure 2. 6**(e)). A very classic design that has been used for ages is the Schroeder Diffuse. Zhu et al. used the SD mechanism and redesigned it in the form

of an acoustic metasurface with ultra-thin thickness[53]. This design has a far-reaching implication in noise control (**Figure 2. 6**(d)).

Various other researchers have also developed unique sound-absorbing metamaterials which help reduce sound in the most noise environments[54-56]. These materials have unique feature and material properties which allows them to work as noise absorbers. This is still a developing field and there is a huge prospect in this section in the upcoming times.

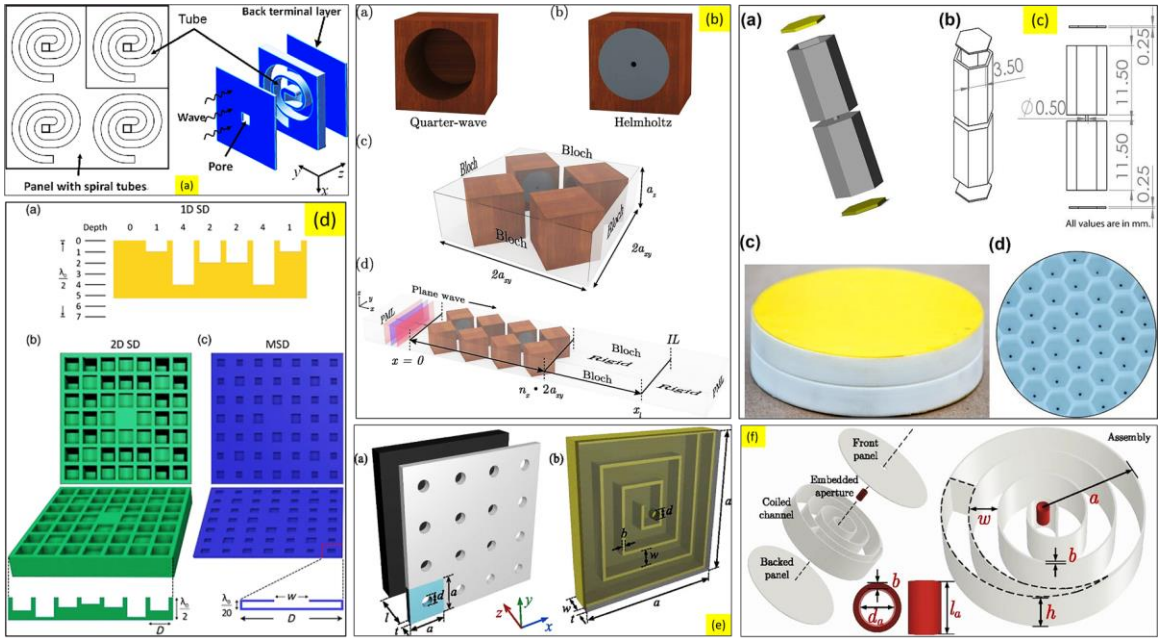

Figure 2. 6: Sound-absorbing materials developed by various researchers. (a)Ultrathin coiling based metamaterial panel[49] (b) 3D multiresonant sound absorbing metamaterial[50] (c) 1D metastructure with double negative parameters [51] (d) Ultrathin acoustic metasurface-based Schroeder diffuser[53] (e) ultrathin metastructure with thin perforated plate with holes is placed on top of a rigid squared air cavity with a coiled chamber[52] (f) Acoustic perfect absorbers via spiral metasurface with embedded apertures [55].

2.1.2.3. Acoustic Metamaterial

In the past two decades, huge progress has been made in the acoustic metamaterial field. These materials have demonstrated tremendous potential for wide frequency noise absorption. Owing to the promising advancement, the designs developed by the researchers so far can be used in practical settings for effective noise reduction in various environments. Acoustic metamaterials use a few basic physics to attenuate sound waves and filter noise. Five of the most widely used physics are discussed in this section.

2.1.2.3.1. Bragg Scattering

Let us consider two identical scatterers at a distance of Δx. There is a time lag or phase difference between the incident and the radiated wave. The scattered waves interfere destructively. The distance between the scatterers leads to a strong destructive effect on wave propagation. This phenomenon is called the Bragg scattering. It happens at the heart of the phononic crystal. In a crystal, at the frequencies where the Bragg condition meets, a frequency window is created through which no waves can propagate. Such a window is called a bandgap. Acoustic metamaterial uses Bragg scattering to create bandgaps so that the cells can be used as a noise barrier material. **Figure 2.7**(a) represents a tunable acoustic metamaterial with a square array of circular holes and resonators which is capable of filtering low-frequency noise. The numerical study from this model indicates that the locally resonant Bragg scattering band gap can be controlled by controlling the amount of deformation[57]. On the other hand, Chen et al.[58] reported a triply periodic co-continuous acoustic metamaterial that can filter wave using the Bragg scattering phenomenon (**Figure 2.7**(b)). But these metamaterials operate on a very high-frequency range. So, it is not suitable for application in regular noise barrier walls. Similarly, Casadei

et al.[59] reported another tunable waveguide configuration where Bragg scattering bandgaps are combined with piezoelectric resonators to confine the propagation of elastic waves in a phononic crystal plate (**Figure 2.7**(c)).

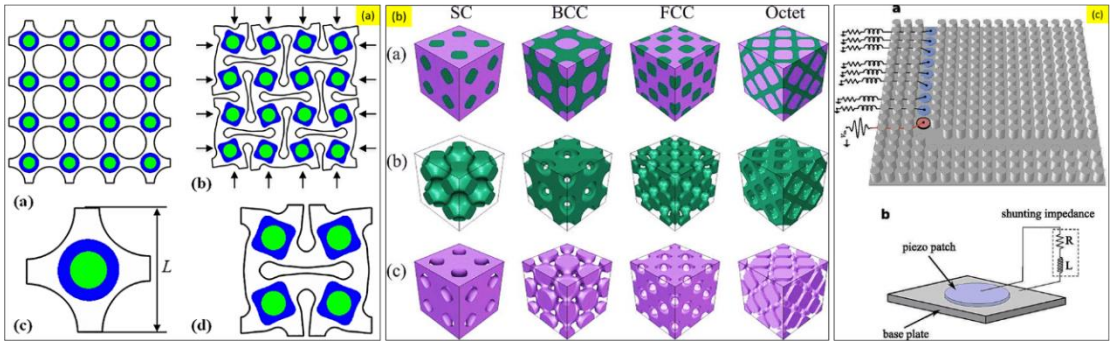

Figure 2.7: Bragg scattering phenomena observed in various acoustic metamaterial structures (a) Tunable acoustic metamaterial with a square array of circular holes and resonators [57](b) triply periodic co-continuous acoustic metamaterial capable of filtering wave using the Bragg scattering phenomenon [58] (c) Piezoelectric resonator arrays for tunable acoustic waveguides and metamaterials [59].

Apart from these cases, various researchers have worked on developing unique acoustic metamaterial structures that used the physics of Bragg scattering[60-62]. Recently, Wen et al. proposed an acoustic metamaterial beam with periodically variable cross-sections which combines the Bragg scattering and locally resonant bandgap mechanisms. These structures reduce the vibration of a structure in a wide frequency range. Based on the numerical and experimental validation of the model, they have concluded that band gaps become stronger and wider with the increase in the sub-cell sizes[63].

2.1.2.3.2. Local Resonance

From the research conducted so far, it is evident that periodic structures have an influence on the propagation of waves. For instance, if we consider two oscillators, the coupling between them is strongest if they are degenerate. The coupling is expected to split the

degenerate system of the wave and the local resonator onto the dispersion of waves. This effect is strongest at the point where two frequencies cross. Here also, similar to the Bragg scattering effect, a window is present through which no wave propagation is possible. The frequency is not directed by the spacing of the periodic array, instead, the local oscillator's frequency dominates it. The propagation of waves can be modified in the vicinity of a specific frequency by coupling the wave to a local resonance with a similar frequency. This local resonance phenomenon is widely used for designing noise filtering acoustic metamaterials. Manipulation of the design parameters can help achieve desired band gaps in a specific frequency range.

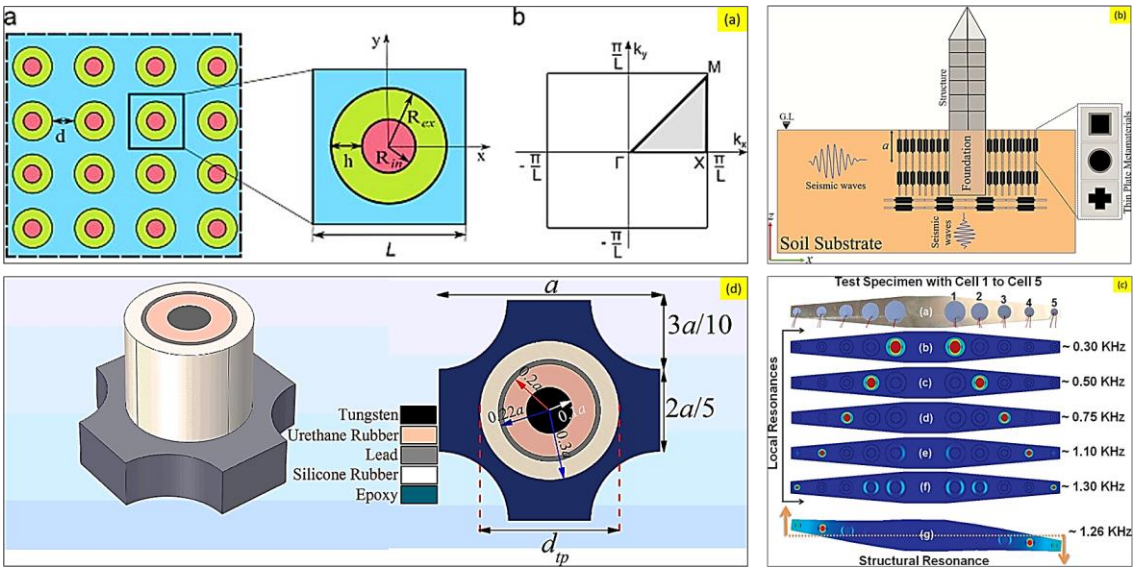

Figure 2.8: Local resonance phenomena observed in various structures. (a) optimal design of locally resonant metamaterial [64] (b)elastic wave propagation in thin wave metamaterial[65] (c)multiresonant pillared and trampoline metamaterial [66](d)energy harvesting using sub wavelength scale acousto-elastic metamaterial. [67]

Figure 2.8 shows some of the structures where researchers used local resonance phenomena to filter sound. Krushyanska et al. exhibited an optimal design of locally resonant acoustic metamaterial[64]. They have presented a detailed study on the influence

of geometric and material parameters, filling fractions, and inclusion shape on the width of the lowest bandgap. They have advised to used tungsten core material as an alternative to traditionally used lead or gold metals. This model creates band gaps in a low-frequency range (**Figure 2.8(a)**). Muhammad and Lim[65] proposed an elastic thin plate where low-frequency band gaps can be observed. This structure uses local resonance phenomena. Researchers suggest that this kind of plate metamaterial can be used for subwavelength manipulation including seismic shielding of civil infrastructures (**Figure 2.8**(b)). Lim also reported another dissipative multiresonant pillared acoustic resonator which can amplify the local resonance bandgaps[66]. The unit cell of the design is demonstrated in **Figure 2.8**(d). These unit cells can be arranged periodically to generate wide band gaps. This model works in a higher frequency range. Ahmed et al. [67] reported a multi-cell metamaterial model with linearly varying core mass which utilizes the physics of local resonance phenomena (**Figure 2.8** (c)).

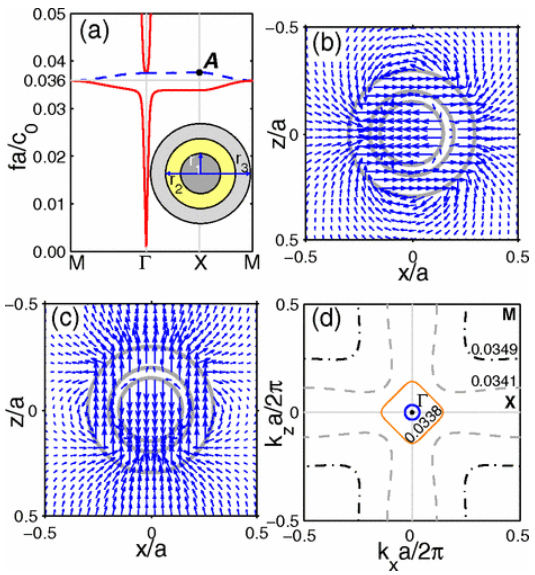

Figure 2.9: Far field image magnification using acoustic metamaterial and the observation of deaf band [68]

2.1.2.3.3. Deaf Band Based

Ao et al. reported a design of an acoustic metamaterial that can form a far-field image beyond the diffraction limit[68]. They studied a 2D array of coaxially layered rods in the water. They observed transverse modes corresponding to zero effective density (Error! Reference source not found.**a**). These are labeled as deaf bands since they do not couple with normal incident longitudinal waves.

Very recently, Indaleeb et al. [69] reported an acoustic metamaterial where a Dirac cone-like point is introduced. They presented a deaf band based predictive model which has the potential to achieve engineered Dirac cone. Their model includes PVC cylinder PnCs immersed in air. They experimentally validated the model to confirm the numerically generated orthogonal wave transport phenomena (**Figure 2.10**).

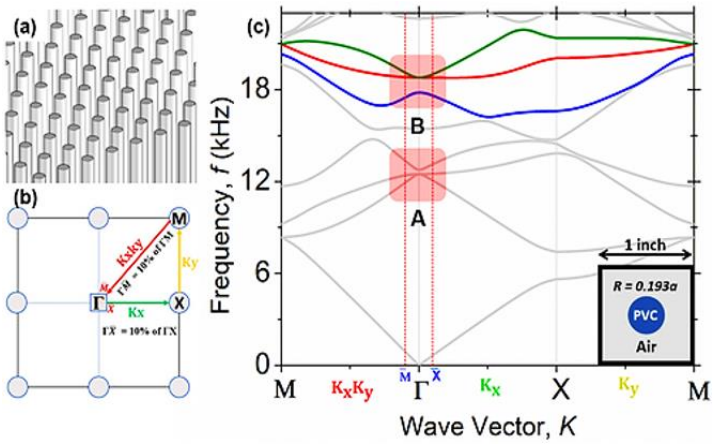

Figure 2.10: (a) PVC cylinder PnCs immersed in air, (b) BZ depicting reduced wave vector direction, and (c) full dispersion band structure for PVC in air [69]

Earlier Indaleeb et al. [70] also reported Dirac cone-like dispersion at the center of the Brillouin zone created due to accidental degeneracy. They observed that nondispersive deaf band frequency remains unaltered from any arbitrary periodic structure made of PnCs. Their claims are validated numerically and experimentally, and they reported that

orthogonal wave transport, negative refraction, and wave vortex exist at the deaf band based engineered Dirac cone (

Figure 2. 11).

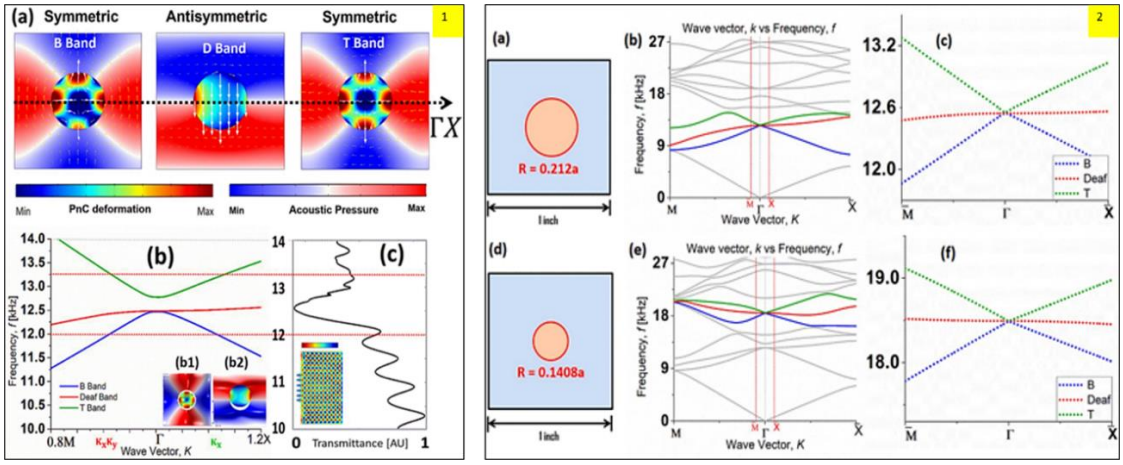

Figure 2. 11: [(1) B, deaf, and T band mode shapes of the PVC cylinder surrounded by the air pressure mode shapes with arrows and observation of deaf band; (2) (a) Unit cell and Dispersion relation for region A with magnified view[70]

2.1.2.3.4. Acoustic Quantum Hall Effect

The acoustic quantum hall effect is a new phenomenon observed in acoustic metamaterials recently. Under a strong magnetic field, many intrigue phenomena can be observed. Recently, the introduction of graphene has opened the door to quantum transport control by mechanical means. Wen et al [71] reported the first experimental realization of a giant uniform pseudo magnetic field in acoustics by introducing a simple uniaxial deformation to acoustic graphene. They proposed a strategy to create a uniform pseudo magnetic field (PMF) for airborne sound by arranging a 2D sonic Crystal array in a triangular lattice and validated the model experimentally. They attained uniform PMF by modifying only one geometric parameter in one direction. They claim that their model can be extended to other artificial structures such as a patterned photonic crystal slab on a silicon chip(**Figure 2.12**).

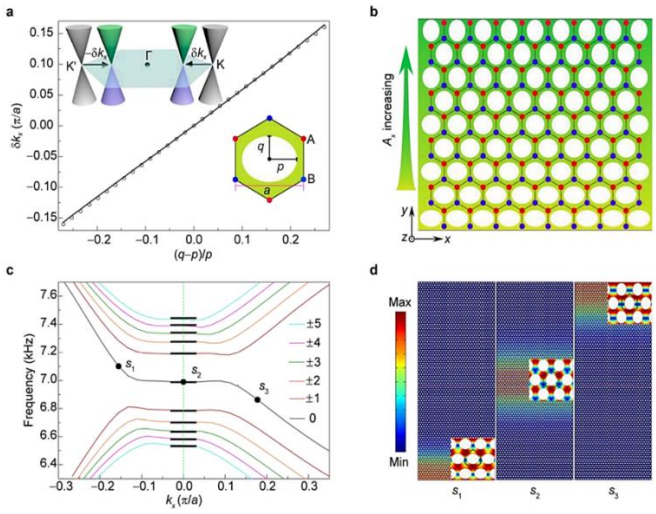

Figure 2.12: Synthesized acoustic magnetic field and relativistic Landau quantization for observing acoustic quantum Hall effect. [71].

Zhou et al.[72] developed a membrane-type metamaterial and observed quantum hall effect in it. To theoretically analyze the metamaterial, they have employed a density heterogeneous membrane model. However, the working frequency range of the topological system is very narrow. But the frequency range can be widened by applying an electrical voltage (**Figure 2. 13**). The experimental results have validated the concept of the metamaterial with tunable topological behavior. It is lightweight and can couple with acoustic waves.

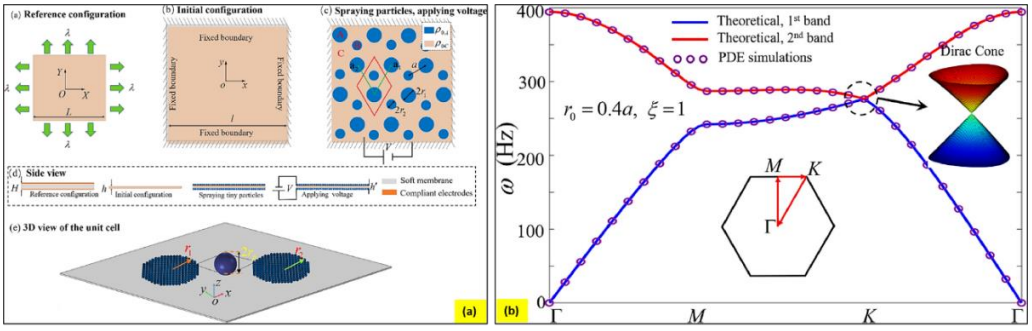

Figure 2. 13: (a) Fabrication steps of soft MAM. and 3D view of the unit cell. (b) The band structure and the Dirc cone in soft MAM.[72]

The capacity of guiding currents towards specific directions according to the spin of the traveling electrons has been transposed to the classical domain in electromagnetics and acoustics, unveiling the pseudo-spin locking of guided waves. However, these macroscopic analogs are photonic/phononic crystals which are intrinsically wavelength-scaled. Yves et al.[73], reported a genuine acoustic analog of the valley-Hall effect in the audible regime using a lattice of soda cans. They experimentally demonstrated the unidirectional excitation of sound guided at a scale much smaller than the wavelength of operation. These results not only open the tantalizing valley-topological phenomena to the audible regime but also allow us to envision compact applications for acoustic manipulation.

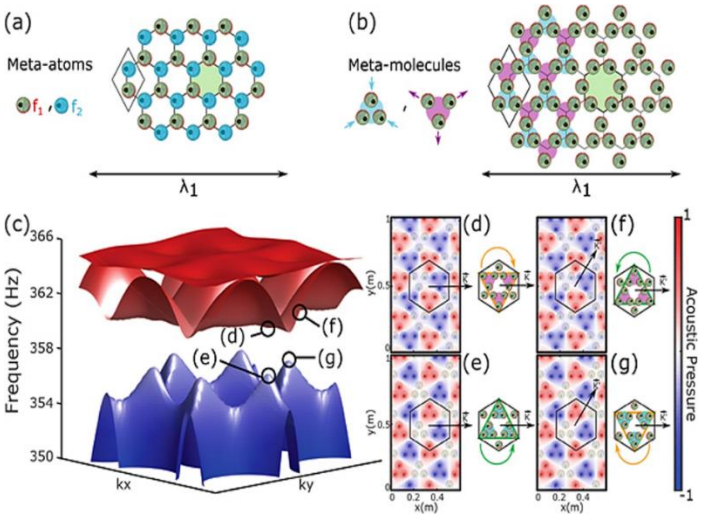

Figure 2.14: Visualization of Bidisperse honeycomb lattice and Breathing Kagome lattice of soda cans. Dispersion relation and Acoustic field map of the crystalline mode of the breathing Kagome lattice can also be seen[73]

This is a recently developed phenomenon in the acoustic field. Researchers are working constantly to understand its effects and ways to manipulate it for more user-

friendly operations. Studies done so far show promising future of the crystalline metamaterials for discovering more solid-state physics phenomena.

2.1.2.3.5. Topological Effect

Topological insulators have drawn significant attention due to their unique one-way wave propagation characteristics which are not affected by defects or disorders in the structures[74-76]. In topological insulators, the outer surface is conductive while there is a bandgap like phenomenon inside the cell which makes it an insulator to the electron flow. Topological metamaterials are developed considering the same physics and they demonstrate a new vision for domination of wave propagation aside Bragg scattering and local resonance.

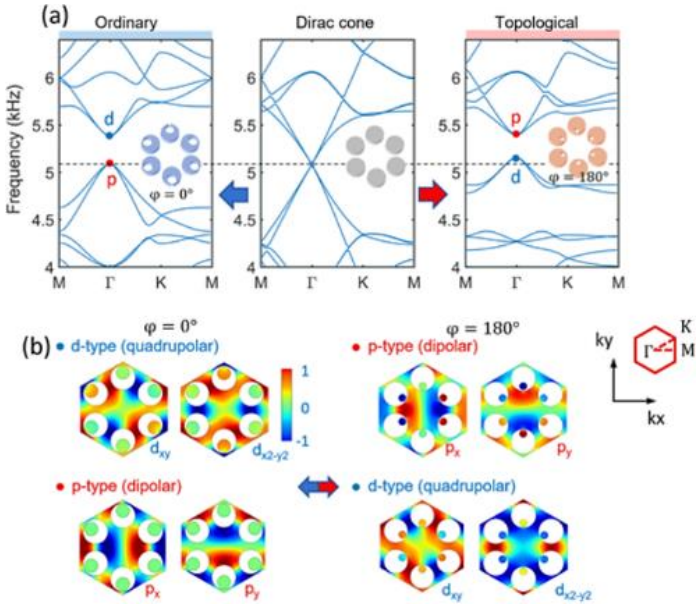

Figure 2.15:(a) Band structures of the honeycomb phononic crystals for the ordinary state (left), double Dirac cone (middle), and topological state (right). (b) Pressure fields for the ordinary (left panel) and topological (right panel) states.[77]

Understanding of topological transition by the interaction between these mechanisms is strongly desired to extend the design degrees of freedom for intriguing wave

phenomena. Lee and Iizuka [77] demonstrate a phononic metamaterial consisting of C-shaped elements and investigated interaction between Bragg scattering and local resonance. They have reported that adding resonance scattering a topological band gap is opened from a Bragg scattering based Dirac cone, and its bandgap is controlled by the resonance frequency of the cavities relative to the Dirac cone frequency. They have also proved that topological bandgap opening induced by the Bragg scattering can be reversed into an ordinary state or vice versa by thoughtful inclusion of the local resonance **(Figure 2.15).**

Higher-order topological insulators are a family of recently predicted topological phases of matter that obey an extended topological bulk–boundary correspondence principle. Xue et al. [78] have presented an acoustic metamaterial based second-order topological insulator. They report that this model is shape-dependent and it allows corner states to act as topologically protected but reconfigurable local resonances.

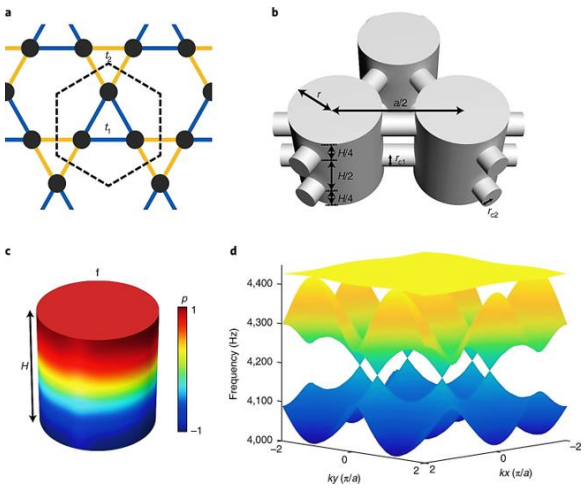

Figure 2.16: (a) Tight-binding model for the kagome lattice. (**b)**, Unit cell of the acoustic kagome lattice, with a cylindrical resonator at each site joined by thin waveguides; (**d)**, Numerically computed bulk bands for the acoustic kagome lattice shown in **b**[78].

Recently a new class of topological states has been reported which is localized in more than one dimension of a D-dimensional system[79]. Such systems are referred to as higher-order topological (HOT) states. These offer an even more versatile platform to confine and control classical radiation and mechanical motion. The assembled 3D topological metamaterial represents the acoustic analog of a pyrochlore lattice made of interconnected molecules and is shown to exhibit topological bulk polarization, leading to the emergence of boundary states (**Figure 2.17**).

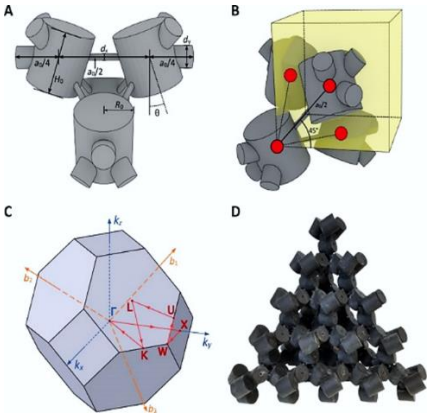

Figure 2.17: Schematic and realistic design of the Wigner-Seitz unit cell of the expanded pyrochlore lattice and photograph of the 3D topological metamaterial assembled from 3D printed metamolecules, with boundary cells attached [79].

2.1.2.4. Spring Mass Damping System

The spring-mass-damper model is the most basic method of suppressing vibration. These models are used widely to minimize structural vibration and thus minimize noise. Now is the age of metamaterials. So the traditional spring mass damper system has also entered the metamaterials club for enhanced structural vibration suppression. Peng et al.[80] modeled a metamaterial plate with mass-spring-damper subsystems (**Figure 2. 18a**). This design uses the local resonance phenomena of the subsystem to absorb energy and thus creates stopbands. A bandgap can be observed right above the natural frequency of the

system. This model can be used to suppress low-frequency vibration and expand stopband. He, Xiao and Li[81] presented a laminate acoustic metamaterial that has a carbon fiber-reinforced polymer and a periodic array of spring-mass damper sub-system (**Figure 2. 18b**). This model acts as a vibration absorber and the dispersion analysis shows that this model generates a wide stopband. This design is used to design a vehicle door where the vibration of the door was suppressed significantly. Various other researchers have also reported unique designs for such noise control mechanisms[82, 83].

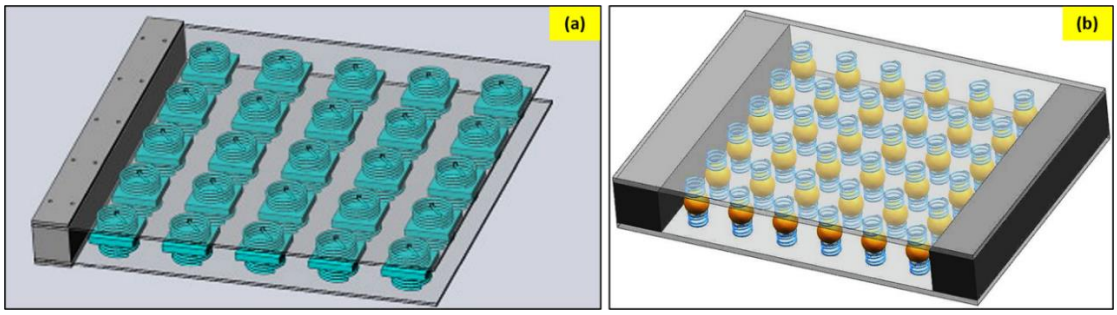

Figure 2. 18: Spring Mass damping systems to suppress noise. (a)acoustic metamaterial plate with elastic wave absorption [80] (b)structural vibration suppression in laminate acoustic metamaterial [81]

2.1.2.5. Vibration Absorbing Structure

Vibration is one of the major sources of industrial noise. Reduction in the vibration of a structure or isolating the vibrating surface will lead to a huge reduction in environmental noise. Ideally, spring is used in most cases to suppress vibration. Modern complex problems with vibration sources have led researchers to develop lattice structures to absorb a wide range of vibrations. Such vibration absorbing structures fall under the passive noise controlling mechanism. Yu et al.[84] have reported a viscoelastic damping system that damps vibration for mid-frequency noise control. Their model can significantly reduce the total acoustic energy of the system and ensure a uniform modal energy distribution (**Figure**

2. 19a). Feng et al. [85] reported a design to reduce the vibration of an existing glass window using viscoelastic material. Their method enables retrofitting of existing glass windows for vibration absorption (**Figure 2. 19b**). These windows work on a very low-frequency range (0-50Hz). Their model is easy to implement, almost maintenance-free, and has aesthetic appeal.

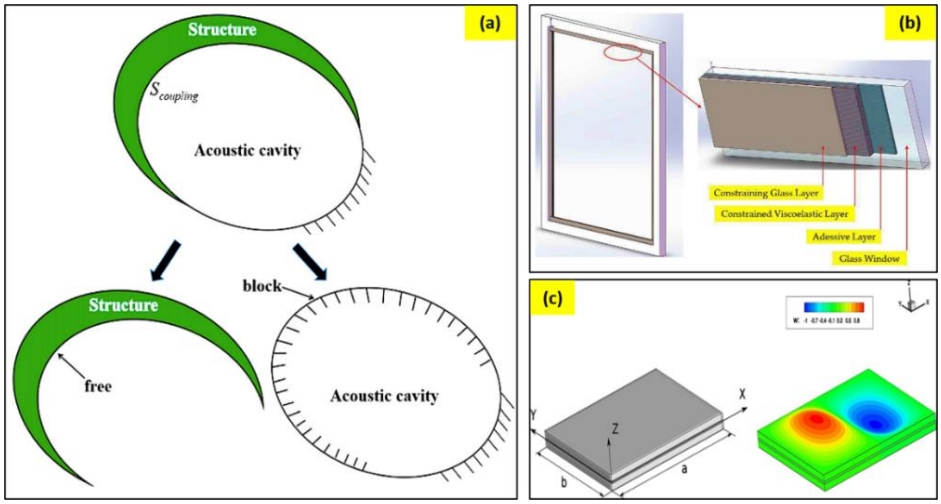

Figure 2. 19: Vibration absorbing structure (a) viscoelastic damping for mid frequency noise control [84] (b)vibration reduction of an existing glass window [85](c) Noise reduction passive control system based on viscoelastic material based retrofit. [86]

Sound transmission and insulation of aeronautical panels represent one of the major problems of aircraft comfort. Valvano et al. [86] proposed a plate finite element with an advanced higher-order kinematic field for the analysis of noise reduction passive control system in laminated structures. The acoustic insulation of the panels is evaluated by computing its sound transmission factor using the Rayleigh integral method. They have conducted various numerical investigations to validate and demonstrate the accuracy and efficiency of the acoustic optimization procedure for the design of viscoelastic plates (**Figure 2. 19c**). *Table 2. 2* summarizes the passive controm mechanisms studied so far.

Table 2. 2: Summary of Passive control mechanisms with noise reduction capability

Helmholtz Resonator		
Author	Model Description	Noise Reduction
Fahy and Schofield [27]	a cylindrical resonator with a cavity and neck placed inside a room is exposed to a various range of frequencies	11.6 dB
Neise and Koopmann [30]	replaced the scroll cutoff with a quarter-wavelength resonator. It was tuned by changing the length via a movable plug	29 dB
Franco [31]	reduction of low frequency cabin noise by tuning an acoustical resonator using the luggage compartment	1.4 dB
Laudien [37]	reduction of helicopter cabin noise using honeycomb bulkhead and various measures to optimize transmission loss in window, sealing and frame.	17 dBA
Zhao [38]	rainbow trapping of acoustic waves using a hollow spiral tube and 40 Helmholtz resonators attached to it.	
Isozaki [39]	planar acoustic notch filter with multiple spherical Helmholtz resonators placed in vertices of a polygon.	
Selamet and Lee [42]	studied a concentric Helmholtz resonator with extended neck.	~40dB
Yang et al[43]	effects of different neck material on the sound absorption capability of Helmholtz resonator.	~0.75 (sound absorption coefficient)
Tadeu and Mateus [45]	experimentally validated the sound insulation capability of glazed openings.	30dB (R_w)
Sound Absorbing Material		
Yang et al [46]	experimentally verified the theoretical study of the membrane type acoustic metamaterial in 100-1000Hz range.	0.01% (Transmission)
Yang et al [47]	metamaterial with two coupled membranes which has double negativity	13.9 dB (STL)
Ang et al [48]	design and verification of meta panel made of plexiglass hollow tubes for low frequency noise control.	

Cai et al [49]		coiling up quarter wavelength sound absorbing tubes in coplanar matrix and form a sound absorbing panel.	100% (absorption)
Cavalieri et al [50]		periodically coupled quarter wavelength and Helmholtz resonators to produce large insertion loss.	16.8dB (Insertion Loss)
Kumar et al [51]		dual hexagonal resonators connected by a common neck for low frequency noise absorption in aircraft.	TL: 58 dB Absorption: 48%
Li and Assouar [52]		a coiled coplanar air chamber and perforated plate used to construct a low frequency perfect sound absorbing metasurface.	100% (absorption)
Zhu et al [53]		used the Schroeder diffuser design to develop a sound diffusing acoustic metasurface.	
Zhang et al [54]		labyrinth acoustic metamaterial capable of perfectly absorbing low frequency air borne sound.	100 % (Absorption)
Huang et al [55]		perfect sound absorber using coiled channel and embedded aperture.	100 % (Absorption)
Acoustic Metamaterial			
Bragg Scattering	Prasetiyo et al [56]	coiled up air chamber to absorb low frequency sub wavelength sound.	80% (Absorption)
	Casadei et al [59]	phononic crystal plate with cylindrical stubs & L shaped wave-guide with PZT discs.	
Deaf Band Based	Ao and Chan [68]	locally resonant acoustic meta-material capable of creating low frequency band gap which can be tuned for desired range, creates deaf bands.	
	Indaleeb et al [69]	targeted dirac cone at a higher frequency validating orthogonal energy transport in spiral pattern.	Dirac cone @ 12.5kHz and 18.512kHz
	Indaleeb et al [70]	deaf band based phononic crystals are modeled andand multiple occurrence of dirac like points are are demonstrated	Dirac cone @ ~12.5kHz and ~18.5kHz
Acoustic Quantum Hall Effect	Wen et al [71]	uniform pseudomagnetic field in acoustics by adding de-formation in acoustic graphene.	
	Zhou et al [72]	membrane type metamaterial developed with tunable topological properties to monitor the quantum valley hall effect	Dirac cone at ~275Hz
	Yves et al [73]	guiding sound waves at a lower scale than the operational wavelength and experimentally observe the quantum valley Hall effect.	Dirac cone and band gap above 355 Hz
Topological	Fu and Kane [74]	the linear connection between superconductors judged by topological insulator to form a nonchiral 1D wire.	

	Zhang et al [75]	calculated pre-diction of topo-logical insulators with single dirac cone on the surface.	
	Chen et al [76]	investigating sur-face state of Bi_2Te_3 to prove the existence of single nondegenerate dirac cone in surface state; also indicating a full energy gap for bulk states.	
	Lee and Iizuka [77]	phononic meta-material with C-shaped elements create topological band gap due to the addition of resonance scattering	Band gap at ~5kHz
	Xue et al [78]	higher order topological insulators using kagome lattice structure with cylindrical resonator at each site	
	Weiner et al [79]	3D topological metamaterial displays the analog of pyrochlore lattice and shows topological bulk polarization.	
Viscoelastic Damping System			
Yu et al[84]		optimized formulation for viscoelastic damping of noise control in mid frequency vibro- acoustic systems.	Acoustic energy decrease: ~17.49dB
Feng et al [85]		triple layer adhesive glass capable of minimizing vibration in the existing glass window.	~66.7% reduction in amplitude.
Valvano et al [86]		viscoelastic laminated panels capable of damping band frequencies is used for passive control of noise reduction.	

2.2. Energy Harvesting Based on Sources

Since energy is neither created nor destroyed, the sound and vibration energy that we are filtering using passive control mechanisms can be harvested in the form of electrical energy. The piezoelectric materials can be used to scavenge the unused energy in the form of electrical power. In this section, piezoelectric energy harvesting based on vibration and sound sources can be are reviewed categorically. Piezoelectric materials in the form of solid crystals are used for high energy sources while polymer-based piezoelectric membranes can be used for low-frequency energy sources. The tree diagram represented in Figure 2. 20 helps to understand the classification easily.

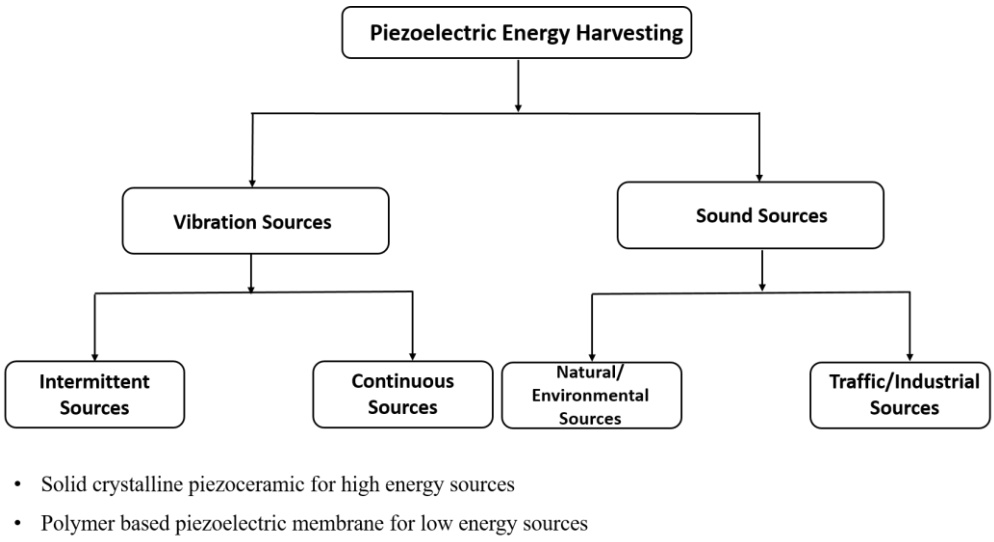

Figure 2. 20: Classification of piezoelectric energy harvesting sources

2.2.1. Vibration Sources

Based on the vibration source, energy harvesting approaches can be classified into two major categories, intermittent and continuous. The continuous source represents the models where the host structure vibrates at specific frequencies or band of frequencies, such as machine vibration. Whereas, the intermittent source doesn't rely on input frequency, however, the host structure deforms and generates power upon the availability of the source, such as footsteps. One major difference between continuous and intermittent sources is in operating principle. While the resonance phenomenon is the key to generating maximum power using the continuous source, the intermittent source uses pure bending mode to harvest energy. Puscasu et al [87] introduced a new technology for converting energy generated from steps into electricity. Their model is built from available piezoelectric membranes arranged in a rectangular array. This model could generate 17.7mJ of useful electrical energy per activation to provide up to 10.6 seconds of light (**Figure 2. 21**). Harvesting energy from vibration is the most common form of energy

harvesting. In most of the cases, cantilever structures are used. Few researchers have used spiral and twisted structures.

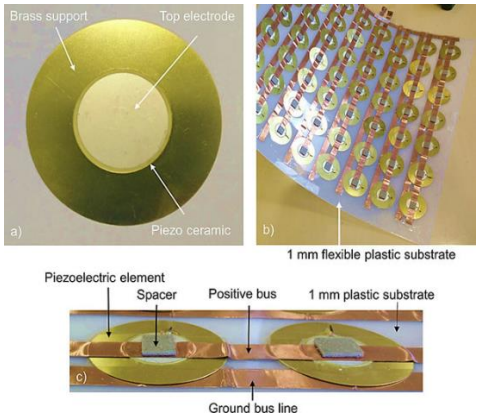

Figure 2. 21: Structure of the energy-harvesting tile active layer using commercially available piezoelectric materials[87]

Lueke et al. [88] presented a folded spring-like structure for vibration-based energy harvesting. Two classes of folded spring energy harvesters were developed. This design is capable of harvesting energy from frequency within 45-3667Hz. This model harvested a maximum 69.5nW at 226.3Hz (Figure 2. 22). Liu et al. [89] developed an S-shaped Mems PZT cantilever which can harvest energy from frequency as low as 30Hz. Few other researchers have also worked on spiral-shaped cantilever energy harvester[90-93].

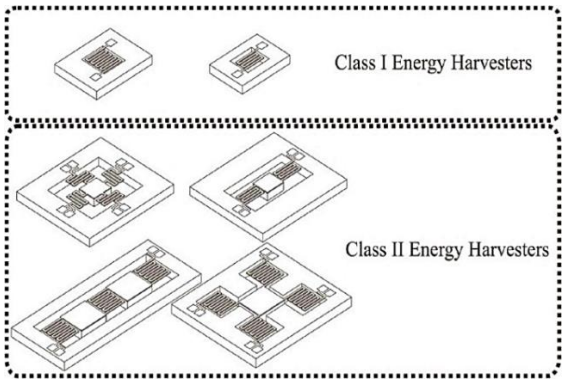

Figure 2. 22: The two classes of energy harvesters: Class I-single folded springs.; Class II-arrays of folded beams including at least one proof mass[88]

In the case of vibration-based energy harvesting, galloping piezoelectric energy harvesters are used in places where there is a chance of induced vibration from airflow. In these models, there is an extra mass attached to the tip of the beam. Self-excited vibration is induced when the tip bluff body is subjected to airflow. Various researchers including Ewere and Wang [94] have studied the performance of galloping energy harvesters[95-98]. Figure 2. 23 represents a schematic of the galloping piezoelectric energy harvester.

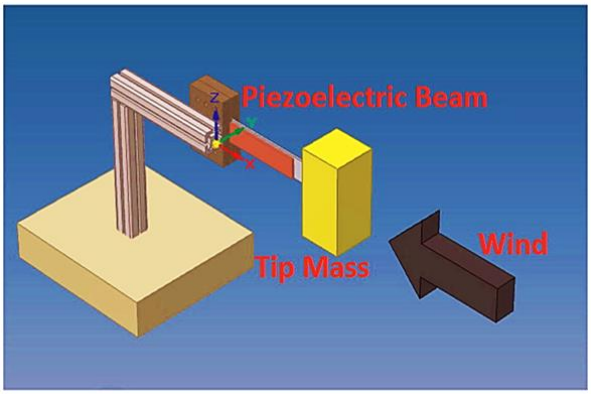

Figure 2. 23: Mechanism of a Galloping Energy Harvester. [94]

Sun et al. proposed a U-shaped vibration-based piezoelectric energy harvester[99]. They investigated the properties of the model analytically and validated the results experimentally. They have also compared linear and non-linear models side by side and found that the nonlinear U shaped model narrows the bandgap. The maximum voltage response changes during up sweeping and down sweeping signals. 8.743 V at 6.5 Hz under the up-sweeping 14.18 V at 15.41 Hz under the down-sweeping signals were recorded. The experimental results demonstrate that the voltage response and the resonance frequency of the U-VPEH agree with the analytical and theoretical analysis. The design is represented in **Figure 2. 24**.

The use of unimorph and bimorph energy harvester is also a developing part of the vibration-based energy harvesting. Depending on the host structure and purpose of the harvester, damping is required for optimum power output. Unimorph is a cantilever-based structure that has one active layer while bimorph has two active layers. Bimorphs can have passive layers in between two active layers. Unimorph and bimorphs are proved to be the most promising method for microscale energy harvesting[100-105].

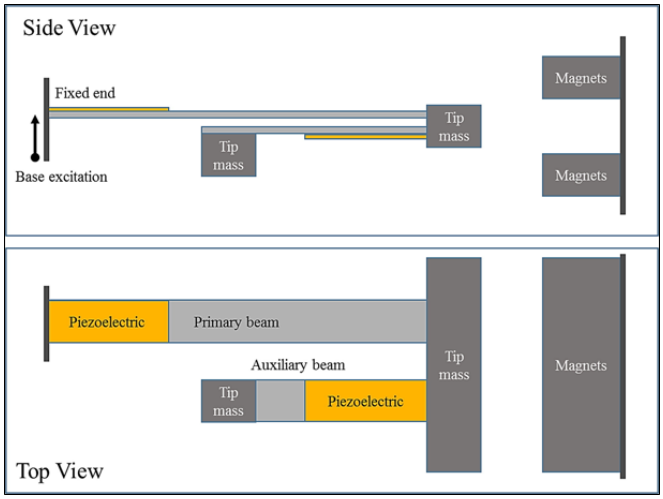

Figure 2. 24: U-VPEH model design proposed by sun et al [99].

Cottone et al. [106] introduced a nonlinear bucked beam-like structure that is studied under the wideband on random vibrations. The design comprises of a thin steel beam with two bonded layers of piezoelectric material (**Figure 2. 25**). Numerical and experimental results are in harmony and they indicate that such structure has extremely high power generation capability when in the buckled state compared to the unbuckled state.

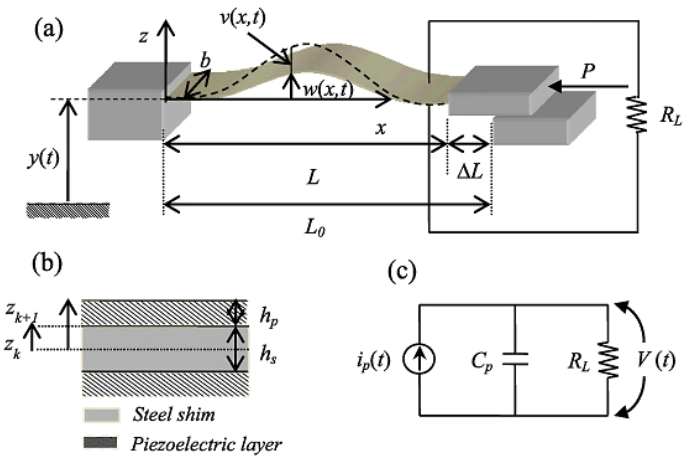

Figure 2. 25: Buckled beam structure for vibration based energy harvesting. [106]

2.2.2. Sound Sources

Generally, acoustic energy is ultimately dissipated into thermal energy at the propagation stage, and low- and midfrequency sound waves have attracted the most attention. One reason is that this frequency band of noise is usually a significant component of the spectrum. The other reason is that in this frequency range, the corresponding sound wavelength is long, making it difficult to absorb or isolate it using most engineering structures. Many approaches have been developed to effectively absorb or isolate low- to midfrequency acoustic sound waves, and these include passive approaches and active approaches. The mechanism of sound energy harvesting can be explained easily from **Figure 2. 26**. The ambient noise passes through either resonator or an acoustic metamaterial where it is trapped. The trapped energy is converted to electric potential using either piezoelectric, electromagnetic, or triboelectric energy conversion mechanism. This energy can be stored in batteries for further application.

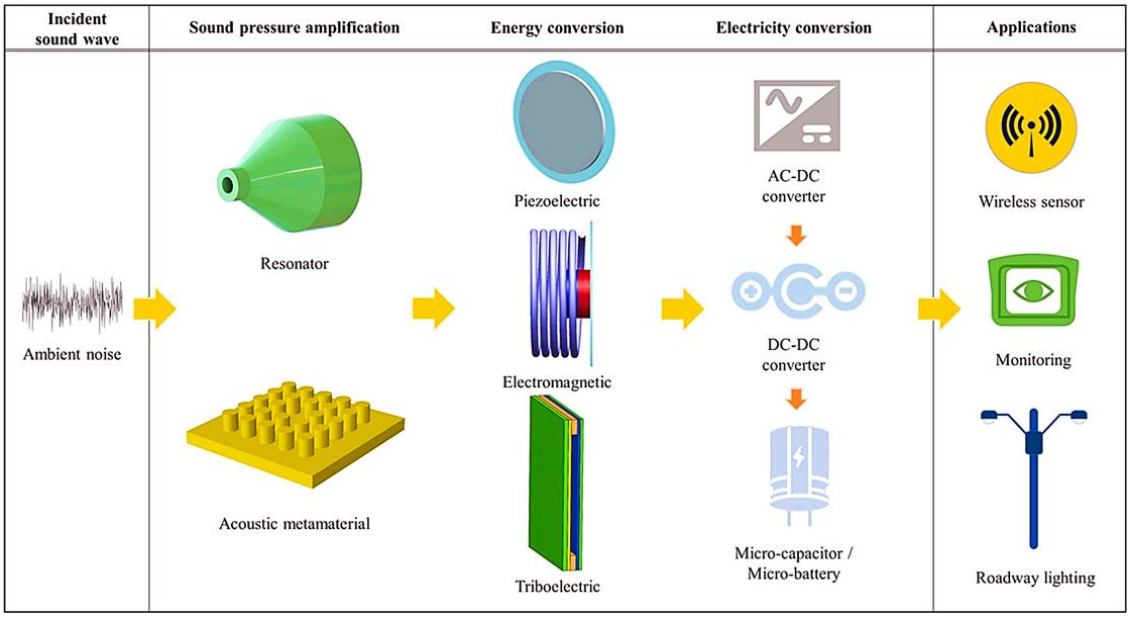

Figure 2. 26: Sound energy harvesting mechanism [107]

Acoustic energy harvesters can be small in size but harvest a significant amount of power output. A combination of metamaterials and membrane type piezoelectric materials are widely used for acoustic energy harvesting. Li et al. reported a membrane-type energy harvester which is also capable of low-frequency sound insulation[108]. The basic structure consists of a circular TPU membrane fixed by a rigid aluminum ring. Rigid Aluminum mass is attached on both sides of the membrane. A flexible PVDF membrane is used for harvesting energy (**Figure 2. 27a**). Results show that power output is observed in the nano Watt scale which is comparatively low. Wang et al [109] proposed a compact acoustic energy harvesting system with a beam-based PZT transducer and a dual-layer of an acoustic metamaterial. To effectively improve the efficiency of the cell, the first bending mode of the transducer is designed to resonating vibration related to the amplification effect. The authors report that under 100 dB incident pressure, the maximum output voltage is calculated to be 72.6mV which is 4.2 times higher compared to the models without

layered metamaterial (**Figure 2. 27b**). An innovative and practical acoustic metamaterial energy harvester is proposed by Qi et al.[110] where a defect is created on the plate to accommodate the PZT patch. From this model, a maximum output voltage of 1.3 V and a power density of 0.54 l W/cm^3 are obtained at a frequency of 2257.5 Hz (Figure 2. 27c). Helical designs have long been in fashion for various purposes. Yuan et al [111] presented a helix structure for low-frequency acoustic energy harvesting which can be 3D printed (**Figure 2. 27e**).

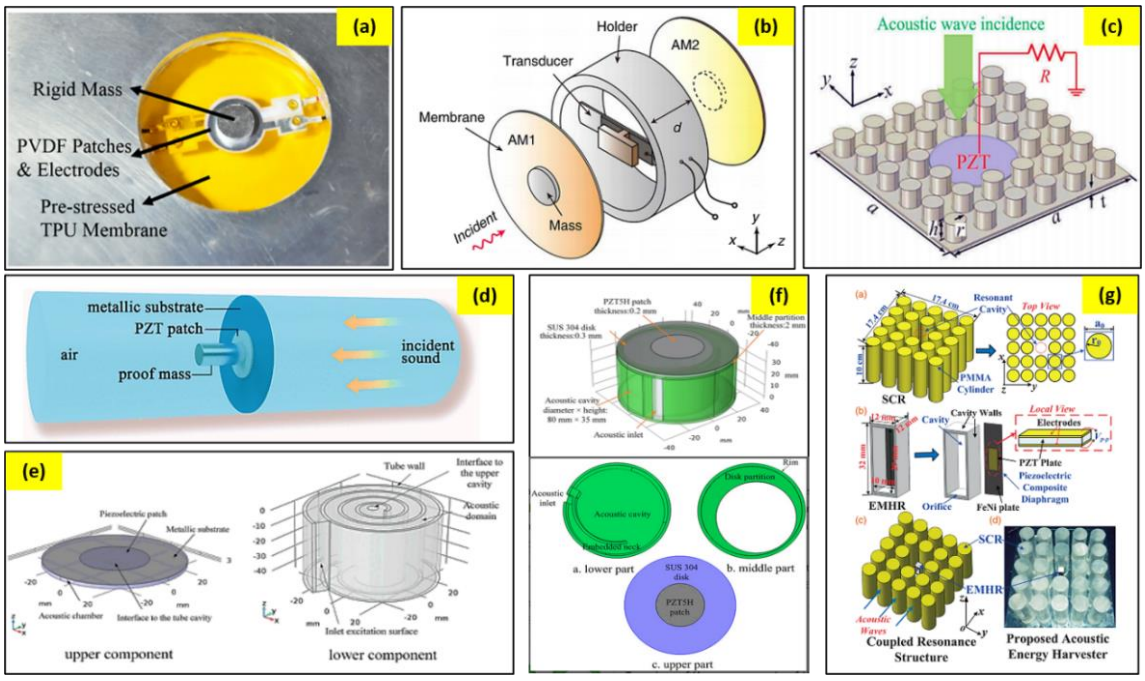

Figure 2. 27: Acoustic energy harvesting structures(a)Membrane type sound absorber and energy harvester [108] (b)compact energy harvester with beam bazed PZT[109] (c)planar acoustic metamaterial[110] (d)energy harvester using a metallic sustrate and a proof mass[112] (e)3D printed helix structure with PZT patch [111](f) Low-frequency acoustic energy harvester based on planar helmholtz resonator[113] (g) acoustic energy harvesting using coupled sonic crystal and helmholtz resonator. [114]

PZT patch is used in the design for energy harvesting which gives a power output of 7.3 µW at acoustic resonance frequency 175 Hz and 100 dB sound pressure level excitation. Few other researchers have also developed helical structures for acoustic energy

harvesting. Yuan et al also reported a metallic substrate with proof mass which harvests energy in the mW range[112]. Sonic crystal and Helmholtz resonator both have been used for waveguiding and energy harvesting for a very long time. Yang et al. have incorporated two basic structures into one module to harvest acoustic energy[114]. Experimental results show that the proposed harvester exhibits ~23 and ~262 times higher maximum harvesting efficiencies than the sonic crystal resonator and the Helmholtz resonator structure, respectively (**Figure 2. 27g**).

2.3. Acoustic Metamaterial with Ventilation

In recent years there have been huge studies conducted on acoustic metamaterials and their use as a noise filtering material. But for most of the designs, there is a prevailing complaint which is blocked airflow.

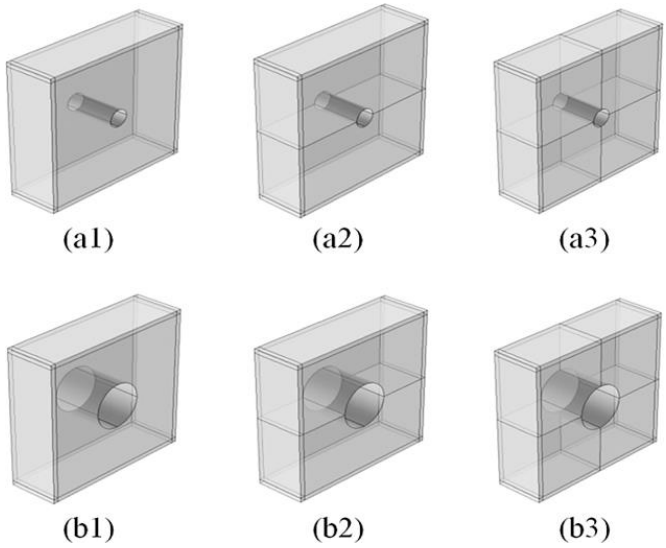

Figure 2. 28: Diffraction resonators or acoustic cells. Diameters of the air holes: 20mm for (a1), (a2), and (a3), and 50mm for (b1), (b2), and (b3). There are three structures: one room for (a1) and (b1), two rooms for (a2) and (b2), and four rooms for (a3) and (b3) [115]

For an enclosed space, it is required that the circulation of fresh air from the external environment is brought into the room. For this reason, acoustic metamaterial design with

ventilation has been developed. Researchers have come up with unique designs of metamaterial-based windows that allow airflow, are lightweight, highly tunable, and can be 3D printed. Recently, Kim and lee presented a soundproof transparent window design with air ventilation[115]. The window design has negative bulk modulus and the reduction in sound level is recorded between 20-35dB in the frequency range of 400-5,000Hz. They studied 6 different designs of the cell to compare the best effective model. The design developed by Kim and Lee could be seen in **Figure 2. 28**.Various other researchers have developed such noise filtering material designs that aid airflow. Few of the recent most effective designs can be seen in **Figure 2.29** [116-121]. These studies indicate that sound transmission can be minimized even by using barriers with air ventilation capacity. These models are an indication that in the near future the noise barrier industry is going to be revolutionized by a new design trend.

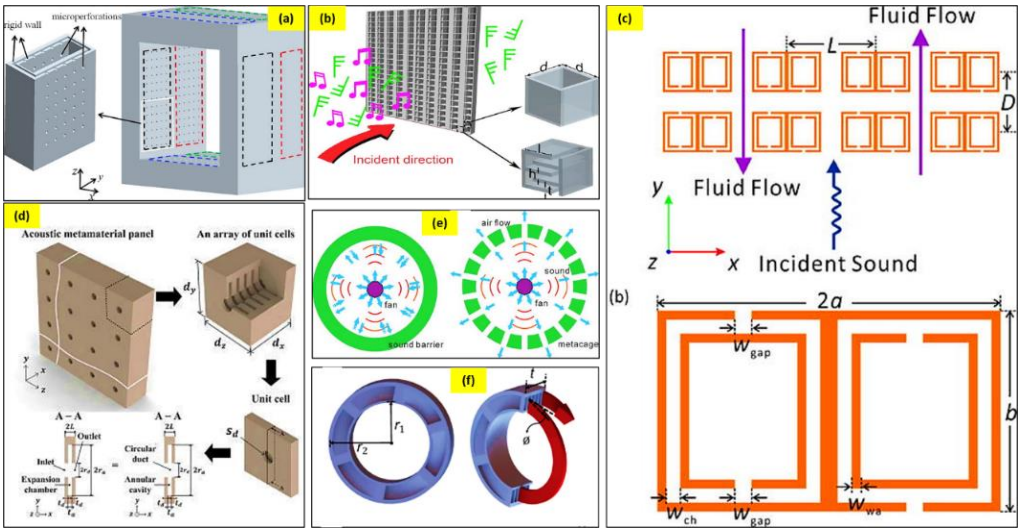

Figure 2.29: Acoustic metamaterials with ventilation for fluid Flow (a) Broadband acoustic absorber with ventilation performance [118] (b) omnidirectional ventilated acoustic barrier[119](c) High efficiency ventilated metamaterial at low frequency[116](d) acoustic metamaterial for fluid passage and soundproofing [121](e)Acoustic metacages with steady air flow [117] (f)Ultra open metamaterial silencer. [120]

Table 2. 3: Energy harvesting based on excitation sources

Vibration sources		
Author	Model Description	Power Output
Puscasu et al [87].	Energy harvesting using pressure and vibration from steps in a busy corridor using piezoelectric membrane.	17.7mJ
Lueke et al. [88]	Fixed-fixed folded spring type vibration-based energy harvester for low frequency energy harvesting.	690.5nW
Liu et al. [89]	S-shaped PZT cantilever for very low frequency (<30Hz) vibration and low acceleration (<0.4g) energy harvester.	40mV
Wen et al[90]	Spiral shaped PVDF cantilever for harvesting energy from low frequency of around 20Hz.	1.8V
Bai et al [91]	Spiral shaped multi modal vibration energy harvester with magnetoelectric transducers as tip mass for low frequency energy harvesting	~24V
Zhao et al. [92]	Spiral shaped thin elastic beam with a PZT layer and proof mass for low frequency energy harvesting	330.8μW
Zorlu et al [93]	Low frequency MEMS energy harvester which generates energy from low displacement amplitude vibrations.	363nW
Ewere & Wang [94]	Galloping piezoelectric energy harvester to use vibration from wind with different tip bluff bodies to characterize its performance.	~9mW
Yan et al [95]	A galloping piezoelectric energy harvester with general EM decoupled model including the derivation and analysis of electrical damping corresponding to Hopfbirufication.	~4mW
Wang et al [97]	Tristable galloping piezoelectric energy harvester using nonlinear magnetic force.	0.73mW
Dash et al [98]	Proposed non-linear EM distributed parameter model for GPEH and effect of different order polynomial for aerodynamic force on dynamic behavior is investigated.	~14mW
Sun et al [99]	Linear and nonlinear U-shaped vibration based energy harvester with tip mass and magnets is investigated	14.18V
Hosseini et al [100]	Comprehensive analysis of the relationship between the shape of the piezoelectric cantilever and voltage output and seducing a rule of thumb for calculation	6.75V

Jemai et al [101]	Unimorph cantilever beam type energy harvester analyzed under nonuniform vibration mode shapes and optimized the performance of the system.	~0.01W
Zeng et al. [102]	Unimorph piezoelectric energy harvester with one through width crack in the form of delamination to study the influence of the delamination on voltage and power output.	$1.8X10^{-19}$
Tsujiura et al. [103]	Thin bimorph cantilever energy harvester capable of generating electric power using the self- excited vibration prompted by continuous air flow.	~53μ
Yeo et al. [104]	Bimorph PCM energy harvester demonstrating high efficiency and power output from low frequency mechanical vibration.	$3.9mWcm^{-2}g^2$
Alsaadi and Sheeraz [105]	A bimorph energy harvester which proves the effect of piezoelectric layer thickness on the energy output.	7W
Cottone et al. [106]	Bistable oscillators exposed to nonlinear vibration which exhibits superior power generation in a wide resistance range.	10^{-1}μW
Sound Sources		
Li et al [108]	Piezoelectric patch on either side of a thin membrane to harvest energy from the strain created in the membrane from sound waves.	~10nW 15.3% (energy conversion efficiency)
Wang et al [109]	Beam based PZT transducer with two layers of acoustic metamaterial which increases the efficiency and power output by 4.2 times than transducer without LAM.	72.6mV
Qi et al [110]	PZT patch attached to a defect in the AMM plate with array of silicone rubber stubs on a thin aluminum plate which harvests energy from acoustic pressure.	1.3 V $0.54\mu W/cm^3$ (power density)
Yuan et al [112]	Helical acoustic resonator which can be 3D printed and occupies less volume is capable of harvesting energy from the piezoelectric patch bonded on the cap using sound pressure.	7.3μW
Yuan et al [111]	A metallic substrate with proof mass is designed to harvest energy from acoustic energy which overcomes the drawbacks of the rubber film.	0.21mW

Yang et al [114]	Coupled acoustic resonance of sonic crystal and Helmholtz resonator to magnify acoustic pressure and harvest higher pressure.	429μW
Yuan et al [113]	Helmholtz resonator with tapered neck and PZT patch on the cover to harvest low frequency acoustic energy.	64.4μW

Since the world is progressing, the need for more cost effective and efficient noise barriers are also becoming a much-needed thing these days. In this review, various designs have been listed and compared. Though most of them have very interesting design and promising output, they are not always feasible for real life application. Apart from having increased manufacturing and installation cost, all of them are not capable of surviving the real-life environment. Again, most of the noise filtering barrier designs are not equipped with energy harvesting capability. Hence, either the existing designs can be modified to be more cost effective and include energy harvesting capability or novel materials can be designed to incorporate the desired properties. Another increasing concern regarding the noise barriers is the issue with air flow. Though most of the designs are very effective in noise filtering, blocking air flow is a concern with almost all of them. Recently many researchers have proposed various designs with enhanced air ventilation facilities. Based on the proposals presented by various researchers in this article, it is evident that such shortcomings can be resolved soon. Overall, a general directive should be developed which includes the discoveries reported so far and the shortcomings that is expected to be resolved.

This chapter presents a detailed review of the metamaterials developed so far that can be used for active noise filtering and energy harvesting. The entire study is divided into major sections for the ease of understanding. Based on what appears in the present review few conclusions can be drawn. Though various models have been developed for noise

controlling purposes and the structures have shown promising output in the laboratory experiments, still many of them have complexities associated with them which makes it hard to be transferred to the real-world scenario. Similarly, the metamaterials with energy harvesting capability have comparatively lower power harvesting capability. Further research needs to be conducted to increase the power output from such smart materials. However, one of the major concerns with traditional noise barriers is blocked air flow and it is very impressive to learn that many researchers have worked on developing noise filters with ventilation for fluid flow. So far these have only been used for acoustic noise filters, but we believe that advanced research in future can incorporate smart materials in such systems to harvest energy from the structures simultaneously.

CHAPTER 3

Mathematical Model Development

This chapter presents a predictive analytical model which ensures energy harvesting from a thin plate or membrane with a piezoelectric layer with certain constraints. The derivation of the coupled dynamic equation for the plate type energy harvester where a unimorph thin membrane is considered with piezoelectric ring on the top of the host membrane is presented here. The piezoelectric ring is assumed to be placed on top of the membrane in the form of a ring. A generalized model is proposed to find analytically the voltage output from any arbitrary shape of a piezoelectric layer placed at any arbitrary location on the substrate. A dynamic equation where there is a resonator attached on the membrane and coupled with a feedback voltage or power generation equation is proposed after considering the strain-rate damping mechanism. The proposed predictive model could potentially be helpful to optimize the placement of such small segments of piezoelectric layers or electrodes in a required pattern according to the shape or design of the structure. Such a design approach would need an accurate mathematical model that can be used for predictive design of the customized harvesters.

The proposed mathematical model is versatile enough to be formulated for different application The electrodes are assumed to cover the entire surface on either side of the piezoelectric layer. In this derivation, the assembly is assumed to be a thin membrane and Love-Kirchhoff's assumptions are valid. The strain along the thickness direction of the

plate is assumed to be zero. The piezoelectric layer is assumed to be thin compared to the membrane thickness. The mechanical damping is separated in two parts including Kelvin–Voigt and air damping. The electrodes on either side of the piezoelectric layers are assumed to be perfectly conductive.

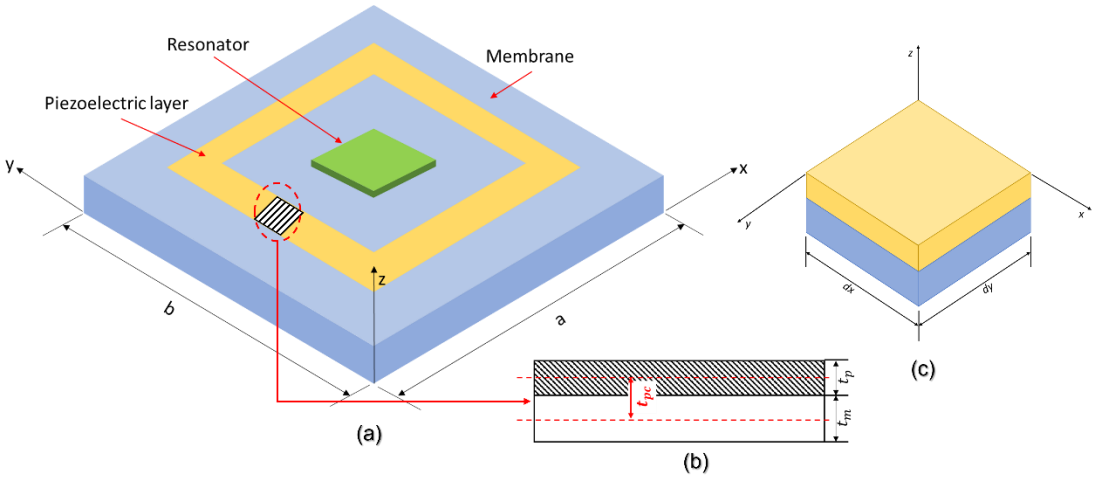

Figure 3. 1: (a) schematic of a unit cell with piezoelectric ring (b) cross sectional view of the layers representing the orientation and thickness (c) an element from the unit cell.

An element of dx by dy taken from the plate (figure 3.1(c)) is considered for the following derivation. This small segment size can be varied to fit into any model. Figure 3.2 shows an example of how this element can be adjusted to fit a circular ring. Though the model demonstrates the process of finding the voltage and power in a square element, this element can be used in any finite element model by changing the element size as per design requirement. Thus this model can be used as a universal model for any arbitrary shape and size. A resistive load (R_L) is considered in the energy-harvesting circuit for developing the governing equation. When small segments of piezoelectric patches are considered, the total circuit resistance is assumed to be contributed through the parallel connection of effective resistance for individual patches. It is assumed that the electric field is bound to develop only along the z-direction. Hence, the electric field strength developed

along the x- and y-axes was zero. In figure 3.1 a small rectangular element between x_i and x_{i+1} along x and between y_i and y_{i+1} along y is considered in the following derivation.

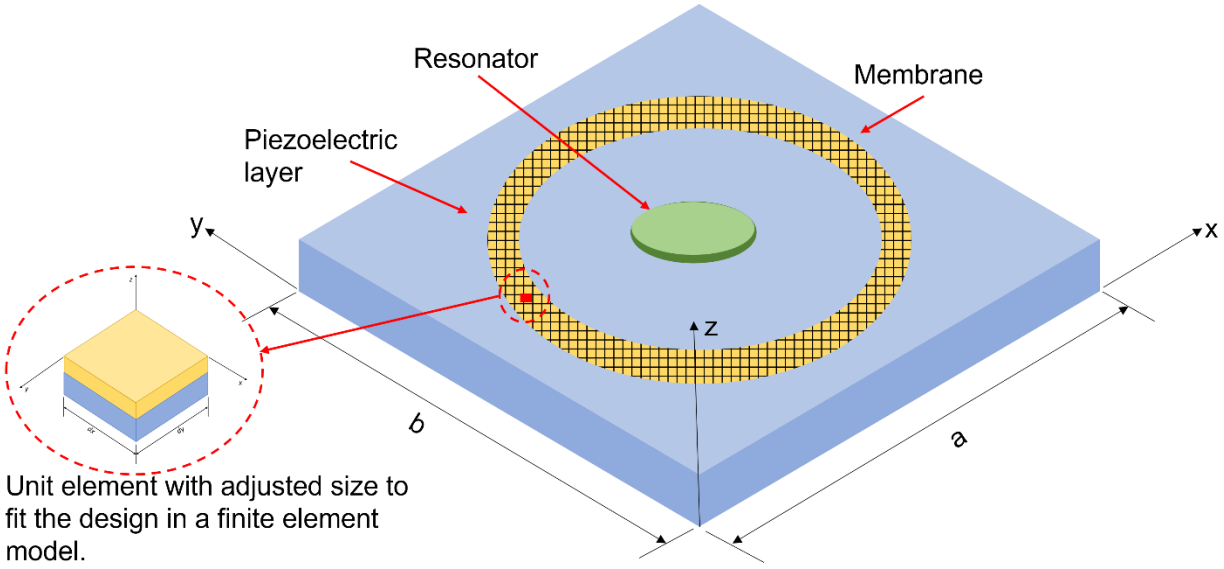

Figure 3. 2 : Adjusting the element size to be formulated into various shapes in a finite element model

The governing differential equation of a membrane with a resonator experiencing transverse loading under dynamic conditions can be written as

$$\frac{\partial^2 M_x}{\partial x^2} + \frac{\partial^2 M_y}{\partial y^2} - \frac{\partial^2 M_{xy}}{\partial x \partial y} = -\left[-m\frac{\partial^2(\omega+\omega_b)}{\partial t^2} - q - \sum_{r=1}^{N} m_r \frac{\partial^2 \omega(\xi_i \eta_i)}{\partial t^2}\,\delta(x-\xi_i)\delta(y-\eta_i)\right] \quad \text{.....Eq 3. 1}$$

Here, $M_x \; and \; M_y$ are the moments per unit length along the x and y axis respectively while M_{xy} is the moment resulting from shear stress. Expression for the moments in the plate can be expressed in the form of integration of the stress distribution over the cross section of the membrane and the piezoelectric material thickness. Here p is used to address piezoelectric layer and m is used for membrane. $t_m and \; t_p$ are the thickness of the membrane and the piezoelectric layer.

$$M_x = \int_0^{t_m+t_p} \sigma_{xx} z \, dz$$

$$M_x = \int_0^{t_m} \sigma_{xx}^m z \, dz + \int_{t_m}^{t_p} \sigma_{xx}^p z \, dz \ldots\ldots\ldots\ldots\ldots\ldots\ldots\ldots\ldots\ldots\ldots\ldots \text{Eq 3. 2}$$

$$M_y = \int_0^{t_m} \sigma_{yy} z \, dz + \int_{t_m}^{t_p} \sigma_{yy} z \, dz \ldots\ldots\ldots\ldots\ldots\ldots\ldots\ldots\ldots\ldots\ldots\ldots \text{Eq 3. 3}$$

$$M_{xy} = \int_0^{t_m} \sigma_{xy} z \, dz + \int_{t_m}^{t_p} \sigma_{xy} z \, dz \ldots\ldots\ldots\ldots\ldots\ldots\ldots\ldots\ldots\ldots\ldots\ldots \text{Eq 3. 4}$$

Following equations are standard outcomes while deriving a plate equation. The piezoelectric constitutive relation can be written as

$$\left.\begin{array}{c} \boldsymbol{S} = s^E \boldsymbol{T} + \boldsymbol{d}^t E \\ \boldsymbol{D} = d^t \boldsymbol{T} + \varepsilon^T \boldsymbol{E} \\ \boldsymbol{S} = s^D \boldsymbol{T} + g^t \boldsymbol{D} \\ \boldsymbol{E} = -g\boldsymbol{T} + +\varepsilon^{T-1} \boldsymbol{D} \\ \boldsymbol{S}^P = s^p \boldsymbol{T}^p + d^t \boldsymbol{E} \end{array}\right\} \ldots\ldots\ldots\ldots\ldots\ldots\ldots\ldots \text{Eq 3. 5}$$

Here, $\mathbf{S}^p$ is strain tensor, $\mathbf{T}^p$ is stress tensor, [**d**] is the matrix for direct piezoelectric effect consists of piezoelectric charge constants and **E** is the induced or generated electric filed strength. Where C is constitutive matrix; and D is the coupled strain rate damping matrix.

$$\begin{bmatrix} \sigma_{11} \\ \sigma_{22} \\ \sigma_{12} \end{bmatrix}^m = \begin{bmatrix} C_{11} & C_{12} & C_{13} \\ C_{21} & C_{22} & C_{23} \\ C_{31} & C_{32} & C_{33} \end{bmatrix}^m \begin{Bmatrix} \varepsilon_{11} \\ \varepsilon_{22} \\ \varepsilon_{12} \end{Bmatrix}^m \ldots\ldots\ldots\ldots\ldots\ldots\ldots\ldots\ldots\ldots \text{Eq 3. 6}$$

$$\begin{Bmatrix} \varepsilon_{11} \\ \varepsilon_{22} \\ \varepsilon_{12} \end{Bmatrix}^p = \begin{bmatrix} S_{11} & S_{12} & S_{13} \\ S_{21} & S_{22} & S_{23} \\ S_{31} & S_{32} & S_{33} \end{bmatrix}^p \begin{Bmatrix} \sigma_{11} \\ \sigma_{22} \\ \sigma_{12} \end{Bmatrix}^p + \begin{bmatrix} 0 & 0 & d_{31} \\ 0 & 0 & d_{32} \\ 0 & 0 & d_{33} \end{bmatrix} \begin{Bmatrix} E_1 \\ E_2 \\ E_3 \end{Bmatrix} \ldots\ldots\ldots\ldots\ldots\ldots \text{Eq 3. 7}$$

In order to find stress in piezoelectric layer, the equation can be expressed as:

$$\boldsymbol{T}^p = s^{p^{-1}} [\boldsymbol{S}^p - \boldsymbol{d}^T \boldsymbol{E}] = c^p \boldsymbol{S}^p - c^p \boldsymbol{d}^T \boldsymbol{E} = c^p \boldsymbol{S}^p - e^p \boldsymbol{E} \ldots\ldots\ldots\ldots\ldots\ldots \text{Eq 3. 8}$$

$$\begin{Bmatrix}\sigma_{11}\\ \sigma_{22}\\ \sigma_{12}\end{Bmatrix}^p = \begin{bmatrix}C_{11} & C_{12} & C_{13}\\ C_{21} & C_{22} & C_{23}\\ C_{31} & C_{32} & C_{33}\end{bmatrix}^p \begin{Bmatrix}\varepsilon_{11}\\ \varepsilon_{22}\\ \varepsilon_{12}\end{Bmatrix}^p + \begin{bmatrix}C_{srx} & C_{sry} & 0\\ C_{sry} & C_{srx} & 0\\ 0 & 0 & 0\end{bmatrix}\begin{Bmatrix}\dot{\varepsilon_{11}}\\ \dot{\varepsilon_{22}}\\ \dot{\varepsilon_{12}}\end{Bmatrix} + \begin{bmatrix}C_{11} & C_{12} & C_{13}\\ C_{21} & C_{22} & C_{23}\\ C_{31} & C_{32} & C_{33}\end{bmatrix}^p \begin{bmatrix}0 & 0 & d_{31}\\ 0 & 0 & d_{32}\\ 0 & 0 & d_{33}\end{bmatrix}\begin{Bmatrix}E_1\\ E_2\\ E_3\end{Bmatrix} \quad \text{..... Eq 3. 9}$$

For piezoelectric layer, $C_{13} = C_{31} = C_{32} = C_{23} = 0$. So, the stress turns out to be as follows

$$\left.\begin{aligned}\sigma_{xx}^p &= \left(C_{11}^p\varepsilon_{11} + C_{12}^p\varepsilon_{22}\right) + \left(C_{srx}\dot{\varepsilon_{11}} + C_{sry}\dot{\varepsilon_{22}}\right) - \left[C_{11}^p d_{31} + C_{12}^p d_{32}\right]E_3\\ \sigma_{yy}^p &= \left(C_{21}^p\varepsilon_{11} + C_{22}^p\varepsilon_{22}\right) + \left(C_{srx}\dot{\varepsilon_{11}} + C_{sry}\dot{\varepsilon_{22}}\right) - \left[C_{21}^p d_{31} + C_{22}^p d_{32}\right]E_3\\ \sigma_{xy}^p &= C_{33}\varepsilon_{12} - {C_{33}}^p d_{33}E_3\\ \sigma_{xx}^m &= C_{11}^m\varepsilon_{11} + C_{12}^m\varepsilon_{22}\\ \sigma_{yy}^m &= C_{21}^m\varepsilon_{11} + C_{22}^m\varepsilon_{22}\\ \sigma_{xy}^m &= C_{33}^m\varepsilon_{12}^m\end{aligned}\right\} \text{... Eq 3. 10}$$

C_{srx} and C_{sry} are the strain rate damping coefficient. Substituting the values from Eq 3.10 in the moment equation we get

$$M_x = \int_0^{t_m}\sigma_{xx}^m z\,dz + \int_{t_m}^{t_p}\sigma_{xx}^p z\,dz$$

$$\begin{aligned}M_x = \int_0^{t_m}\left(C_{11}^m\frac{\partial^2\omega}{\partial x^2} + C_{12}^m\frac{\partial^2\omega}{\partial y^2}\right)z^2\,dz - \int_{t_m}^{t_p}\left(C_{11}^p\frac{\partial^2\omega}{\partial x^2} + C_{12}^p\frac{\partial^2\omega}{\partial y^2}\right)z^2\,dz\\ - \int_{t_m}^{t_p}\left(C_{srx}\frac{\partial^3\omega}{\partial t\partial x^2} + C_{sry}\frac{\partial^3\omega}{\partial t\partial y^2}\right)z^2\,dz\\ - \int_{t_m}^{t_p}\left(C_{11}^p d_{31} + C_{12}^p d_{32}\right)E_3 z\,dz\end{aligned}$$

$$\begin{aligned}M_x = -\frac{t_m^3}{3}\left[C_{11}^m\frac{\partial^2\omega}{\partial x^2} + C_{12}^m\frac{\partial^2\omega}{\partial y^2}\right] + \left(\frac{t_m^3}{3} - \frac{t_p^3}{3}\right)\left[C_{11}^p\frac{\partial^2\omega}{\partial x^2} + C_{12}^p\frac{\partial^2\omega}{\partial y^2}\right]\\ + \left(\frac{t_m^3}{3} - \frac{t_p^3}{3}\right)\left[C_{srx}\frac{\partial^3\omega}{\partial x^2\partial t} + C_{sry}\frac{\partial^3\omega}{\partial y^2\partial t}\right]\\ + \left(\frac{t_m^2}{2} - \frac{t_p^2}{2}\right)\left[\left(C_{11}^p d_{31} + C_{12}^p d_{32}\right)E_3\right] \quad \text{..... Eq 3. 11}\end{aligned}$$

*S*imilarly,

$$M_y = -\frac{t_m^3}{3}\left[C_{21}^m \frac{\partial^2\omega}{\partial x^2} + C_{22}^m \frac{\partial^2\omega}{\partial y^2}\right] + \left(\frac{t_m^3}{3} - \frac{t_p^3}{3}\right)\left[C_{21}^p \frac{\partial^2\omega}{\partial x^2} + C_{22}^p \frac{\partial^2\omega}{\partial y^2}\right]$$
$$- \left(\frac{t_m^3}{3} - \frac{t_p^3}{3}\right)\left[C_{sry}\frac{\partial^3\omega}{\partial x^2\partial t} + C_{srx}\frac{\partial^3\omega}{\partial y^2\partial t}\right]$$
$$+ \left(\frac{t_m^2}{2} - \frac{t_p^2}{2}\right)\left[\left(C_{21}^p d_{31} + C_{22}^p d_{32}\right)E_3\right] \text{ ..... Eq 3. 12}$$

and $M_{xy} = -\int_0^{t_m} C_{33}^m \frac{\partial^2\omega}{\partial x\partial y} z^2\, dz - \int_{t_m}^{t_p} C_{33}^p \frac{\partial^2\omega}{\partial x\partial y} z^2\, dz - \int_{t_m}^{t_p} E_3 C_{33}^p d_{33} z\, dz$

$$M_{xy} = \left(-\frac{t_m^3}{3}\right) C_{33}^m \frac{\partial^2\omega}{\partial x\partial y} + C_{33}^p \frac{\partial^2\omega}{\partial x\partial y}\left(\frac{t_m^3}{3} - \frac{t_p^3}{3}\right) + E_3 C_{33}^p d_{33}\left(\frac{t_m^2}{2} - \frac{t_p^2}{2}\right) \text{ ... ... Eq 3. 13}$$

Further finding the derivatives of the moments for substituting in Eq 3.1

$$\frac{\partial^2 M_x}{\partial x^2} = -\frac{t_m^3}{3}\left[C_{11}^m \frac{\partial^4\omega}{\partial x^4} + C_{12}^m \frac{\partial^4\omega}{\partial x^2\partial y^2}\right] + \left(\frac{t_m^3}{3} - \frac{t_p^3}{3}\right)\left[C_{11}^p \frac{\partial^4\omega}{\partial x^4} + C_{12}^p \frac{\partial^4\omega}{\partial x^2\partial y^2}\right]$$
$$+ \left(\frac{t_m^3}{3} - \frac{t_p^3}{3}\right)\left[C_{srx}\frac{\partial^5\omega}{\partial x^4\partial t} + C_{sry}\frac{\partial^5\omega}{\partial x^2\partial y^2\partial t}\right]$$
$$+ \left(\frac{t_m^2}{2} - \frac{t_p^2}{2}\right)\frac{d^2}{dx^2}\left[\left(C_{11}^p d_{31} + C_{12}^p d_{32}\right)E_3\right] \text{ ..... Eq 3. 14}$$

$$\frac{\partial^2 M_y}{\partial y^2} = -\frac{t_m^3}{3}\left[C_{21}^m \frac{\partial^4\omega}{\partial x^2\partial y^2} + C_{22}^m \frac{\partial^4\omega}{\partial y^4}\right] + \left(\frac{t_m^3}{3} - \frac{t_p^3}{3}\right)\left[C_{21}^p \frac{\partial^4\omega}{\partial x^2\partial y^2} + C_{22}^p \frac{\partial^4\omega}{\partial y^4}\right]$$
$$+ \left(\frac{t_m^3}{3} - \frac{t_p^3}{3}\right)\left[C_{sry}\frac{\partial^5\omega}{\partial x^2\partial y^2\partial t} + C_{srx}\frac{\partial^5\omega}{\partial y^4\partial t}\right]$$
$$+ \left(\frac{t_m^2}{2} - \frac{t_p^2}{2}\right)\frac{d^2}{dy^2}\left[\left(C_{21}^p d_{31} + C_{22}^p d_{32}\right)E_3\right] \text{ ... ... } \textit{Eq 3. 15}$$

$$\frac{\partial^2 M_{xy}}{\partial x\partial y} = \left(-\frac{t_m^3}{3}\right) C_{33}^m \frac{\partial^4\omega}{\partial x^2\partial y^2} + \left(\frac{t_m^3}{3} - \frac{t_p^3}{3}\right) C_{33}^p \frac{\partial^4\omega}{\partial x^2\partial y^2}$$
$$+ \left(\frac{t_m^2}{2} - \frac{t_p^2}{2}\right)\frac{d^2}{dxdy}\left[E_3 C_{33}^p d_{33}\right] \text{ ..... Eq 3. 16}$$

$$\frac{\partial^2 M_x}{\partial x^2} + \frac{\partial^2 M_y}{\partial y^2} - \frac{\partial^2 M_{xy}}{\partial x \partial y} = \frac{\partial^4 \omega}{\partial x^4}\left[C_{11}^m\left(-\frac{t_m^3}{3}\right) + C_{11}^p\left(\frac{t_m^3}{3} - \frac{t_p^3}{3}\right)\right]$$

$$+ \frac{\partial^4 \omega}{\partial y^4}\left[C_{22}^m\left(-\frac{t_m^3}{3}\right) + + C_{22}^p\left(\frac{t_m^3}{3} - \frac{t_p^3}{3}\right)\right]$$

$$+ \frac{\partial^4 \omega}{\partial x^2 \partial y^2}\left[\left(-\frac{t_m^3}{3}\right)[C_{12}^m + C_{21}^m] + \left(\frac{t_m^3}{3} - \frac{t_p^3}{3}\right)[C_{12}^p + C_{21}^p]\right.$$

$$+ \frac{d}{dt}\left[\frac{\partial^4 \omega}{\partial x^2 \partial y^2}\right]\left(\frac{t_m^3}{3} - \frac{t_p^3}{3}\right)2C_{sry}\Big] + \frac{d}{dt}\left[\frac{\partial^4 \omega}{\partial x^2 \partial y^2}\right]\left(\frac{t_m^3}{3} - \frac{t_p^3}{3}\right)C_{srx}$$

$$+ \frac{d}{dt}\left[\frac{\partial^4 \omega}{\partial x^2 \partial y^2}\right]\left(\frac{t_m^3}{3} - \frac{t_p^3}{3}\right)C_{srx}$$

$$+ \left(\frac{t_m^2}{2} - \frac{t_p^2}{2}\right)\left[\frac{d^2}{dx^2}(V_x) + \frac{d^2}{dy^2}(V_y) - 2\frac{d^2}{dxdy}(V_{xy})\right] \ldots\ldots\ldots\ldots \text{ Eq 3. 17}$$

Now, let us assume

$$\psi_1 = C_{11}^m\left(-\frac{t_m^3}{3}\right) + C_{11}^p\left(\frac{t_m^3}{3} - \frac{t_p^3}{3}\right) \ldots\ldots\ldots\ldots\ldots\ldots\ldots\ldots\ldots\ldots\ldots\ldots\ldots\ldots\ldots\ldots\ldots\text{Eq 3. 18}$$

$$\psi_2 = \left(-\frac{t_m^3}{3}\right)2C_{12}^m + \left(\frac{t_m^3}{3} - \frac{t_p^3}{3}\right)2C_{12}^p - \left[\left(-\frac{t_m^3}{3}\right)2C_{33}^m + \left(\frac{t_m^3}{3} - \frac{t_p^3}{3}\right)C_{33}^p\right]$$

Simplifying this equation for ψ_2,

$$\psi_2 = \left(-\frac{t_m^3}{3}\right)(C_{33}^m - C_{12}^m) + \left(\frac{t_m^3}{3} - \frac{t_p^3}{3}\right)(C_{33}^p - C_{12}^p) \ldots\ldots\ldots\ldots\ldots\ldots\ldots\ldots\ldots\ldots\ldots\ldots\ldots\text{Eq 3. 19}$$

$$\psi_3 = C_{22}^m\left(-\frac{t_m^3}{3}\right) + C_{22}^p\left(\frac{t_m^3}{3} - \frac{t_p^3}{3}\right) \ldots\ldots\ldots\ldots\ldots\ldots\ldots\ldots\ldots\ldots\ldots\ldots\ldots\ldots\ldots\ldots\ldots\ldots\text{ Eq 3. 20}$$

Also, assuming

$$\left.\begin{aligned} \varphi_1 &= \left(\frac{t_m^3}{3} - \frac{t_p^3}{3}\right)C_{srx} \\ \varphi_2 &= \left(\frac{t_m^3}{3} - \frac{t_p^3}{3}\right)2C_{sry} \\ \varphi_3 &= \left(\frac{t_m^3}{3} - \frac{t_p^3}{3}\right)C_{srx} \end{aligned}\right\} \ldots\ldots\ldots\ldots\ldots\ldots\ldots\ldots\ldots\ldots\ldots\ldots\ldots\ldots\text{Eq 3. 21}$$

Here, $\varphi_1 = \varphi_3$. Now, without simplifying the voltage terms, and substituting values from Eq 3.15 to Eq 3.18 in Eq 3.14, the moment equation turns out to be

$$\left[\psi_1 \frac{\partial^4 \omega}{\partial x^4} - 2\psi_2 \frac{\partial^4 \omega}{\partial x^2 \partial y^2} + \psi_3 \frac{\partial^4 \omega}{\partial y^4}\right] + \frac{d}{dt}\left[\varphi_1 \frac{\partial^4 \omega}{\partial x^4} + \varphi_2 \frac{\partial^4 \omega}{\partial x^2 \partial y^2} + \varphi_3 \frac{\partial^4 \omega}{\partial y^4}\right]$$

$$+\left(\frac{t_m^2}{2} - \frac{t_p^2}{2}\right)\left[\frac{d^2}{dx^2}(V_x) + \frac{d^2}{dy^2}(V_y) - 2\frac{d^2}{dxdy}(V_{xy})\right] = -m\frac{\partial^2(\omega + \omega_b)}{\partial t^2} - q$$

$$+\sum_{r=1}^{N} m_r \frac{\partial^2 \omega(\xi_i \eta_i)}{\partial t^2} \delta(x - \xi_i)\delta(y - \eta_i) \ldots\ldots\ldots\ldots\ldots\ldots\ldots\ldots\ldots\ldots \text{Eq } 3.22$$

From the moment equations, the voltage terms can be collected to process the equations further.

$$V_x = E_3\left(C_{11}^p d_{31} + C_{12}^p d_{31}\right)$$

$$= \frac{V(t)}{t_p} H(x)H(y)e_{31}$$

$$= \frac{V(t)}{t_p} [H(x - x_i) - H(x - x_{i+1})][H(y - y_i) - H(y - y_{i+1})]e_{31}$$

$$= \frac{V(t)}{t_p} e_{31}(S_{xy}) \ldots\ldots\ldots\ldots\ldots\ldots\ldots\ldots\ldots\ldots\ldots\ldots\ldots\ldots\ldots\ldots\ldots\ldots Eq\ 3.23$$

$$V_y = E_3\left(C_{21}^p d_{31} + C_{22}^p d_{32}\right)$$

$$= \frac{V(t)}{t_p} H(x)H(y)e_{32}$$

$$= \frac{V(t)}{t_p} [H(x - x_i) - H(x - x_{i+1})][H(y - y_i) - H(y - y_{i+1})]e_{32}$$

$$= \frac{V(t)}{t_p} e_{32}(S_{xy}) \ldots\ldots\ldots\ldots\ldots\ldots\ldots\ldots\ldots\ldots\ldots\ldots\ldots\ldots\ldots\ldots\ldots\ldots Eq\ 3.24$$

$$V_{xy} = E_3 C_{33}^p d_{33}$$

$$= \frac{V(t)}{t_p} [H(x - x_i) - H(x - x_{i+1})][H(y - y_i) - H(y - y_{i+1})]e_{33}$$

$$= \frac{V(t)}{t_p} e_{33}(S_{xy}) \ldots\ldots\ldots\ldots\ldots\ldots\ldots\ldots\ldots\ldots\ldots\ldots\ldots\ldots\ldots\ldots\ldots\ldots Eq\ 3.25$$

Now, substituting the collected and assumed variable in the governing differential equation, we find:

$$\left[\psi_1 \frac{\partial^4 \omega}{\partial x^4} - 2\psi_2 \frac{\partial^4 \omega}{\partial x^2 \partial y^2} + \psi_3 \frac{\partial^4 \omega}{\partial y^4}\right] + \frac{d}{dt}\left[\varphi_1 \frac{\partial^4 \omega}{\partial x^4} + \varphi_2 \frac{\partial^4 \omega}{\partial x^2 \partial y^2} + \varphi_3 \frac{\partial^4 \omega}{\partial y^4}\right]$$

$$+\left(\frac{t_m^2}{2} - \frac{t_p^2}{2}\right)\frac{V(t)}{t_p}\left[e_{31}\frac{d^2 S_{xy}}{dx^2} + e_{32}\frac{d^2 S_{xy}}{dy^2} - 2e_{33}\frac{d^2 S_{xy}}{dxdy}\right] = -m\frac{\partial^2(\omega + \omega_b)}{\partial t^2} - q$$

$$+\sum_{r=1}^{N} m_r \frac{\partial^2 \omega(\xi_i \eta_i)}{\partial t^2}\delta(x - \xi_i)\delta(y - \eta_i) \ldots\ldots\ldots\ldots\ldots\ldots Eq\ 3.26$$

Here, S_{xy} is the Heaviside step function which turns out to be 1 when x>a condition is met.

$$S_{xy} = [H(x - x_i) - H(x - x_{i+1})][H(y - y_i) - H(y - y_{i+1})]$$

Viscous air damping is a simple way of modeling the force acting on the plate attributable to the air particles displaced by the plate, and SRD accounts for the structural damping attributable to the friction from the internal constitution of the plate. Eq 3.26 is the dynamic equation of the electric circuit with mechanical coupling. The electric charge density in the piezoelectric layer can be calculated using Gauss law

$$q(t) = \int_A \boldsymbol{D}.ndA \ldots\ldots\ldots\ldots\ldots\ldots\ldots\ldots\ldots\ldots\ldots\ldots\ldots\ldots\ldots\ldots \text{Eq 3. 27}$$

Here, **D** is the charge density value, A is the electrode area over the piezoelectric layer and q(t) is electric charge developed between the electrodes.

Now, we know that charge density equation can be expressed as

$$\mathbf{D} = d\sigma + \varepsilon_r E$$

So, $\begin{Bmatrix} D_1 \\ D_2 \\ D_3 \end{Bmatrix} = \begin{bmatrix} 0 & 0 & 0 & 0 & 0 & 0 \\ 0 & 0 & 0 & 0 & 0 & 0 \\ d_{31} & d_{32} & d_{33} & 0 & 0 & 0 \end{bmatrix} \begin{Bmatrix} \sigma_{11} \\ \sigma_{22} \\ \sigma_{33} \\ \sigma_{12} \\ \sigma_{23} \\ \sigma_{31} \end{Bmatrix} + \begin{bmatrix} \varepsilon_p^{11} & 0 & 0 \\ 0 & \varepsilon_p^{22} & 0 \\ 0 & 0 & \varepsilon_p^{33} \end{bmatrix} \begin{Bmatrix} E_1 \\ E_2 \\ E_3 \end{Bmatrix}$

$$D_3 = \left[-\left(z\frac{\partial^2\omega}{\partial x^2} C_{11}^p + z\frac{\partial^2\omega}{\partial y^2} C_{12}^p \right) - \left(z\frac{\partial}{\partial t}\frac{\partial^2\omega}{\partial x^2} C_{srx} + z\frac{\partial}{\partial t}\frac{\partial^2\omega}{\partial y^2} C_{sry} \right) - E_3\left(C_{11}^p d_{31} + C_{12}^p d_{32} \right) \right] d_{31} + \left[-\left(z\frac{\partial^2\omega}{\partial x^2} C_{21}^p + z\frac{\partial^2\omega}{\partial y^2} C_{22}^p \right) - \left(z\frac{\partial}{\partial t}\frac{\partial^2\omega}{\partial x^2} C_{sry} + z\frac{\partial}{\partial t}\frac{\partial^2\omega}{\partial y^2} C_{srx} \right) - E_3\left(C_{21}^p d_{31} + C_{22}^p d_{32} \right) \right] d_{32} + \varepsilon_{33}^p E_3$$

$$D_3 = -\left(z\frac{\partial^2\omega}{\partial x^2} C_{11}^p + z\frac{\partial^2\omega}{\partial y^2} C_{12}^p \right) d_{31} - \left(z\frac{\partial^2\omega}{\partial x^2} C_{21}^p + z\frac{\partial^2\omega}{\partial y^2} C_{22}^p \right) d_{32}$$

$$-\frac{\partial}{\partial t}\left(z\frac{\partial^2\omega}{\partial x^2} C_{srx} + z\frac{\partial^2\omega}{\partial y^2} C_{sry} \right) d_{31} - \frac{\partial}{\partial t}\left(z\frac{\partial^2\omega}{\partial x^2} C_{sry} + z\frac{\partial^2\omega}{\partial y^2} C_{srx} \right) d_{32}$$

$$+E_3\left[\varepsilon_{33}^p - \left(C_{11}^p d_{31} + C_{12}^p d_{32} \right) d_{31} - \left(C_{21}^p d_{31} + C_{22}^p d_{32} \right) d_{32} \right]$$

$$\therefore D_3 = -t_{pc}\left(\frac{\partial^2\omega}{\partial x^2} C_{11}^p d_{31} + C_{12}^p \left(d_{31}\frac{\partial^2\omega}{\partial y^2} + d_{32}\frac{\partial^2\omega}{\partial x^2} \right) + C_{22}^p d_{32}\frac{\partial^2\omega}{\partial y^2} \right)$$

$$+E_3\left[\varepsilon_{33}^p - \left(C_{11}^p d_{31} + C_{12}^p d_{32} \right) d_{31} - \left(C_{21}^p d_{31} + C_{22}^p d_{32} \right) d_{32} \right] \ldots\ldots\ldots \text{ Eq } 3.28$$

Here, t_{pc} is the distance from the neutral axis to the middle of the piezoelectric layer thickness (ref figure 3.1). In this mathematical model, strain rate damping and viscous damping is considered. $C_{srx}\ and\ C_{sry}$ are the strain rate damping coefficients pertaining to bending of the plate about x axis and y axis, respectively. These damping values vary depending on structural geometry and the piezoelectric layer thickness. Ignoring the damping terms ($C_{srx}\ and\ C_{sry}$) assuming no damping in the feedback loop and also assuming, $d_{31} = d_{32}$, Eq 3.24 turns out to be

$$D_3 = -t_{pc}\left[\left(\frac{\partial^2\omega}{\partial x^2}C_{11}^p + \frac{\partial^2\omega}{\partial y^2}C_{12}^p\right)d_{31} + \left(\frac{\partial^2\omega}{\partial x^2}C_{12}^p + \frac{\partial^2\omega}{\partial y^2}C_{22}^p\right)d_{31}\right]$$

$$+ E_3\left[\varepsilon_{33}^p - \left(C_{11}^p + C_{12}^p\right){d_{31}}^2 - \left(C_{21}^p + C_{22}^p\right){d_{31}}^2\right]$$

$$D_3 = -t_{pc}d_{31}\left[\frac{\partial^2\omega}{\partial x^2}\left(C_{11}^p + C_{12}^p\right) + \frac{\partial^2\omega}{\partial y^2}\left(C_{12}^p + C_{22}^p\right)\right]$$

$$+ E_3\left[\varepsilon_{33}^p - \left(C_{11}^p + C_{12}^p\right){d_{31}}^2 - \left(C_{21}^p + C_{22}^p\right){d_{31}}^2\right]$$

$$D_3 = -t_{pc}d_{31}\left[\frac{\partial^2\omega}{\partial x^2}\left(C_{11}^p + C_{12}^p\right) + \frac{\partial^2\omega}{\partial y^2}\left(C_{12}^p + C_{22}^p\right)\right]$$

$$+ E_3\left[\varepsilon_{33}^p - {d_{31}}^2\left(C_{11}^p + 2C_{12}^p + C_{22}^p\right)\right]$$

Let's assume $C_{11} = C_{22};\ C_{12} = C_{21}$. So,

$$D_3 = -t_{pc}d_{31}\left(C_{11}^p + C_{12}^p\right)\left(\frac{\partial^2\omega}{\partial x^2} + \frac{\partial^2\omega}{\partial y^2}\right) + E_3\left(\varepsilon_{33}^p - 2d_{31}^2\left(C_{11}^p + C_{12}^p\right)\right) \ldots\ldots\ldots \text{Eq 3. 29}$$

Now, from Eq 3.24, we know

$$q(t) = \int_0^a \int_0^b D_3 dxdy$$

$$= \int_0^a \int_0^b -t_{pc}d_{31}\left(C_{11}^p + C_{12}^p\right)\left(\frac{\partial^2\omega}{\partial x^2} + \frac{\partial^2\omega}{\partial y^2}\right)dxdy$$

$$+ \int_0^a \int_0^b E_3\left(\varepsilon_{33}^p - 2d_{31}^2\left(C_{11}^p + C_{12}^p\right)\right)dxdy$$

$$q(t) = -t_{pc}d_{31}\left(C_{11}^p + C_{12}^p\right)\int_{x_i}^{x_{i+1}}\int_{y_i}^{y_{i+1}}\left(\frac{\partial^2\omega}{\partial x^2} + \frac{\partial^2\omega}{\partial y^2}\right)dxdy$$

$$+E_3\left(\varepsilon_{33}^p - 2d_{31}^2\left(C_{11}^p + C_{12}^p\right)\right)A_{pzt} \ldots\ldots\ldots\ldots\ldots\ldots \text{Eq 3.30}$$

Let, $E_3\left(\varepsilon_{33}^p - 2d_{31}^2\left(C_{11}^p + C_{12}^p\right)\right) = \eta_{33}$ which is the permittivity at constant strain. The electric current generated by the piezoelectric material under the dynamic loading can be given by

$$I(t) = \frac{dq(t)}{dt} = -t_{pc}d_{31}\left(C_{11}^p + C_{12}^p\right)\int_{x_i}^{x_{i+1}}\int_{y_i}^{y_{i+1}}\left(\frac{\partial^2}{\partial x^2}\left(\frac{\partial \omega}{\partial t}\right) + \frac{\partial^2}{\partial y^2}\left(\frac{\partial \omega}{\partial t}\right)\right)dxdy + \frac{d}{dt}\frac{v(t)}{t_p}\eta_{33}A_{pzt} \ldots\ldots\ldots\ldots\ldots\ldots\ldots\ldots\ldots\ldots \text{Eq } 3.31$$

Here, Eq 3.31 shows the current flow through the piezoelectric layer. The current expression given by this equation includes the capacitance information of the piezoelectric material in this model that we are studying. $\frac{\eta_{33}A_{pzt}}{t_p}$ is the capacitance of the piezoelectric layer. it is important to include the resistive load into the system equation. So, the differential equation for voltage across the resistive load in feedback loop $v(t) = I(t)R_L$

So, $$I(t) = \frac{v(t)}{R_L} = \frac{dx(t)}{dt} \ldots\ldots\ldots\ldots\ldots\ldots\ldots\ldots\ldots\ldots\ldots\ldots Eq\ 3.32$$

$$\frac{v(t)}{R_L} = \frac{dv(t)}{dt}\frac{\eta_{33}A_{pzt}}{t_p} - t_{pc}d_{31}\left(C_{11}^p + C_{12}^p\right)\int_{x_i}^{x_{i+1}}\int_{y_i}^{y_{i+1}}\left(\frac{\partial^2}{\partial x^2}\left(\frac{\partial \omega}{\partial t}\right) + \frac{\partial^2}{\partial y^2}\left(\frac{\partial \omega}{\partial t}\right)\right)dxdy$$

$$\frac{\eta_{33}A_{pzt}}{t_p}\frac{dv(t)}{dt} - \frac{v(t)}{R_L} = t_{pc}d_{31}\left(C_{11}^p + C_{12}^p\right)$$

$$\int_{x_i}^{x_{i+1}}\int_{y_i}^{y_{i+1}}\left(\frac{\partial^2}{\partial x^2}\left(\frac{\partial \omega}{\partial t}\right) + \frac{\partial^2}{\partial y^2}\left(\frac{\partial \omega}{\partial t}\right)\right)dxdy \ldots\ldots\ldots \text{Eq } 3.33$$

3.1 Solution of the Dynamic Equation

Let us assume that the external loading on the plate is uniform and the maximum amplitude of the loading is q. It is assumed that the plate is simply supported all around and hence the vertical displacement (w) and the moments (M_x and M_y) are zero at the boundary. Here,

$$w = \sum\sum A_{mn} sin\frac{m\pi x}{a} sin\frac{n\pi y}{b}\ T_{mn}(t) \ \ldots\ldots\ldots\ldots\ldots\ldots\ Eq\ 3.34$$

It is possible to assume any suitable eigenfunctions satisfying the boundary conditions pertaining to different boundary conditions. In this model, sinusoidal eigenfunctions are assumed to satisfy the homogeneous boundary conditions.

Let, $sin\frac{m\pi x}{a} = X_m$ and $sin\frac{n\pi y}{b} = Y_n$

$$\frac{\partial^4\omega}{\partial x^4} = \left(\frac{m\pi}{a}\right)^4 \sum\sum A_{mn} X_m(x) Y_n(y)\ T_{mn}(t)$$ ... ... Eq 3. 35

$$\frac{\partial^4\omega}{\partial y^4} = \left(\frac{n\pi}{b}\right)^4 \sum\sum A_{mn} X_m(x) Y_n(y)\ T_{mn}(t)$$ ... ... Eq 3. 36

$$\frac{\partial^4\omega}{\partial x^2\partial y^2} = -\left[\left(\frac{m\pi}{a}\right)^2\left(\frac{n\pi}{b}\right)^2\right]\sum\sum A_{mn} X_m(x) Y_n(y)\ T_{mn}(t)$$ ... ... Eq 3. 37

$$\frac{d^2}{dx^2}\ S_{xy} = \frac{d^2}{dx^2}[H(x-x_i) - H(x-x_{i+1})][H(y-y_i) - H(y-y_{i+1})]$$

$$= [H(y-y_i) - H(y-y_{i+1})]\frac{d}{dx}[\delta(x-x_i) - \delta(x-x_{i+1})]$$ ... ... Eq 3. 38

$$\frac{d^2}{dy^2}\ S_{xy} = \frac{d^2}{dy^2}[H(x-x_i) - H(x-x_{i+1})][H(y-y_i) - H(y-y_{i+1})]$$

$$= [H(x-x_i) - H(x-x_{i+1})]\frac{d}{dy}[\delta(y-y_i) - \delta(y-y_{i+1})]$$ ... ... Eq 3. 39

Now, substituting the values from Eq 3.31 to Eq 3.36 into Eq 3.23 yields

$$\psi_1 \sum\sum \left(\frac{m\pi}{a}\right)^4 A_{mn}X_m(x)Y_n(y)\ T_{mn}(t)$$
$$+ 2\psi_2 \sum\sum \left(\frac{m\pi}{a}\right)^2 + \left(\frac{n\pi}{b}\right)^2 A_{mn}X_m(x)Y_n(y)\ T_{mn}(t)$$
$$+ \psi_3 \sum\sum \left(\frac{m\pi}{a}\right)^4 A_{mn}X_m(x)Y_n(y)\ T_{mn}(t)$$
$$+ \frac{\partial}{\partial t}\left[\varphi_1 \sum\sum \left(\frac{m\pi}{a}\right)^4 A_{mn}X_m(x)Y_n(y)\ T_{mn}(t)\right.$$
$$- \varphi_2 \sum\sum \left(\frac{m\pi}{a}\right)^2 + \left(\frac{n\pi}{b}\right)^2 A_{mn}X_m(x)Y_n(y)\ T_{mn}(t)$$
$$+ C_a \sum\sum A_{mn}X_m(x)Y_n(y)\ T_{mn}(t)$$
$$\left. + \varphi_3 \sum\sum \left(\frac{m\pi}{a}\right)^4 A_{mn}X_m(x)Y_n(y)\ T_{mn}(t)\right]$$
$$+ \frac{V(t)}{t_p}\left(\frac{t_m^2}{2} - \frac{t_p^2}{2}\right)\left[e_{31}\frac{d^2S_{xy}}{dx^2} + e_{32}\frac{d^2S_{xy}}{dx^2} - 2e_{33}\frac{d^2S_{xy}}{dxdy}\right]$$
$$= -q - m\frac{\partial^2}{\partial t^2}\left[\sum\sum A_{mn}X_m(x)Y_n(y)\right] - m\frac{\partial^2}{\partial t^2}(\omega_b)$$
$$-\sum m_r \frac{\partial^2 \omega(\xi_i\eta_i)}{\partial t^2}\ \delta(x-\xi_i)\delta(y-\eta_i) \dots\dots\dots\dots\dots \text{Eq } 3.40$$

Here, $\omega(\xi_i\eta_i) = \sum\sum A_{mn}X_m(\xi_i)Y_n(\eta_i)$ and C_a is the viscous damping coefficient.

Let us divide the eigenfunction and voltage terms for easy assessment. Let,

$$E_1 = \psi_1 \sum\sum \left(\frac{m\pi}{a}\right)^4 A_{mn}X_m(x)Y_n(y)\ T_{mn}(t)$$
$$+ 2\psi_2 \sum\sum \left(\frac{m\pi}{a}\right)^2 + \left(\frac{n\pi}{b}\right)^2 A_{mn}X_m(x)Y_n(y)\ T_{mn}(t)$$
$$+ \psi_3 \sum\sum \left(\frac{m\pi}{a}\right)^4 A_{mn}X_m(x)Y_n(y)\ T_{mn}(t) \dots\dots\dots\dots Eq\ 3.41$$

$$E_2 = \frac{\partial}{\partial t}\Bigg[\varphi_1 \sum\sum \left(\frac{m\pi}{a}\right)^4 A_{mn}X_m(x)Y_n(y)\ T_{mn}(t)$$

$$- \varphi_2 \sum\sum \left(\frac{m\pi}{a}\right)^2 + \left(\frac{n\pi}{b}\right)^2 A_{mn}X_m(x)Y_n(y)\ T_{mn}(t)$$

$$+ C_a \sum\sum A_{mn}X_m(x)Y_n(y)\ T_{mn}(t)$$

$$+ \varphi_3 \sum\sum \left(\frac{m\pi}{a}\right)^4 A_{mn}X_m(x)Y_n(y)\ T_{mn}(t)\Bigg] \ldots\ldots\ldots\ldots\ Eq\ 3.42$$

$$E_3 = \frac{V(t)}{t_p}\left(\frac{t_m^2}{2} - \frac{t_p^2}{2}\right)\left[e_{31}\frac{d^2S_{xy}}{dx^2} + e_{32}\frac{d^2S_{xy}}{dx^2} - 2e_{33}\frac{d^2S_{xy}}{dxdy}\right] \ldots\ldots\ldots\ldots\ Eq\ 3.43$$

$$F = -q - m\frac{\partial^2}{\partial t^2}\left[\sum\sum A_{mn}X_m(x)Y_n(y)\right] - m\frac{\partial^2}{\partial t^2}(\omega_b)$$

$$- \sum m_r \frac{\partial^2 \omega(\xi_i\eta_i)}{\partial t^2}\ \delta(x-\xi_i)\delta(y-\eta_i) \ldots\ldots\ldots\ldots\ \text{Eq } 3.44$$

Solving the equations, we get

E_1 output:

$$\psi_1 \frac{ab}{4}\left(\frac{\pi r}{a}\right)^4 A_{rs}T_{rs}(t) + 2\psi_2 \frac{ab}{4}\left[\left(\frac{\pi r}{a}\right)^2 + \left(\frac{\pi s}{b}\right)^2\right]A_{rs}T_{rs}(t) + \psi_3 \frac{ab}{4}\left(\frac{\pi s}{b}\right)^4 A_{rs}T_{rs}(t)$$

$$= \left[\psi_1\left(\frac{\pi r}{a}\right)^4 + 2\psi_2\left[\left(\frac{\pi r}{a}\right)^2 + \left(\frac{\pi s}{b}\right)^2\right] + \psi_3\left(\frac{\pi s}{b}\right)^4\right]\frac{ab}{4}A_{rs}T_{rs}(t) \ldots\ldots\ldots\ldots\ldots\ldots\ Eq\ 3.45$$

Let, $\left[\psi_1 \frac{ab}{4}\left(\frac{\pi r}{a}\right)^4 + 2\psi_2 \frac{ab}{4}\left[\left(\frac{\pi r}{a}\right)^2 + \left(\frac{\pi s}{b}\right)^2\right] + \psi_3 \frac{ab}{4}\left(\frac{\pi s}{b}\right)^4\right]\frac{ab}{4} = K_{rs}$

And $A_{rs}T_{rs}(t) = \underline{T_{rs}}(t)$. Hence, the A_{rs} coefficients are consumed in the expression $T_{rs}(t)$ terms.

E_2 output:

$$\frac{d}{dt}\left[\varphi_1\frac{ab}{4}\left(\frac{\pi r}{a}\right)^4 A_{rs}T_{rs}(t) - \varphi_2\frac{ab}{4}\left[\left(\frac{\pi r}{a}\right)^2+\left(\frac{\pi s}{b}\right)^2\right]\right]A_{rs}T_{rs}(t) + \varphi_3\frac{ab}{4}\left(\frac{\pi s}{b}\right)^4 A_{rs}T_{rs}(t)$$

$$= \left[\varphi_1\left(\frac{\pi r}{a}\right)^4 - \varphi_2\left[\left(\frac{\pi r}{a}\right)^2+\left(\frac{\pi s}{b}\right)^2\right] + \varphi_3\left(\frac{\pi s}{b}\right)^4 + C_a\right]\frac{ab}{4}A_{rs}\dot{T}_{rs}(t) \ldots\ldots\ldots\ldots\ldots \textit{Eq 3. 46}$$

From =$\varphi 1\pi ra4 - \varphi 2\pi ra2 + \pi sb2 + \varphi_3\left(\frac{\pi s}{b}\right)^4 + C_a$ $\frac{ab}{4}A_{rs}\dot{T}_{rs}(t)$ ... ... Eq 3. 46, let,

$$\left[\varphi_1\left(\frac{\pi r}{a}\right)^4 - \varphi_2\left[\left(\frac{\pi r}{a}\right)^2+\left(\frac{\pi s}{b}\right)^2\right] + \varphi_3\left(\frac{\pi s}{b}\right)^4 + C_a\right]\frac{ab}{4} = C_{rs}$$

And $A_{rs}\dot{T}_{rs}(t) = \underline{\dot{T}_{rs}}(t)$. Hence, the A_{rs} coefficients are consumed in the expression $\dot{T}_{rs}(t)$ terms. E_3 output from $E3=V(t)t_p\left(\frac{t_m^2}{2}-\frac{t_p^2}{2}\right)\left[e_{31}\frac{d^2S_{xy}}{dx^2}+e_{32}\frac{d^2S_{xy}}{dx^2}-2e_{33}\frac{d^2S_{xy}}{dxdy}\right]$ ... ... $Eq\ 3.43$ can be divided into three parts. So,

E_3^1 output

Let,

$$\frac{V(t)}{t_p}\left(\frac{t_m^2}{2}-\frac{t_p^2}{2}\right)e_{31} = V_{31}v(t) \ldots\ldots\ldots\ldots\ldots\ldots\ldots\ldots\ldots\ldots\ldots\ldots\ldots\ldots\ldots\ldots\ldots\ldots\ldots\ldots \textit{Eq 3. 47}$$

$$\frac{V(t)}{t_p}\left(\frac{t_m^2}{2}-\frac{t_p^2}{2}\right)e_{32} = V_{32}v(t) \ldots\ldots\ldots\ldots\ldots\ldots\ldots\ldots\ldots\ldots\ldots\ldots\ldots\ldots\ldots\ldots\ldots\ldots\ldots\ldots \textit{Eq 3. 48}$$

$$\frac{V(t)}{t_p}\left(\frac{t_m^2}{2}-\frac{t_p^2}{2}\right)e_{33} = V_{33}v(t) \ldots\ldots\ldots\ldots\ldots\ldots\ldots\ldots\ldots\ldots\ldots\ldots\ldots\ldots\ldots\ldots\ldots\ldots\ldots\ldots \textit{Eq 3. 49}$$

$$\int_0^a\int_0^b \frac{d^2}{dx^2}[H(x-x_i)-H(x-x_{i+1})][H(y-y_i)-H(y-y_{i+1})]$$

$$= \int_0^a \int_0^b \frac{d^2H(x)}{dx^2} sin\frac{r\pi x}{a} H(y) sin\frac{s\pi y}{b} dxdy$$

$$= \int_0^b \left[\int_0^a \frac{d^2H(x)}{dx^2} sin\frac{r\pi x}{a} dx\right] H(y) sin\frac{s\pi y}{b} dy$$

$$= \int_0^b \left[\int_0^a \frac{df(x)}{dx} sin\frac{r\pi x}{a} dx\right] H(y) sin\frac{s\pi y}{b} dy$$

Applying integral by parts

$$\int f'g dx = \int_0^a \delta'^{(x)} sin\frac{r\pi x}{a} dx = \left[\delta(x) sin\frac{r\pi x}{a}\right] - \int_0^a \delta(x) cos\frac{r\pi x}{a} dx$$

$$\delta(x) = \delta(x - x_i) - \delta(x - x_{i+1}) + \delta\left(x - x_j\right) - \delta\left(x - x_{j+1}\right)$$

$$\int_0^a \delta(x) cos\frac{r\pi x}{a} dx = \frac{r\pi}{a}\left[-cos\frac{r\pi x_i}{a} + cos\frac{r\pi x_{i+1}}{a} - cos\frac{r\pi x_j}{a} + cos\frac{r\pi x_{j+1}}{a}\right] = cosV_x$$

$$\frac{r\pi}{a}\int_0^b cosV_x\, H(y) sin\frac{s\pi y}{b} dy$$

$$\frac{rb\pi}{as\pi} cosV_x \int_0^b H(y) d\left(cos\frac{s\pi y}{b}\right)$$

$$sin\frac{r\pi x}{a} sin\frac{s\pi y}{b}\, dxdy$$

$$= \frac{rb}{sa} cosV_x \left[H(y) cos\frac{s\pi y}{b} | - \int_0^b \delta(y) \cos\frac{s\pi y}{b}\right]$$

$$= \frac{rb}{sa} cosV_x \left[-cos\frac{s\pi y_i}{b} + cos\frac{s\pi y_{i+1}}{b} - cos\frac{s\pi y_j}{b} + cos\frac{s\pi y_{j+1}}{b}\right]$$

$\therefore sin\frac{r\pi x}{a} sin\frac{s\pi y}{b}\, dxdy = \frac{rb}{sa} cosV_x\, cosV_y$ ... ... *Eq 3. 50*

E_3^2 becomes

$$\int_0^a \int_0^b \frac{d^2}{dy^2}[H(y)] sin\frac{s\pi y}{b}\ H(x) sin\frac{r\pi x}{a} dxdy$$

$\int_0^a \left[\int_0^b \delta'(y) sin\frac{s\pi y}{b} dy\right]\ H(x) sin\frac{r\pi x}{a} dx = \frac{sa}{rb} cosV_x\ cosV_y$ ... ... *Eq 3. 51*

Similarly, E_3^3 becomes

$$\int_0^a \int_0^b \frac{d^2}{dxdy} H(y)H(x) sin\frac{r\pi x}{a} sin\frac{s\pi y}{b}\ dxdy$$

$$\int_0^a \int_0^b \delta'(y)\delta'(x) sin\frac{r\pi x}{a} sin\frac{s\pi y}{b}\ dxdy$$

$\int_0^a \left[\int_0^b \delta'(x) sin\frac{r\pi x}{a} dx\right] \delta'(y) sin\frac{s\pi y}{b} dy = \frac{rs\pi^2}{ab} cosV_x\ cosV_y$ ... ... *Eq 3. 52*

Now adding the equations, total E_3^3 output turns out

$$V(t)\left[v_{31}\frac{rb}{sa} cosV_x\ cosV_y + v_{32}\frac{rb}{sa} cosV_x\ cosV_y - 2v_{33}\frac{rs\pi^2}{ab} cosV_x\ cosV_y\right]$$

$$= V(t) cosV_x\ cosV_y \left[v_{31}\frac{rb}{sa} + v_{32}\frac{rb}{sa} - 2v_{33}\frac{rs\pi^2}{ab}\right] \text{... ... ... } Eq\ 3.53$$

Let, $cosV_x\ cosV_y \left[v_{31}\frac{rb}{sa} + v_{32}\frac{rb}{sa} - 2v_{33}\frac{rs\pi^2}{ab}\right] = \lambda_{rs}$

Now, combining E_3^1, E_3^2 and E_3^3

$$\frac{ab}{4} K_{rs}\underline{T_{rs}}(t) + \frac{ab}{4} C_{rs}\frac{d\underline{T_{rs}}(t)}{dt} + \lambda_{rs} V(t) = F$$

Similarly, the force can be divided into three parts. The external force attributable to varying pressure throughout the membrane is expressed as

$$F_1 = \int_0^a \int_0^b q \, sin\frac{r\pi x}{a} sin\frac{s\pi y}{b} \, dxdy \ldots\ldots\ldots\ldots\ldots\ldots\ldots\ldots Eq\ 3.54$$

If pure vertical translation is assumed, the excitation force attributable to mass inertia can be written as

$$F_2 = -m\frac{\partial^2}{\partial t^2}\left[\frac{ab}{4} A_{rs} T_{rs}(t)\right] - m\frac{\partial^2}{\partial t^2}(\omega_b)$$

$$Here, \omega_b = \omega_b e^{i\omega t}$$

$$= -m\frac{ab}{4}\frac{d^2\underline{T_{rs}}(t)}{dt^2} - m\,\omega_b(i\omega)^2 e^{i\omega t}$$

$$= -m\frac{ab}{4}\frac{d^2\underline{T_{rs}}(t)}{dt^2} - m\,\omega_b\omega^2 e^{i\omega t} \ldots\ldots\ldots\ldots\ldots\ldots\ldots Eq3.55$$

and, the force generated due to the mass of the resonators on top of the plate or membrane is

$$F_3 = -\sum_{r=1}^{N} m_r \frac{\partial^2}{\partial t^2} \int_0^a \int_0^b \left[\sum\sum A_{mn} \, sin\frac{\pi m\xi_i}{a} \sin\frac{\pi n\eta_i}{b} \right.$$
$$\left. \delta(x-\xi_i)\delta(y-\eta_i) sin\frac{r\pi x}{a} sin\frac{s\pi y}{b}\right] dxdy + \sum_{r=1}^{N} m_r \frac{d^2\omega_b}{dt^2}$$

$$= -\sum_{r=1}^{N} m_r \frac{\partial^2}{\partial t^2} \left[\left[\sum\sum A_{mn} \, sin\frac{\pi m\xi_i}{a} \sin\frac{\pi n\eta_i}{b} \, \delta(x-\xi_i)\delta(y-\eta_i) sin\frac{r\pi x}{a} sin\frac{s\pi y}{b}\right] dxdy\right]$$
$$+ \sum_{r=1}^{N} m_r \frac{d^2\omega_b}{dt^2}$$

$$= -\sum_{r=1}^{N} m_r \frac{\partial^2}{\partial t^2} \frac{d^2\underline{T_{rs}}(t)}{dt^2} \, sin^2\frac{\pi m\xi_i}{a} \, sin^2 \frac{\pi n\eta_i}{b} + \sum_{r=1}^{N} m_r\omega_b\omega^2 \ldots\ldots\ldots Eq\ 3.56$$

Now,

$$\frac{dT_{rs}}{dt} = \frac{-i\omega\left[I\omega_b - \frac{4}{ab}\lambda_{rs}V_0\right]e^{i\omega t}}{M_{rs}[-\omega^2 + 2i\xi_{rs}\omega_{rs}\omega + \omega_{rs}^2]} \ldots\ldots\ldots\ldots \; Eq\ 3.57$$

Let, $M_{rs}[-\omega^2 + 2i\xi_{rs}\omega_{rs}\omega + \omega_{rs}^2] = D_{rs}$

From Eq 3.30, the coupling equation of voltage becomes:

$$\left(\frac{\eta_{33}A_p}{t_p}\right)\frac{dv(t)}{dt} - \frac{v(t)}{R_L} = t_{pc}d_{31}\left(C_{11}^p + C_{12}^p\right)\int_{x_i}^{x_{i+1}}\int_{y_i}^{y_{i+1}}\left(\frac{\partial^2}{\partial x^2}\left(\frac{\partial\omega}{\partial t}\right)\right)dxdy$$

$$\omega = \sum\sum sin\frac{m\pi x}{a}sin\frac{n\pi y}{b}\ T_{mn}(t)$$

Here, A_{mn} is consumed in $T_{mn}(t)$

$$\frac{\partial\omega}{\partial t} = \sum\sum sin\frac{m\pi x}{a}sin\frac{n\pi y}{b}\ \frac{dT_{mn}(t)}{dt}$$

$$\frac{\partial^2}{\partial x^2}\left(\frac{\partial\omega}{\partial t}\right) = -\sum\sum A_{mn}\left(\frac{m\pi}{a}\right)^2 sin\frac{m\pi x}{a}sin\frac{n\pi y}{b}\ \frac{dT_{mn}(t)}{dt} \ldots\ldots\ldots\ldots\ldots\ldots\ldots\ldots\text{Eq 3. 58}$$

$$\frac{\partial^2}{\partial y^2}\left(\frac{\partial\omega}{\partial t}\right) = -\sum\sum A_{mn}\left(\frac{n\pi}{b}\right)^2 sin\frac{m\pi x}{a}sin\frac{n\pi y}{b}\ \dot{T_{mn}} \ldots\ldots\ldots\ldots\ldots\ldots\ldots\ldots\ldots\ldots\text{Eq 3. 59}$$

Using Eq 3.55

$$\frac{\partial^2}{\partial x^2}\left(\frac{\partial\omega}{\partial t}\right) = -\sum\sum A_{mn}\left(\frac{m\pi}{a}\right)^2\left[\int_{x_i}^{x_{i+1}}\int_{y_i}^{y_{i+1}} sin\frac{m\pi x}{a}sin\frac{n\pi y}{b}\ dxdy\right]\dot{T_{mn}}$$

$$= -\sum\sum A_{mn}\frac{mb}{an}[cosX_m]\,[cosY_n]\dot{T_{mn}} \ldots\ldots\ldots\ldots\ldots \; Eq\ 3.60$$

Similarly, from Eq 3.56

$$\frac{\partial^2}{\partial y^2}\left(\frac{\partial \omega}{\partial t}\right) = -\sum\sum A_{mn}\frac{an}{mb}[cosX_m]\,[cosY_n]\dot{T_{mn}} \ldots\ldots\ldots\ldots\ldots\ldots\ldots\ Eq\ 3.61$$

Substituting the values in Eq 3.33 we get

$$\left(\frac{\eta_{33}A_p}{t_p}\right)\frac{dv(t)}{dt} - \frac{v(t)}{R_L} = -t_{pc}d_{31}\left(C_{11}^p + C_{12}^p\right)\sum\sum[cosX_m]\,[cosY_n]\left(\frac{mb}{an}+\frac{an}{mb}\right)\frac{dT_{mn}(t)}{dt} \ldots\ldots\ldots\ldots\ldots\ldots\ldots\ldots \text{ Eq } 3.62$$

Using homogeneous solution and particular integral, Eq 3.62 can be used to find the solution for the voltage across resistive load.

3.2 Solution under Harmonic Condition

Now, assuming harmonic vibration being applied on the structure

$$v(t) = v_0 e^{i\omega t}$$

$$\frac{dv(t)}{dt} = v_0 i\omega e^{i\omega t} \ldots\ldots\ldots\ldots\ldots\ldots\ Eq\ 3.63$$

Here, v_0 is the maximum voltage across the load resistance R_L. The voltage output from the energy harvester will also be harmonic assuming that the proposed system is linear. Substituting the values in Eq 3.63 we get,

$$v_0\left[i\omega\left(\frac{\eta_{33}A_p}{t_p}\right) - \frac{1}{R_L}\right]e^{i\omega t} = -t_{pc}d_{31}\left(C_{11}^p + C_{12}^p\right)\sum\sum[cosX_m]\,[cosY_n]\frac{ab}{mn\pi^2}\left[\left(\frac{\pi m}{a}\right)^2 + \left(\frac{\pi n}{b}\right)^2\right]\dot{T_{mn}}(t) \ldots\ldots\ldots\ldots\ldots\ldots \text{ Eq } 3.64$$

Here, $[cosX_m][cosY_n]\ \frac{ab}{mn\pi^2}\left[\left(\frac{\pi m}{a}\right)^2 + \left(\frac{\pi n}{b}\right)^2\right] = K_{mn}$

For Square/rectangular plate with resonator

$$\left[m + \frac{4}{ab}\sum m_r sin^2\frac{\pi r\xi_i}{a}\ sin^2\frac{\pi s\eta_i}{b}\right]\frac{d^2T_{rs}}{dt^2} + C_{rs}\frac{dT_{rs}}{dt} + K_{rs}T_{rs}(t)$$

$$= -\frac{4}{ab}\lambda_{rs}v_0 e^{i\omega t} - \int_0^a\int_0^b q\ \ sin\frac{r\pi x}{a}sin\frac{s\pi y}{b}\ dxdy + m\omega_b\omega^2 e^{i\omega t}$$

$$+ \sum m_r\ \omega_b\omega^2 e^{i\omega t} - C_a(i\omega)\omega_b e^{i\omega t}$$

$$M_{rs}\frac{d^2T_{rs}(t)}{dt^2} + C_{rs}\frac{T_{rs}(t)}{dt} + K_{rs}T_{rs}(t) = -\left[\left[\frac{4}{ab}\lambda_{rs}v_0 + C_a(i\omega)\omega_b\right] + \left[m\omega_b\omega^2 + \sum m_r\ \omega_b\omega^2\right]\right]e^{i\omega t} \ldots\ldots\ldots\ldots\ldots\ldots\ldots\ldots \text{Eq } 3.65$$

In this equation ω is any excitation frequency and ω_b is the displacement amplitude of the transverse vibration. Where C_{rs} is the combination of both viscous and strain rate damping. Assume, $I = [(m + \sum m_r)\omega^2 - C_a(i\omega)]$

$$M_{rs}\frac{d^2T_{rs}(t)}{dt^2} + C_{rs}\frac{T_{rs}(t)}{dt} + K_{rs}T_{rs}(t) = \left[I\omega_b - \frac{4}{ab}\lambda_{rs}v_0\right]e^{i\omega t} \ldots\ldots\ldots\ Eq\ 3.66$$

Here, damping of the system $\xi_{rs} = \frac{C_{rs}}{2[m_{rs}]\omega_{rs}}$ and

natural frequency of the system $\omega_{rs} = \sqrt{\frac{K_{rs}}{M_{rs}}}$

Solving Eq 3.62 assuming no vertical load we get the steady state solution,

$$T_{rs}(t) = \frac{\left[I\omega_b - \frac{4}{ab}\lambda_{rs}\ v_0\right]e^{i\omega t}}{M_{rs}[-\omega^2 + 2i\xi_{rs}\omega_{rs}\omega + \omega_{rs}^2]} \ldots\ldots\ldots\ldots\ldots\ldots\ldots\ldots\ Eq\ 3.67$$

From $v0i\omega\eta 33Aptp{-}1RLei\omega t = -t_{pc}d_{31}\left(C_{11}^{p}+C_{12}^{p}\right)\sum\sum[cosX_m]\,[cosY_n]$, we finally get

$$V_0\left[i\omega\left(\frac{\eta_{33}A_p}{t_p}\right)-\frac{1}{R_L}\right]e^{i\omega t}=CP\sum\sum K_{mn}\frac{i\omega I\omega_b}{D_{mn}}-CP\sum\sum K_{mn}\frac{4}{ab}\frac{\lambda_{mn}}{D_{mn}}v_0e^{i\omega t}$$

$$V_0\left[i\omega\left(\frac{\eta_{33}A_p}{t_p}\right)-\frac{1}{R_L}+CP\sum\sum K_{mn}\frac{4}{ab}\frac{\lambda_{mn}}{D_{mn}}\right] = CP\sum\sum K_{mn}\frac{i\omega I\omega_b}{D_{mn}} \ldots\ldots\ldots\ldots\ldots\ldots\ldots\ Eq\ 3.68$$

Now, the maximum voltage output across the load resistance will also depend on the external load applied on the structure. Using Eq 3.68 the maximum voltage output turns out to be

$$V_0=\frac{CP\sum\sum K_{mn}\frac{i\omega I\omega_b}{D_{mn}}}{\left[i\omega\left(\frac{\eta_{33}A_p}{t_p}\right)-\frac{1}{R_L}+CP\sum\sum K_{mn}\frac{4}{ab}\frac{\lambda_{mn}}{D_{mn}}\right]} \ldots\ldots\ldots\ldots\ldots Eq\ 3.69$$

and thus, the maximum power output will be $P=\frac{V_0^2}{R_L}$

3.3. Numerical Implementations

A MATLAB 2021 code is developed based on the equations derived in the "Solution under Harmonic Condition" section. The resistance (load) was varied to calculate the power output variation at different frequencies. From this study, resonant frequencies were identified at different load resistances. Material properties for this analysis are used (Aluminum, PZT-5H,Silicone membrane and PVDF) as follows in table 3.1: To calculate the voltage output, nine different external load resistances have been used. As stated earlier, in this study, two types of damping (1) Strain Rate Damping (SRD) and(2) viscous damping are considered. In the equations stated earlier in this chapter, C_{srx} and C_{sry}

represent the SRD coefficients related to the bending of the plate about the x- and y-axes, respectively, and C_a is the viscous damping coefficient.

Table 3.1: Material properties of the elements used in this study

Material	**Young's Modulus (Pa)**	d_{31}**(C/N)**	ε_{33}**(F/m)**	**Poisson's ratio**
Aluminum	68e09	-	-	0.3
PZT-5H	62e09	220e-11	3400	0.35
Silicone membrane	8.89e06	-	-	0.48
PVDF	5.7e09	70e-11	12	0.35

Figure. 3.3 shows the frequency response function of a 30mmX30mm aluminum substrate with a piezoelectric PZT-5H layer on top. The MATLAB model was executed for a load resistance ranging from 100Ω to 20kΩ in the frequency range between 0 to 20kHz. From the plot it can be seen that the resonance frequency peaks initiate at comparatively higher frequencies, specifically after 2KHz.

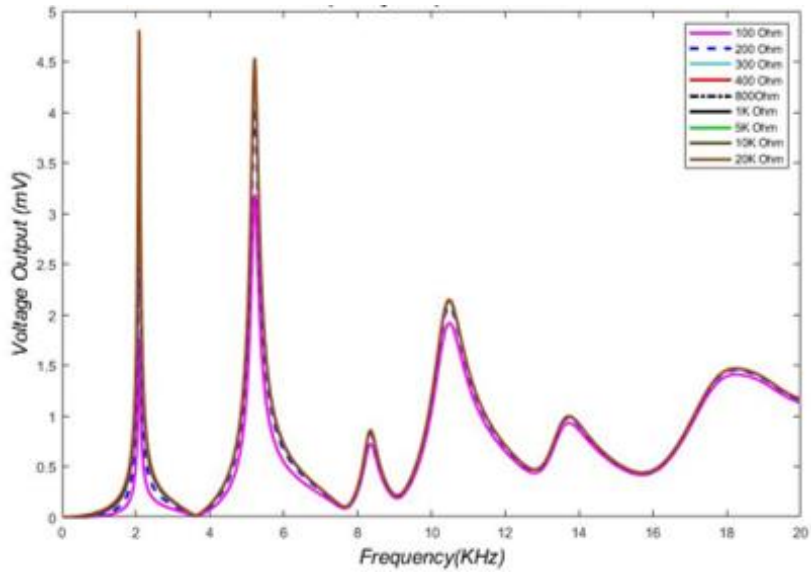

Figure 3. 3: FRF function of a 30mm X30mm square aluminum plate with PZT-5H on top exposed to varying load resistances

Next, same experiment was conducted on a more flexible silicone membrane of the same dimension and load resistance range. Here too the resonance frequencies were initiated at a higher frequency. The output can be seen from figure 3.4.

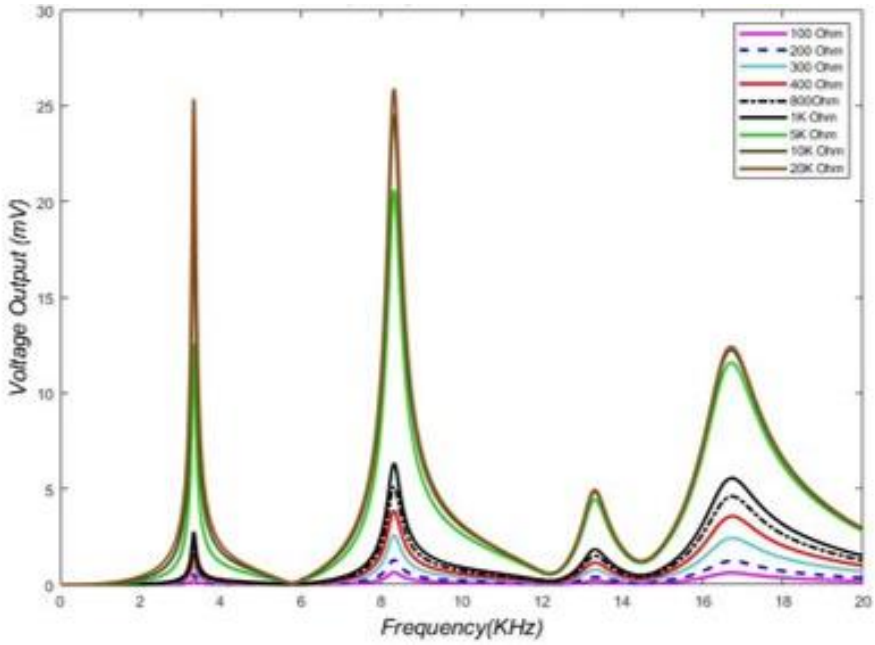

Figure 3. 4: FRF function of a 30mm X30mm square silicone membrane with PVDF on top exposed to varying load resistances

Since the initial resonance frequency range is a bit high, compared to our desired frequency range which is around 1kHz so the dimensions were modified and found that a 20mmX20mm square silicone membrane with flexible piezoelectric PVDF layer demonstrates promising output in our desired frequency range. Figure 3.5 demonstrates the output from this model. The FRF ($\frac{V}{\omega^2}$as function of ω^2) was also obtained for the silicone membrane sample model. Though only a certain frequency range is considered here, but multiple resonance frequency peaks can be observed within 3kHz range. So, if requires, these models can also be used to harvest energy from higher frequencies also. This can also

play a very important role in multi-frequency energy harvesting including both high and low frequencies.

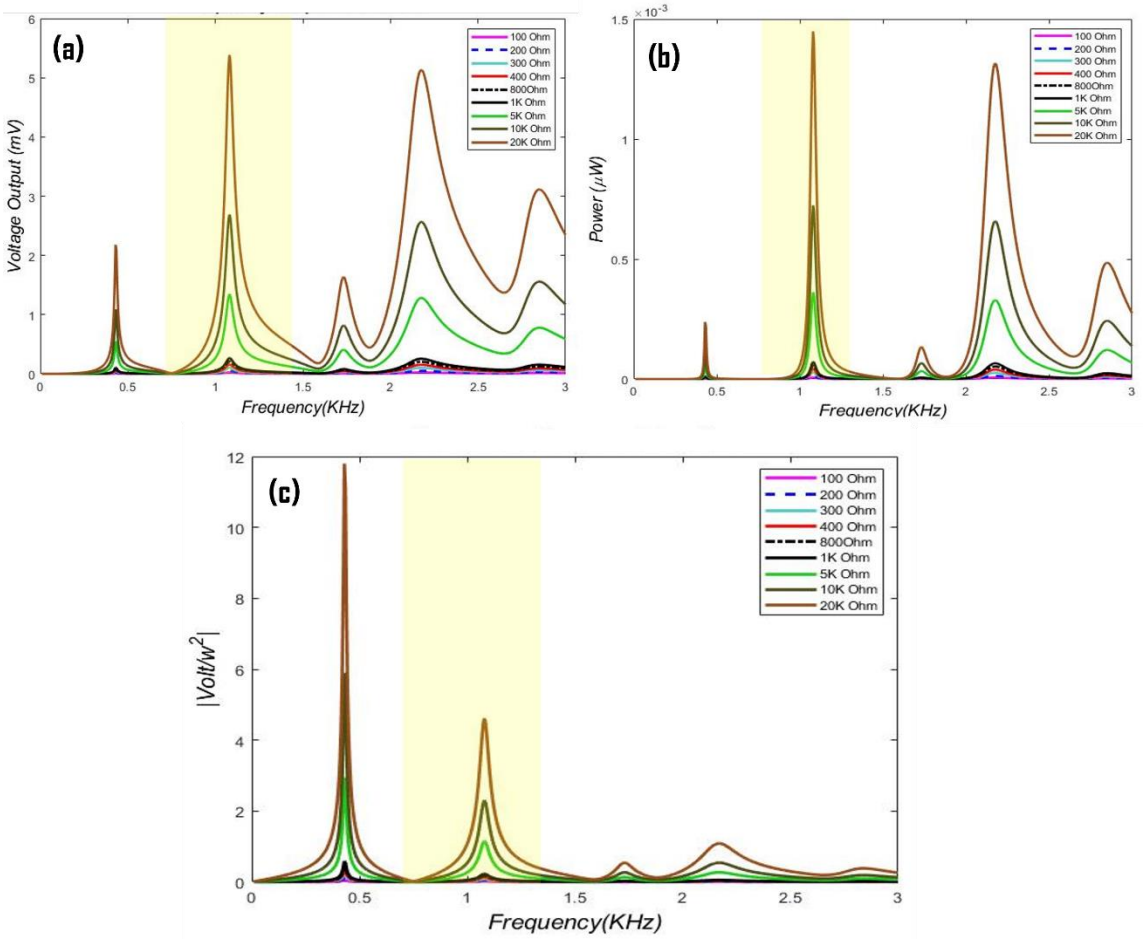

Figure 3. 5 : FRF function of a 20mm X20mm square silicone membrane with PVDF on top exposed to varying load resistances (a) voltage output; (b) power output (c) FRF.

In the end, a numerical model was developed in COMSOL Multiphysics using the 20mmX20mm square model keeping all the dimensions similar. The analytical and numerical models were compared to determine if the resonance frequency matches for both numerical and analytical study. From figure 3.6 it can be seen that the resonance frequency from both studies dwells in a comparatively similar range. So, we can conclude that this

model works for low frequency energy harvesting using thin membrane and also flexible piezoelectric material.

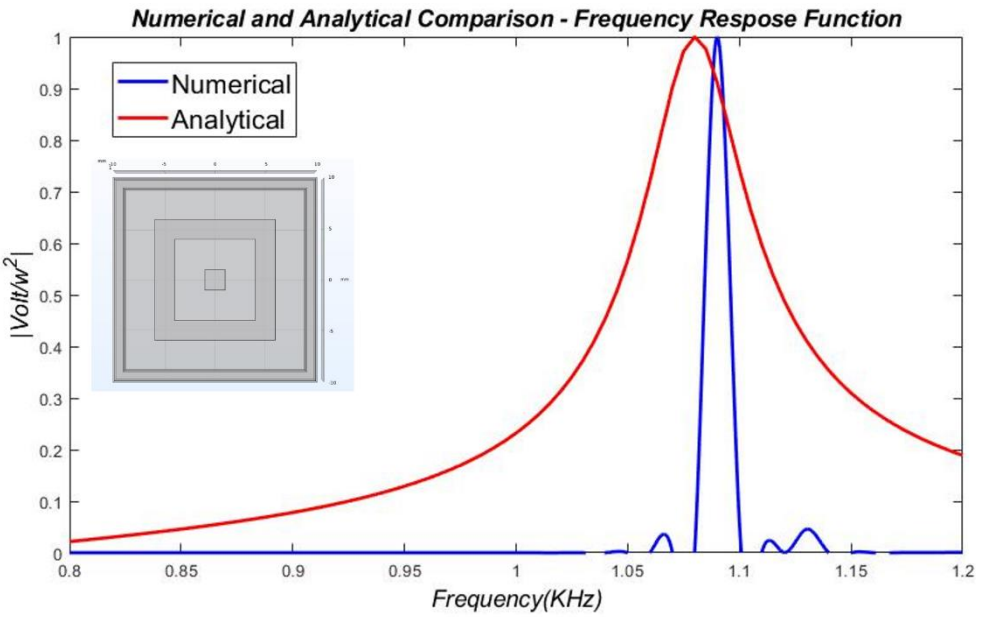

Figure 3. 6: Qualitative comparison between analytical and numerical results of the FRF function of a 20mm x 20mm square membrane with piezoelectric PVDF patch

In this chapter, a mathematical derivation of output voltage and power expressions are presented for plate type energy harvesters. The frequency response function produces peak values at certain band of frequencies. The analytical model can be used to modify and verify the model to find out the optimum dimensions and criteria for an effective harvester. The resonant band structures observed from the initial study suggests that they depend on load resistance. Thus, based on the target power output and applicable load resistances an effective energy harvester can be designed with a wider band of resonance frequency.

CHAPTER 4

Acoustoelastic Metamaterial with Simultaneous Noise Filtering and Energy Harvesting Capability from Ambient Vibrations

Recent advancements in low power electronic gadgets, micro-electromechanical systems and wireless sensors have significantly increased the local power demand. To circumvent the energy demand, low power local energy harvesters are proposed for harvesting energy from different ambient energy sources. Energy harvesters utilize the the ability of piezoelectric materials to generate an electric potential in response to external mechanical deformation. Significant research activities on low power energy harvesters can be found in many works of literature. The key to these research activities is to introduce self-powered wireless electronics systems such that the maintenance, replacement of the old batteries, and the chemical waste from conventional batteries could be avoided.

4.1 Noise Reduction using Metamaterial

These days, with the development of a transportation system, and a tremendous increase in the traffic density, noise problem has drawn more attention in recent years. The impact of urban noise on the quality of life has become an important index to make both urban and environmental policy throughout the world [122]. Hence, different measures have been taken to minimize roadside noises. Noise barriers are being used beside the roads to minimize the intensity of the generated noise. Researches have shown in certain noise barriers that

under carefully controlled measurement conditions, the noise pattern changes with the panel types being absorptive to reflective[123]. Some studies have also shown that some noise barriers create annoying sounds compared to areas without noise barriers which lead to low annoyance-reduction efficiency [124]. In most of the cases, the incident waves get reflected from the noise barriers. The collision of these reflected waves with the incident waves creates such an annoying sound. The problem is so acute that people have started thinking about alternative ways to create noise barriers. Some passive barriers (such as Median noise barriers), can be employed to reduce the impact of traffic noise on roadside communities via the direct propagation path[125]. To introduce passive barriers, two different absorbent materials including a fibrous material and a grass surface are similarly being applied. Results from the use of these passive noise barriers show that thin absorptive barriers are equivalent at lower frequencies but perform better at mid to high frequencies compared to the rigid noise barriers[126]. However, when the barriers are placed in parallel and on opposite sides of a sound source, their performance deteriorates remarkably. Another study has shown that the addition of the perforated sheet inside the wall improves the performance of the barriers [127].

Acousto-Elastic Sonic Crystals (AESC) possess unique properties that are not easily demonstrated by naturally occurring materials, such as, negative bulk modulus, negative mass density[128] AESC's are traditionally designed for guiding and filtering acoustic waves using the Bragg Scattering and Local Resonance phenomena [129]. These sound-absorbing materials as noise barriers are not only required for the industrial purpose but also required for the building and residence applications. Components of usual building materials such as bricks or concrete are certified with required strength, specifically

depending on their application. Moreover, the beauty-enhancing sound-absorbing materials are also used on building materials to make the buildings sound resistant. Thus, if the conventional building materials can be replaced by the sound-absorbing acousto-elastic metamaterials (AEMM), the efficiency of the sound isolation process can be improved. On top of the capability of isolating sound, if the acousto-elastic metamaterials are used for building the structures, the prospect of harvesting energy from a building material will open a way to produce energy from the unused ambient energies. Hence, in this work, a proposal is made to create a acousto-elastic MetaWall brick as a building material that will not only absorb the ambient noise but also harvest the trapped noise to convert it to the electrical power. To meet these functions, the multi-functional MetaWall noise barriers are proposed to construct with Acousto-Elastic metamaterials (AEMM). AEMM is a kind of metamaterial, which is traditionally used for guiding and manipulating elastic waves. Based on the spectrum analysis of traffic at a different location it was shown[130] that the sound pressure decreases with increasing frequency especially above 1 KHz. Also, it was found[130, 131] that the 200 Hz – 500 Hz is the most frequently occurring frequency in the roadside noises where sound pressure is significant enough to cause harm to the human ear and may cause psychological trauma and other health diseases. Researchers designed many roadside sound barriers specifically to filter those low frequencies. Hence, in this article, the study is focused on the frequency range below 500 Hz (between ~420 - ~480 Hz) to filter the noise and harvest the energy from that specified range of frequency.

4.2 Energy Harvesting with Metamaterial

While traditional noise walls filter acoustic energy, these abounded filtered energy remains unused. Since the AEMM possess the capability to trap the filtered energy, it delivers the opportunity to recover these energies into a usable form. The review on energy harvester research shows that microcantilever energy harvesters are the most common low power energy harvesters so far. For this kind of energy harvesters, the range of power outputs is in micro Watts[132-135]. Most of the energy harvester uses the local resonance physics to harvest dynamic energy. Acoustoelastic metamaterial (AEMM) can introduce local resonance in the structure. Recently AEMM's are introduced in the field of energy harvesting because of its unique ability in wave manipulation in a wide range of frequency[135-139]. It is established that sonic crystals have the ability to create frequency band gaps either through Bragg scattering or local resonance [140-142]. Hence several researchers proposed AEMM's for performing duel operations, filtering sound and harvesting trapped energy, simultaneously. This goal cannot be achieved using the usual energy harvesters available.

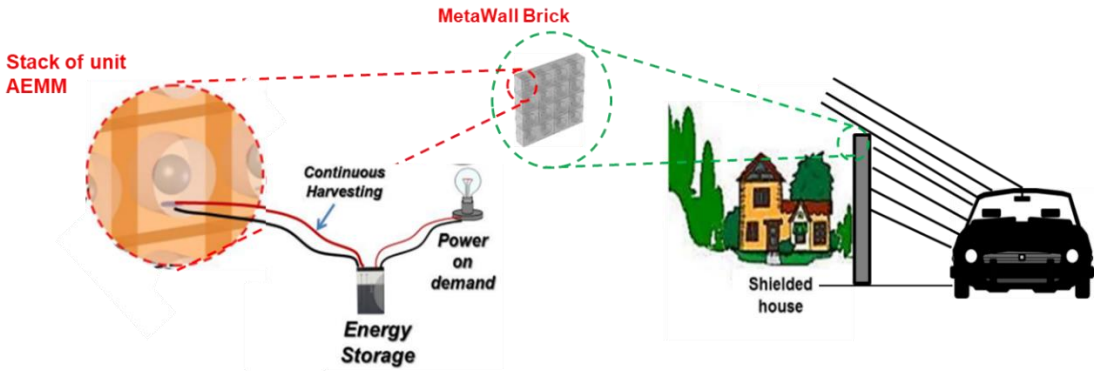

Figure 4. 1: Schematic diagram of simultaneous noise control and energy harvesting using AEMM

The possibility of simultaneous wave filtering and energy harvesting was first mentioned by Gonella et al. [136] in 2009. Earlier, it has been proposed that [60, 67, 143-146] if the filtered wave energy at the stopband frequencies is trapped inside the soft constituent of the metamaterial as dynamic strain energy, then it must be possible to recover that same energy using embedded piezoelectric wafers. Hence, coupling two different physics in a single phenomenon the bimodal AEMM is proposed. Maximum power can be harvested while the piezoelectric wafer is strained inside the matrix due to the local resonance of the embedded mass[143]. Earlier researchers have done various investigations on metamaterials that work in a dual-mode where noise filtering and energy harvesting are done simultaneously. Ahmed et. al [67] have shown that at frequencies lower than ~3KHz can be trapped inside AEMM cell. The trapped energy can also be harvested using proper piezoelectric materials. However, the maximum power output from this model was in the µW range.

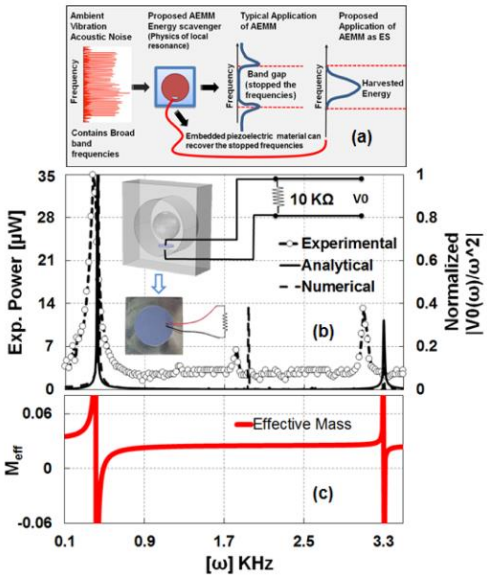

Figure 4. 2: Model representation and power output from the model used by Ahmed et.al

Since Acousto-elastic metamaterial (AEMM) possesses similar physics as AESC and AEMM can be an ideal choice to harvest energy from the filtered wave energy. Till now energy harvesting capabilities of AEMM haven't been explored extensively. In an ideal world, AEMM's are represented as a spring-mass combination in a mass-in-mass system. In this thesis, similar AEMM's are studied to develop low-frequency energy harvester. Very few attempts have been made so far to model the energy harvester based on Acousto-elastic metamaterials.

4.3 Development of the Metamaterial

Traditionally, unit cell AEMM with specific geometric configuration and loading conditions can provide local resonance at a unique frequency. A unit cell AEMM is shown in figure 4.3(b). The unit cell (dimension: 38mm X 38 mm X 25 mm) consists of a cylindrical matrix that is encapsulated in a concrete frame. A spherical heavy core made of lead is housed inside the matrix. The diameter of the core mass and the matrix are ~12.5 mm and ~25 mm, respectively. The mechanical properties of the cell constituents can be found in Table 4. 1. This unit cell is proposed to be used as the building material for the sound-absorbing MetaWall. A MetaWall brick without the embedded piezoelectric material was separately made to decommission and the compressive strength of the brick was found to be ~6.25 MPa. To demonstrate the concept of the proposed MetaWall, a three-dimensional model with 16-unit AEMM cells is considered as shown in Fig. 4.3(a).

Hence, the MetaWall is a stack of the unit cell with consistent geometric and mechanical configurations. Though in this article, MetaWall's capability with a specific acoustic frequency is tested, MetaWall with varied unit cell configurations can perform a similar operation within a broad spectrum of noise.

Table 4. 1: Material properties of the cell constituents

Material	Density (kg/m^3)	Young's Modulus (Pa)	Poisson's ratio
Rubber	1600	0.9942e6	0.47
Concrete	2010	11.2e09	0.20
Lead	11340	13.5e09	0.43

Since the proposed MetaWall brick consists of a series of AESC cells, the brick has the capability of harvesting energy trapped inside, while filtering the acoustic noises through the composite. To harvest energy, the proposed MetaWall is modified by placing piezoelectric materials inside the unit cell of AESC by judicially analyzing the vibration mode of the soft constituents. Two different types of piezoelectric materials were analyzed a) ceramic Lead Zirconate Titanate (PZT) wafer and b) polymer Polyvinylidene Fluoride (PVDF) film. Both materials were first compared with different configurations. To keep the resonance frequency below 500 Hz one specific orientation was adopted as discussed in the subsequent sections.

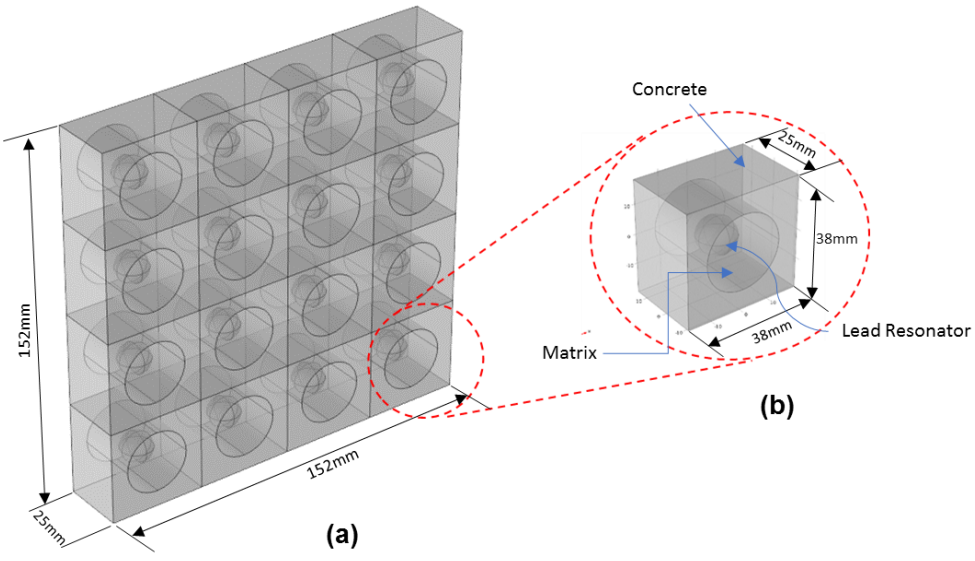

Figure 4. 3 (a) 3D view of the wall with 16 cells; (b) unit cell of the wall

Two arrangements of MetaWall are proposed in this work. Those are 1) concrete free surface and 2) matrix free-surface arrangements. In the concrete free surface arrangement, the MetaWall has been placed in such a way that the concrete frame of each unit cell remains free and encounters direct acoustic incidence. Since a multi-layered MetaWall is more practical for industrial application, only the front of the first layer of the concrete free surface will encounter the dynamic excitation. In the case of the matrix free-surface arrangement, the unit-cell MetaWall is rotated, and the matrix constituent of the cell will remain free and will be exposed to the sound. In a multi-layered matrix free-surface arrangement, the single and double capping configurations are envisioned to enhance the local and global power output. Additionally, a reasonable gap is considered between two adjacent layers in case of single cover design. Detailed reasoning behind such proposals can be found in later chapters. Finally, the proposed MetaWall was fabricated, and energy harvesting capability was tested numerically and experimentally.

4.4 AEMM model as noise barrier

4.4.1 AEMM MetaWall as Noise Barrier

In this study, an arbitrary frequency of ~460 Hz(<500Hz) is considered to filter and test the acoustic noise filtration capability of the unit cell AEMM. Finite element analysis tool (COMSOL Multiphysics) was used in this work to investigate the target objective. Since energy trapping is the key to filtering acoustic waves using AEMM, it is crucial to have local resonance phenomena in the unit cell AEMM at the frequency of interest (~460 Hz). To investigate the existence of local resonance modes around ~460Hz, the dispersion curve of the unit cell is computed. To numerically compute the dispersion relation the unit cell is considered infinite both in x- and y-directions by arranging the unit cell periodically.

Bloch–Floquet periodic boundary conditions [140] are applied at all boundaries of the unit cell. The Bloch–Floquet boundary conditions are based on the Floquet theory which can be applied to the problem of small-amplitude vibrations of spatially periodic structures. The dispersion curve of the unit cell is shown in figure 4.4(a). Two flat bands can be observed in the proximity of ~461 Hz, which denotes local resonance at corresponding frequencies. To identify the existence of local resonance frequency more convincingly, Density of States (DOS) is computed at each frequency within the frequency range of 300-500 Hz. DOS of the system is the number of states (modes) that exist at each frequency level. A high DOS at a specific frequency level means that there are multiple modes available for occupation. Maximum DOS can be obtained where the frequency band is almost straight in the dispersion curve, which means the group velocity is close to zero and the wave energy is trapped inside the structure. Zero DOS at any frequency means that at that frequency no modes could occupy any level (termed as stopband) of the energy. For highly dispersive unimodal wave motion, the DOS is very small but not zero. DOS is calculated from the dispersion relation by applying the relation

$$DOS(\omega) = \frac{1}{\pi}\left({}^{dk}/_{d\omega}\right) \quad \text{.....Eq 4. 1}$$

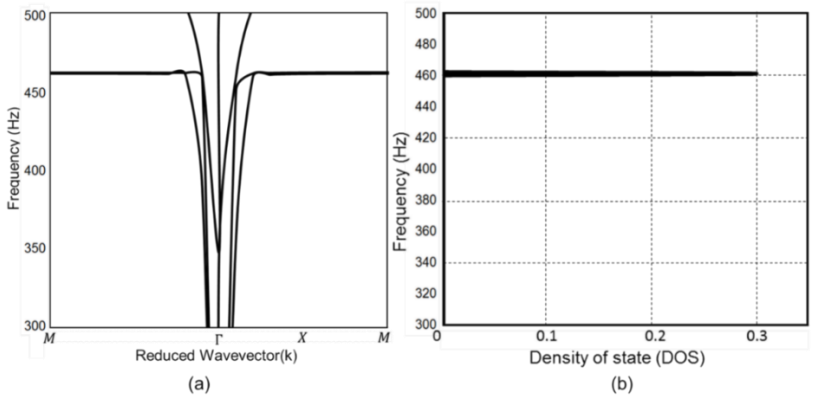

Figure 4. 4: (a) Band structure of the unit AEMM and (b) density of state representation of the unit AEMM

In calculating the DOS, the total wave number $\sum dk$ is computed for each frequency with frequency step $d\omega = 1Hz$[147]. Figure 4.4(b) shows the computed DOS for the frequency range 300-500 Hz. The DOS peak at ~460 HZ corresponds to the flat band in the dispersion plot in figure 4.4(a) and confirms the existence of the local resonance at ~460 HZ.

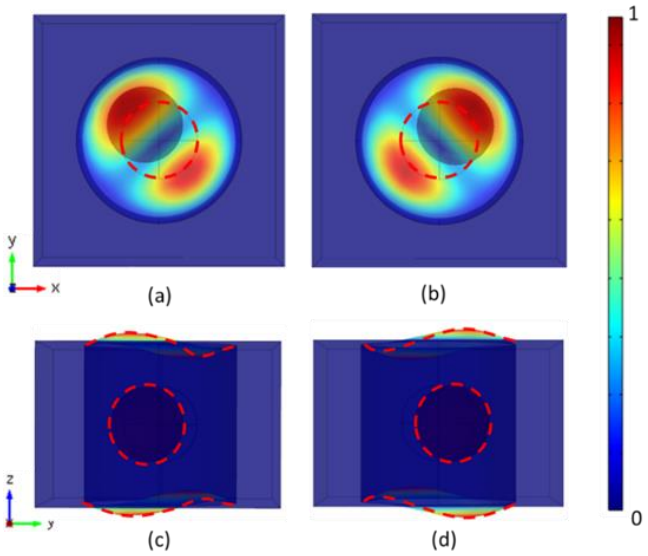

Figure 4. 5: Displacement plot of a unit cell of the MetaWall at (a) Top view of the cell at 460Hz (b) Top view of the cell at 461Hz (c) side view of the cell at 460Hz (d) side view of the cell at 461Hz

To understand the vibration pattern of the constituents at local resonance frequencies, modal displacements of the unit cell is investigated. Figure 4.5 shows the displacement profiles at two DOS peak frequencies (460 Hz & 461 Hz). It can be seen that, at both the local resonance modes, the core mass is resonating, and the acoustic energy is trapped inside the matrix constituent of the cell as dynamic strain energy. It has also been noticed that both the vibration modes are 90^0 mirror images of one another. This confirms that both the modes representing the same vibration mode and only one local resonance frequency exist at ~461 Hz. Hence, it can be concluded that using unit cell AEMM with

proposed mechanical and geometric configurations; it is possible to trap acoustic energy at ~460 Hz inside the AEMM. The following section provides a clear insight; how much acoustic noise can be filtered through such an energy trapping process.

4.4.2 Analytical Study

While the numerically computed outcomes in the previous section confirm the existence of local resonance mode and the possibility to trap acoustic energy in unit cell AEMM at ~460 Hz, an analytical study is performed herein to validate the numerical claims. The unit cell AEMM can be evaluated as a spring-mass system as shown in figure 4.6(a). For analytical validation, a one-dimension system is assumed for two principal purposes, 1) computation simplicity, and 2) cell constituent's deformation in other dimensions are neglected since unidirectional acoustic incidence is assumed. Based on the assumptions, the dynamic effective mass of the microstructures can be presented as

$$M_{eff} = M_0 + \frac{2Km_1}{2K - m_1\omega^2} \quad \text{..... Eq 4. 2}$$

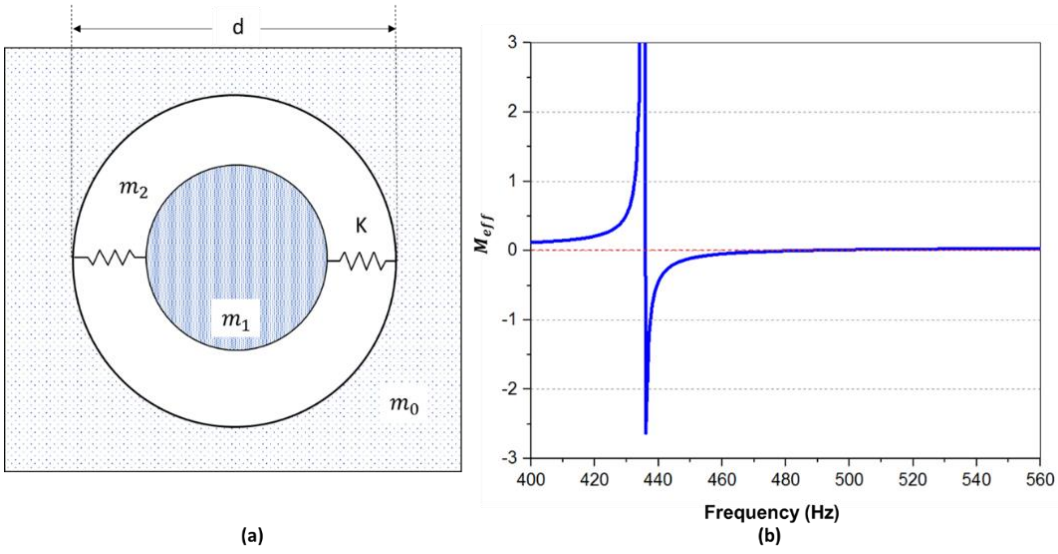

Figure 4. 6: (a) Spring-mass representation of unit cell AEMM (b) Analytically computed dynamic effective mass of the AEMM

Here, M_0 and m_1 are the masses of concrete frame and lead core, respectively. The spring constant for the matrix component is counted as, K = 1 kPa. From Equation (1), the dynamic effective mass of the system is found to be negative at ~440Hz, as shown in figure 4.6(b) which can be counted as local resonance frequency according to the established literature[148]. While ~460 Hz is recorded as the local resonance frequency of the unit cell AEMM, a little deviation is measured in analytical computation due to the adaptation of assumptions as mentioned above. Hence, it can be claimed that the analytical study supports the numerical computer to a good degree.

4.4.3 Filtration of Acoustic Energy

Based on the above discussions, it is evident that under any vibroacoustic loading condition, the AEMM unit cell can trap acoustic energy at a specific frequency inside the soft matrix due to their unique material properties. However, the capability of the AEMM MetaWall as a noise filter through such energy trapping is yet to be tested. A MetaWall placed in highways or industries are not only exposed to increased acoustic pressure, but also environmental ground vibration. This vibration is generated due to the vibroacoustic waves originated from the movement of traffic or vibration of heavy industrial machinery under operation. Hence, to demonstrate the capability of the MetaWall in filtering acoustic pressure, a virtual experiment is created using COMSOL Multiphysics. Frequency-domain analysis is performed applying unit pressure (~94dB) at the boundary of the incident acoustic domain (ref: figure 4.7 (a)). To consider the input load as acoustic pressure, a long air duct of length L is designed at both input and receiving ends of the AEMM (figure 4.7)

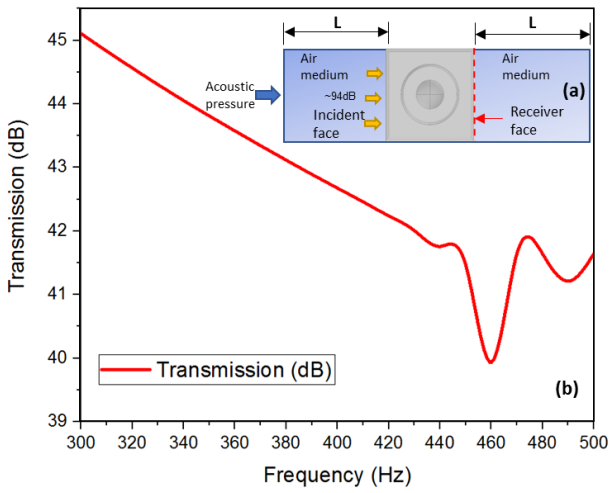

Figure 4. 7: (a) Acoustic pressure test setup; (b) Filtration of the acoustic noise in the matrix

L is defined as twice the wavelength concerning the maximum frequency studied in the air medium. Fig. 4.4(b) shows the acoustic pressure level at the receiver surface of the AEMM for a range of acoustic frequencies. A drop-in acoustic pressure amplitude (dB) is visible for all the frequencies at the receiving end, compared to the incident 94dB pressure. However, a significant drop of around ~57.7% is recorded in the vicinity of the resonance frequency. Hence, this study confirms AEMM MetaWall as a potential noise barrier with almost ~60% noise reduction capability.

4.5 AEMM model as energy harvester

4.5.1 Potential use of the Filtered Acoustic Energy

Since acoustic energy is trapped inside the metamaterial in the process of filtering noise, it is possible to recover this abundant energy as usable electric potential[60]. Two piezoelectric material types (ceramic wafer and PVDF) were considered independently inside the unit cell AEMM to convert the trapped strain energy into electric power.

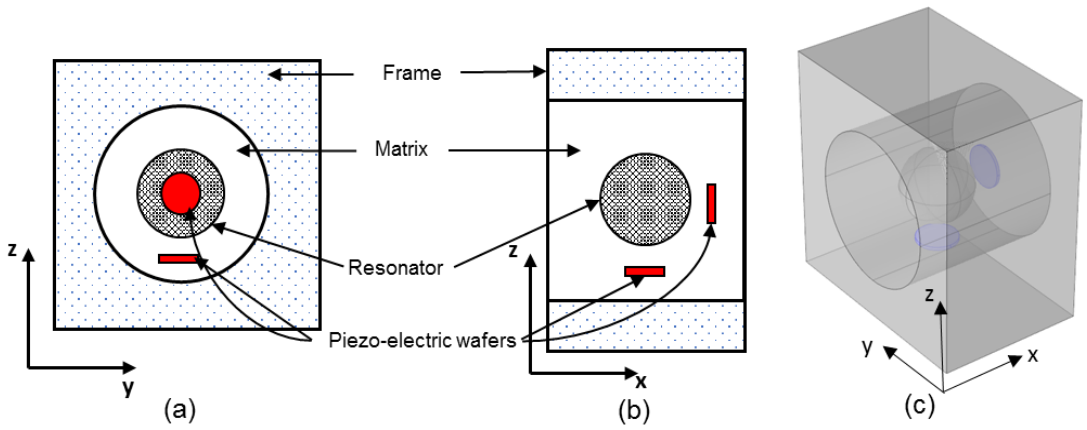

Figure 4. 8 Placement of the piezoelectric wafers or PVDF membrane to maximize power output (a) plan view and (b) side view; (c) proposed piezoelectric material placement in a unit cell to harvest energy from the resonance mode

Harvesting energy from AEMM at different vibration modes has already been reported in previous articles [149]. To harvest the maximum possible energy trapped inside the cell, strategic placements of the energy conversion material inside the soft-core constituents of the AEMM is important. Each local resonance mode arrests the dynamic wave energy inside the matrix constituent of the cell. Hence, it is expected that appropriate placement of an energy conversion material, capable of mechanoelectrical transduction, with the proper design of the matrix component can provide a significant electric potential at the local resonance frequencies. Figure 4.8(a,b) shows the proposed placement of the piezoelectric material in the unit cell. It has been found that in unit cell AEMM, after placing PZT (7mm Dia. And 0.5mm thickness) inside the cell, there are always two dominant vibration or local resonance modes exist, 1) core mass resonated along the axis of excitation, 2) core mass resonated along the thickness axis of PZT unless the thickness axis is making a right angle with the axis of excitation. One additional vibration mode with little dominance is also identifiable along the gravitational (z-) axis of the resonator. It is possible to have maximum power from a PZT if all three vibration modes coincide.

However, due to application compatibility, in this work, it's not possible to coincide with the axis of excitation and gravitational axis. Hence, two piezoelectric wafers are proposed herein to extract the maximum power from the unit cell AEMM. While one PZT will coincide with the axis of the excitation and PZT thickness axis, the other PZT will generate power due to the gravitational effect of the core resonator figure 4.8. In all the above cases, PZT is placed in the middle of the core surface and frame inside the boundary.

On the other hand, similarly at similar locations, PVDF materials of same dimensions (7 mm. dia.) were placed (except the thickness was 100µm). When the PVDF material was used only one resonance frequency was found due to the core mass only in the AESC. However, the energy output of the PVDF membrane from the MetaWall was 66% higher compared to the PZT around the ~460 Hz. It was found from an analysis using a single AESC unit that higher surface area of the PVDF in a cylindrical configuration around the resonator could result in much higher energy output, but the resonance frequency was well above the specified limit of application which is below 500 Hz considered herein. Hence, such configurations of the PVDF membrane inside AESC are not reported in this article but might be suitable for different applications. The material properties for PZT-5H (density 7500 kg/m3) and PVDF (density 1780 kg/m3) used in the simulation written in the following equations

PZT-5H Compliance Matrix:

$$S = \begin{bmatrix} 16.5 & -4.78 & -8.45 & 0 & 0 & 0 \\ -4.78 & 16.5 & -8.45 & 0 & 0 & 0 \\ -8.45 & -8.45 & 20.7 & 0 & 0 & 0 \\ 0 & 0 & 0 & 43.5 & 0 & 0 \\ 0 & 0 & 0 & 0 & 43.5 & 0 \\ 0 & 0 & 0 & 0 & 0 & 42.6 \end{bmatrix} \times 10^{-12}\, Pa^{-1} \text{.....Eq 4. 3}$$

PZT-5H Piezoelectric charge constants or the coupling matrix:

$$d = \begin{bmatrix} 0 & 0 & 0 & 0 & 741 & 0 \\ 0 & 0 & 0 & 741 & 0 & 0 \\ -274 & -274 & 593 & 0 & 0 & 0 \end{bmatrix} \times 10^{-12} C/N \quad \text{..... Eq 4. 4}$$

PZT-5H Relative permittivity matrix:

$$\varepsilon = \begin{bmatrix} 1704.4 & 0 & 0 \\ 0 & 1704.4 & 0 \\ 0 & 0 & 1433.6 \end{bmatrix} \text{..... Eq 4. 5}$$

PVDF Compliance Matrix:

$$S = \begin{bmatrix} 4.06 & -5.09 & -10.12 & 0 & 0 & 0 \\ -5.09 & 2.20 & -8.75 & 0 & 0 & 0 \\ -10.12 & -8.75 & 15.28 & 0 & 0 & 0 \\ 0 & 0 & 0 & 1.82 & 0 & 0 \\ 0 & 0 & 0 & 0 & 1.69 & 0 \\ 0 & 0 & 0 & 0 & 0 & 1.43 \end{bmatrix} \times 10^{-12}\, Pa^{-1} \text{ ..... Eq 4. 6}$$

PZT-5H Piezoelectric charge constants or the coupling matrix:

$$d = \begin{bmatrix} 0 & 0 & 0 & 0 & -0.137 & 0 \\ 0 & 0 & 0 & -0.126 & 0 & 0 \\ -0.93 & -0.67 & 2.8 & 0 & 0 & 0 \end{bmatrix} \times 10^{-12} C/N \text{ .....Eq 4. 7}$$

PZT-5H Relative permittivity matrix:

$$\varepsilon = \begin{bmatrix} 12 & 0 & 0 \\ 0 & 12 & 0 \\ 0 & 0 & 12 \end{bmatrix} \text{.....Eq 4. 8}$$

In figure 4.8, the placement of piezoelectric materials to harvest energy at the frequency ~460Hz is proposed. Hence, to verify the concept of transforming the trapped acoustic energies into usable electric potential, the model is numerically simulated using COMSOL Multiphysics. In the model both types of piezoelectric materials namely, PZT and PVDF materials were used, independently. As described in the introduction section, two arrangements of MetaWall (concrete free-surface and matrix free-surface) are

proposed in order to change the incident face of the brick and observe the change in our expected output. Both configurations were tested with both types of piezoelectric materials. In concrete free-surface set up, the concrete frame of each unit cell remains as the free surface to experience the direct acoustic incidence. In the case of matrix-free surface configuration, the unit cell is rotated, and the surface with a matrix constituent of the cell will be exposed. Multi-layered MetaWall can be a practical choice for industrial application for robustness and improved performance with required compressive strength. In the case of a matrix-free surface arrangement, if the bricks are placed right one after another, the matrix constituent will be continuous along with the whole thickness and could not feel any resistance to experience sufficient strain. Such an arrangement may reduce the local strain energy and total power output. Hence, a capping mechanism is envisioned to enhance the local strain energy in each cell. Both single and double cover configurations are considered, where a reasonable gap is considered in between two adjacent layers in case of single cover design.

Such a gap is important to distinguish between single and double capping, as well as keeping the local resonance frequency for the whole MetaWall brick consistent. It was found that any arbitrary arrangement of capping was not suitable, and the resonance frequency might go well above 500 Hz and is not desired. With the capping arrangement proposed herein, the resonance frequency was very close and right around ~500 Hz with both single and double cover case. Capping arrangement will be fruitful for both types of piezoelectric materials. Though, a multilayer MetaWall arrangement is important for the industrial application, for computation simplicity, in this work, a single layer brick with 16-cell AESC are investigated.

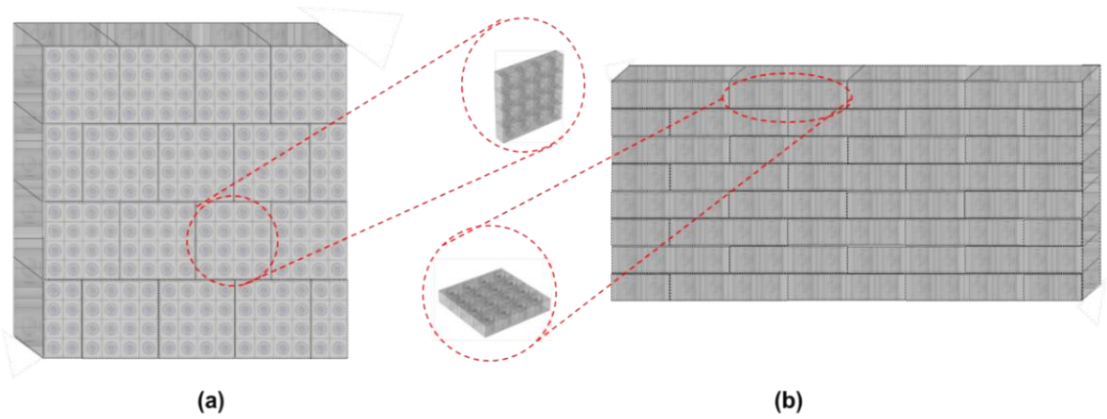

Figure 4. 9: Two different arrangements of the MetaWall brick (a) concrete free surface arrangement (b) matrix free surface arrangement

4.5.2 Concrete Free Surface Arrangement

As conceptualized and proposed, the model is placed in such a way that the concrete frame of the unit cell remains as the free surface of the MetaWall. Here, the displacement boundary condition is applied along the thickness direction of the MetaWall to simulate effective acoustic and ground vibration. Hence, the matrix surface remains parallel to the axis of excitation. Also, the direction of the excitation coincides with one piezoelectric material (PZT or PVDF as used) placed in the unit cell.

The displacement plots of the respective cells at three different frequencies around ~420 Hz, ~460Hz, and ~490Hz using both PZT and PVDF materials are shown in Figure 4.10. At local resonance frequency around ~460 Hz, it can be seen that maximum strain energy is trapped inside the matrix constituent with PZT and PVDF material as shown in Figure 4.10(b)(e), respectively. Hence, the PZT and PVDF piezoelectric materials experienced maximum compressive and bending stress, which resulted in maximum power output (~1.3mW from PZT and ~2.1mW from PVDF) as presented in figure 4.14 (a) and (b), respectively. While a local resonance frequency of ~460 Hz was reported in earlier

sections from eigenfrequency analysis, a little shift is recorded in this section due to the addition of an extra mass (PZT) in the unit cell.

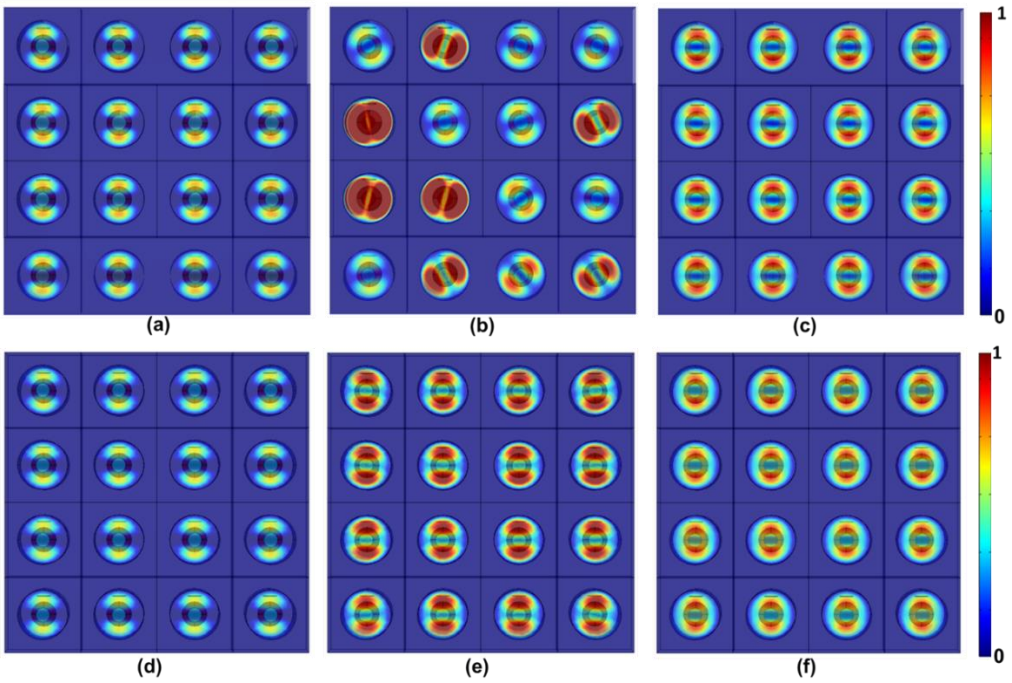

Figure 4. 10: Displacement plot at frequency (a) f_1(420Hz) (b) f_2(458Hz) (c) f_3(490Hz) using PZT and displacement plot at frequency (d) f_1(420Hz) (e) f_2(458Hz) (f) f_3(490Hz) using PVDF

4.5.3 Matrix Free-Surface Arrangement

In another arrangement of the MetaWall with the matrix-free surface, the model is placed in such a way that the matrix surface remains perpendicular to the axis of excitation. In this arrangement of the bricks, two configurations are considered. In the first configuration, the MetaWall has a thin layer of cover on both sides of the concrete frame which was originally considered open to the atmosphere in other arrangements This type of arrangement is chosen in order to fulfill the requirement of a wall with multiple layers of brick. The ones which will be in the middle layers will have both its faces covered by other layers.

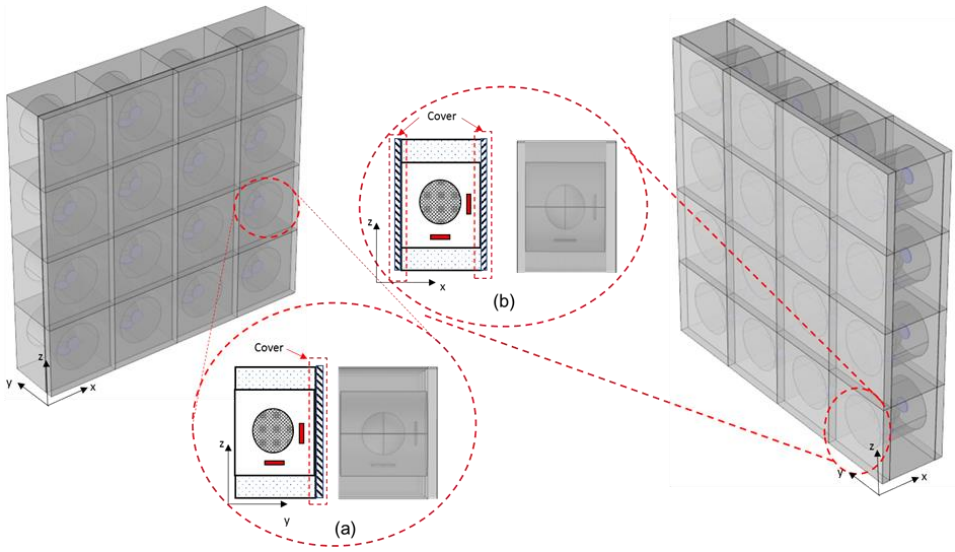

Figure 4. 11: Illustration of a unit cell of MetaWall brick with (a) single cover; (b) double cover

In another setup, cell cover is considered on one face of the unit cell, preferably on the side where the piezoelectric wafers are placed on top of the resonator (see Figure 4.11 (a)). In the arrangement, when the covers are placed on both sides, the resonance frequency was found to be higher (~508HZ) compared to the resonance frequency of the wall without a cover (~460Hz) (ref. Figure 4.15). On the other hand, for the arrangement that has a one-sided cover, the resonance is reported at a higher resonance frequency (~500Hz), which is comparatively lower than the frequency reported with double-sided covers on the MetaWall (~508Hz). Adding cover in the cell makes the soft rubber stiff and leaves very little room to deform. Hence, with double cover resonance frequency shifted to higher frequency compared to the cell with a single cover.

4.6 Experimental Process

In this section, the concept of harvesting energy from the concrete free-surface model of the AEMM MetaWall brick is experimentally validated. A full-scale MetaWall brick is

fabricated in the laboratory and the fabrication steps are discussed as follows. First, the cylindrical acoustoelastic sonic crystals are fabricated using an established method reported by Ahmed et al. [67] with a few additional steps discussed in this section.

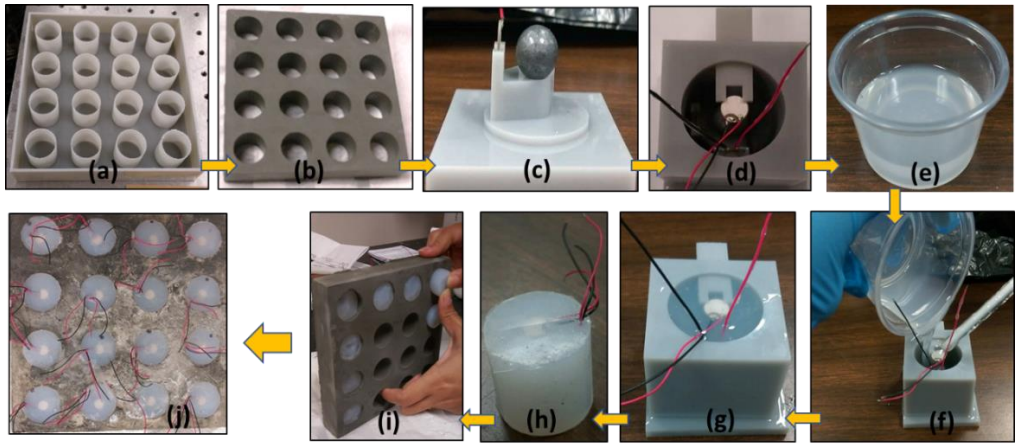

Figure 4. 12: (a-i) Fabrication steps of the MetaWall brick (j) the final form of the brick.

To fabricate the concrete structure, a mold is first designed and then fabricated using 3D printing technology (Figure 4.12 (a)). Portland cement concrete mortar mix prepared with water in a 0.5/0.5 mixing ratio is used to build the structure. A cylindrical support to place the resonator ball was fabricated using 3D printing technology in between the energy transduction units and the pins for holding the piezoelectric wafers in their designated places. The mold for making the harvesters is shown in figure 4.12(d). After the placement of the lead resonator and the wafers, liquid rubber (Mold star 20T, contains two parts (A & B)), is used to fill the hole in 3D printed block. Since it is necessary to sense or transfer the strain energy trapped inside the rubber component, the piezoelectric wafers (with electric wires) were fully submerged into the liquid rubber in such a way that it remains untouched by both the lead balls and the mold. It is important to keep the piezoelectric wafers straight. The rubber used in this process has a curing time of 30 mins.

During the initial steps, the cylindrical support and the pins are used to hold the lead ball and the piezoelectric wafers in the middle. So, empty spaces remained at the bottom of the structure after removing the cylindrical support. Another cavity is created after the removal of the top pin. Further, these empty spaces were filled with additional rubber following the same procedure described above. Since it is required to have a good bonding between the two layers of rubber, the second step needs to start before the full curing of the rubber poured first. After the curing process, the energy harvesters look like the one shown in figure 4.12(h).

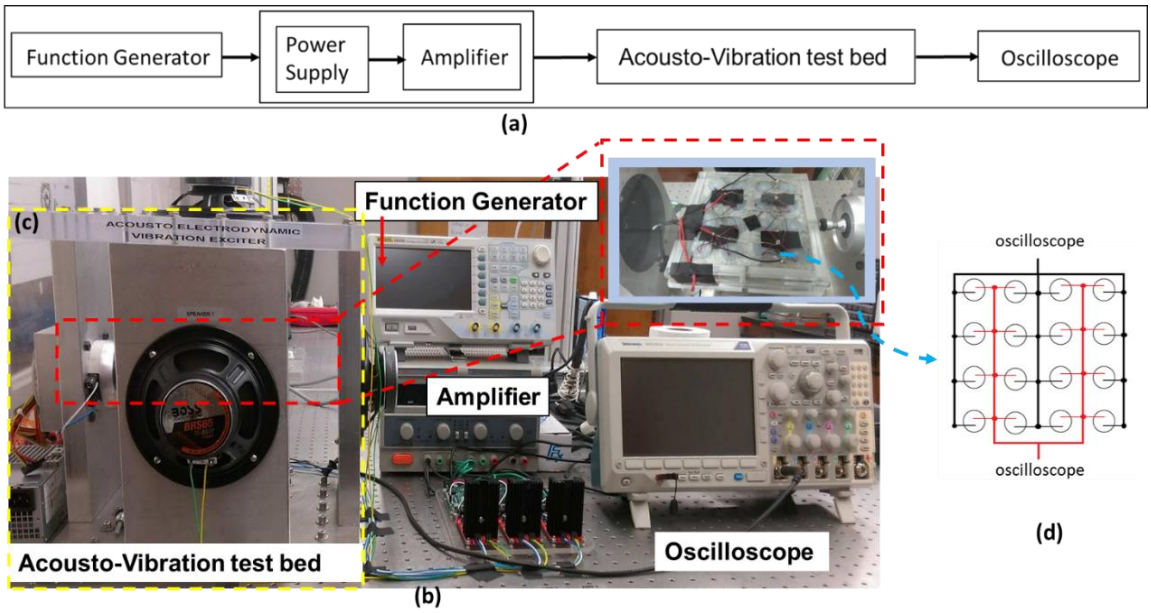

Figure 4. 13: (a) Sequence of the experimental process to harvest energy from the vibration test bed (b) Experimental configuration of MetaWall brick to harvest energy (c)Customized acousto-vibration test bed (d) circuit diagram of the parallel connection used to connect the piezoelectric wafers embedded in the unit cells.

All 16 sonic crystal harvesters are made in the same process. Once all the crystals are completed, they are inserted into the cylindrical hole in the concrete frame (Figure 4.12(i)) of the MetaWall. Then, the MetaWall brick is ready for the experimental investigation (Figure 4.12 (j)). A customized 3D acousto-vibration testbed[150] is used to

perform the experiments. The vibration testbed is shown in figure 4.13 (b) The voltage output from the piezoelectric wafers is captured in parallel connection across a 10 KΩ resistive load and power density is calculated. The circuit diagram for connecting the wafers in parallel connection is displayed in Figure 4.13(c).

4.7 Results and Discussion

Hence, the PZT and PVDF piezoelectric materials experienced maximum compressive and bending stress, which resulted in maximum power output (~1.3mW from PZT and ~2.1mW from PVDF) as presented in Figure 4.14 (a) and (b), respectively. While a local resonance frequency of ~460 Hz was reported in earlier sections from eigenfrequency analysis, a little shift is recorded in this section due to the addition of an extra mass (PZT) in the unit cell.

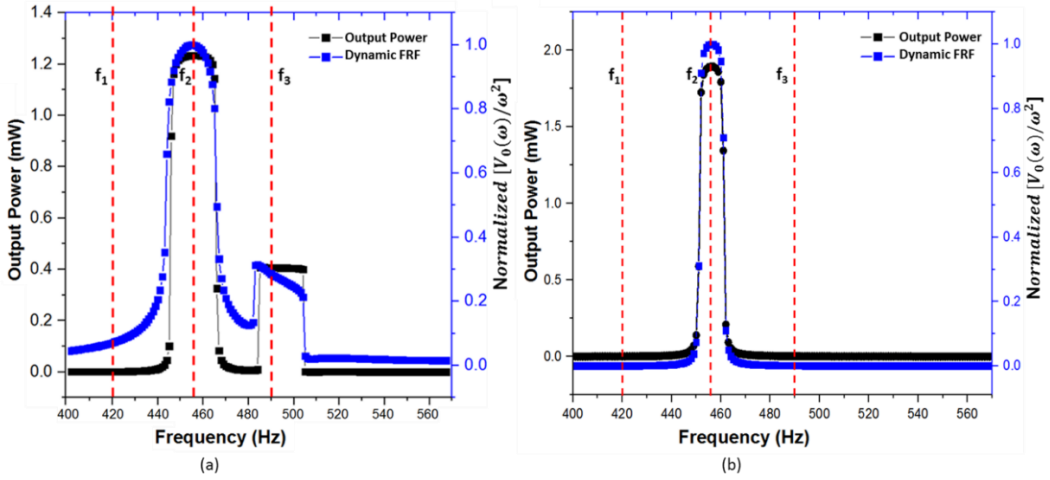

Figure 4. 14: Power output and normalized voltage output from (a) a single layer of the multi-layer MetaWall model with PZT (b) a single layer of the multi-layer MetaWall model with PVDF

The displacement plots of the respective cells at three different frequencies at 420 Hz, 458Hz, and 490Hz. are shown in Figure 4.10. At local resonance frequency, 458 Hz, it can be seen that maximum strain energy is trapped inside the matrix constituent (ref. Figure 4.10 (b), (e)). Hence, the piezoelectric wafers experience maximum compressive

stress, which resulted in maximum power (~1.2mW from PZT and 2.1mW from PVDF) output as can be seen from Figure 4.14. While a local resonance frequency of ~460 Hz was reported in earlier sections from eigenfrequency analysis, a little shift is recorded in this section due to the addition of an extra mass (PZT and PVDF) in the unit cell.

To simulate the possible power output from the MetaWall using PZT and PVDF independently, 10KΩ resistive load was added to the models. The maximum power harvested by PZT from a MetaWall with a double-sided cover arrangement was found to be around ~5.7 mW, and with the single sided cover was around ~8.8mW. Similarly, the maximum power harvested by PVDF from a MetaWall with a double-sided cover arrangement was found to be around ~2.5 mW, which is significantly lower than the PZT. However, with the single sided cover arrangement the harvested power was ~30% higher and was around ~11.5mW with PDVF compared to PZT based walls. It was found that the resonant frequencies, however, were around ~485 Hz and ~530 Hz, respectively. Generally speaking, the power harvested from a single covered MetaWall is significantly higher than the one with a double cover MetaWall. Since in double cover configuration, the matrix constituent is capped from all sides and enclosed in a closed space, the constituent can experience less deformation compared to the cell with just one side capped. Hence the piezoelectric wafer inside the double cover cell experiences less strain and results decreased power output compared to the model with a single cover. Figure 4.15 (a) shows the power output from single and double cover wall using PZT and Figure 4.15 (b) shows the power output from single and double cover wall using PVDF. This concludes that if the double-sided cover is absolutely necessary, embedding PZT would be beneficial compared to PVDF. From the numerical study, ~1.2mW maximum power was recorded

from the entire brick upon unit displacement (1 mm) excitation when the PZT was used as the smart material inside the harvester. Fig. 5.9 shows the experimental power output curve obtained from several experiments

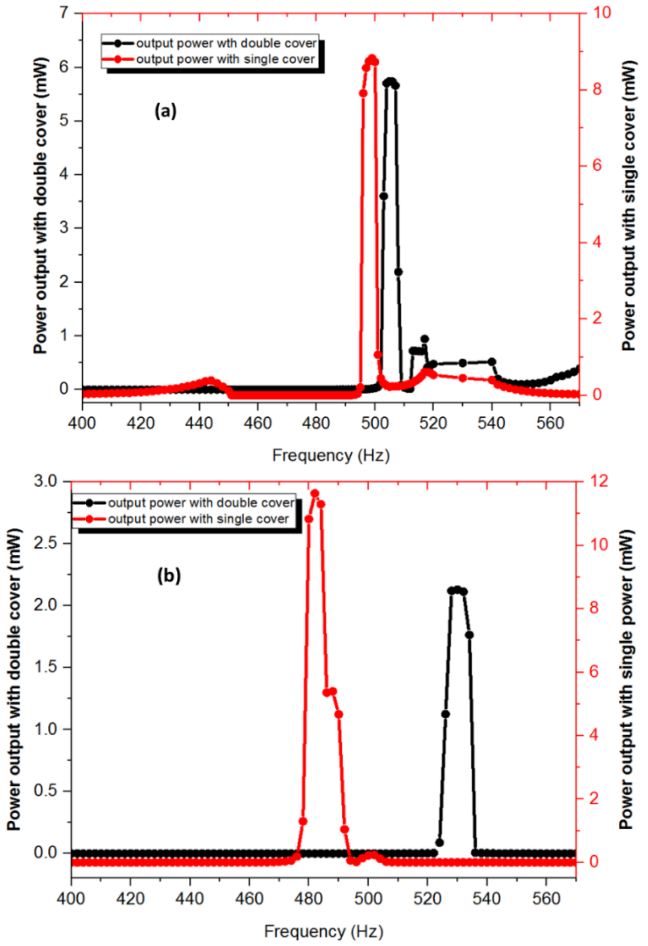

Figure 4. 15: a) Power output in vertical arrangement with cover on both sides and with single cover using embedded PZT, b) Power output in vertical arrangement with cover on both sides and with single cover using embedded PVDF

It can be seen that the mean experimental power output is ~0.45mW near ~490Hz. While the numerical power output is ~1.2mW around the frequency (~460Hz). Error bar (only positive error bars are shown) with one standard deviation in Fig. 5.9 shows that the maximum power output could be ~0.55 mW from the wall that was fabricated in the laboratory. Another observation can be made that the standard deviation is higher towards

the lower frequencies compared to the higher frequencies above ~490 Hz. The result shows that at close proximity to ~460 Hz, at 490 Hz < 500 Hz, the maximum power could be harvested from the MetaWalls, while retaining their compressive strength as desired in a structural material. The result closely supports the analytical and numerical argument which says that the maximum power is to be obtained around ~460 Hz. However, a 30Hz shift in the resonance (or, peak power output) frequency is the result of many factors. Primarily this mismatch is due to the fabrication error, placement of the resonators, the exact inclination of the piezoelectric wafers which might have tilted during pouring the rubber into the mold and concrete strength after curing, etc. The material properties of the concrete used are provided by the vendor, which is used in the simulation and might not exact. However, after curing the small perturbation in the material properties of the core structure may have shifted the resonance frequency which is previously investigated.

A similar argument holds true for the maximum power output which is close to 50% of the simulated power output. A similar investigation was conducted on the MetaWall brick with embedded PVDF of the same size. Although the numerical simulation results in higher power output compared to PZT based MetaWall, ~2.1 mW, the energy output from experiments were not promising (~0.22 mW) and inconsistent between a different set of experiments, hence, not reported herein. This is not to report that the PVDF cannot work for MetaWalls but requires different fabrication process by virtue of which the higher energy output could be achieved as predicted in Figure 4.14 (b) and Figure 4.15 (b). This is primarily due to the difficulty in fabricating the PVDF based MetaWalls using the process described above. However, a different optimized process could result in a better

fabricated product of MetaWall with PVDF, which is not reported or investigated in this article.

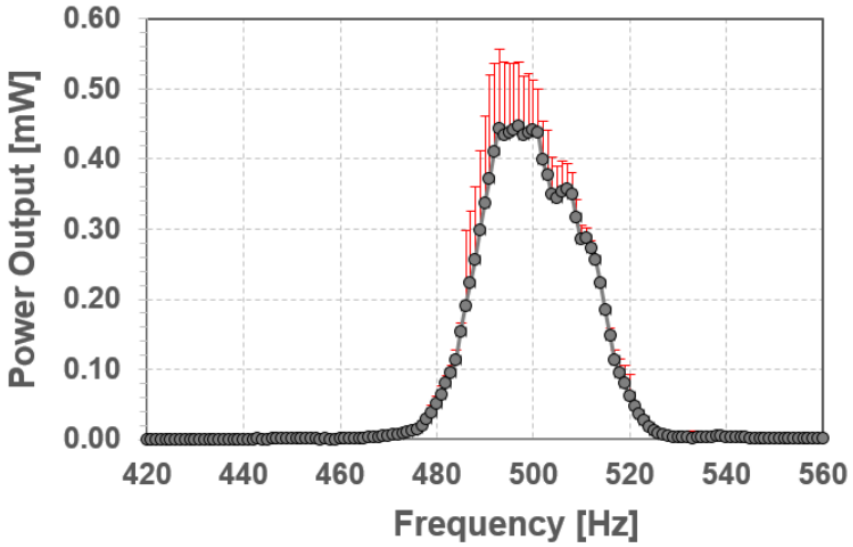

Figure 4. 16: Experimental power output from the proposed model

4.8 Comparison of the AEMM Models

So far we have discussed the capability of harvesting energy from AEMM cells with concret frame and piezoelectric materials(PZT-5H and PVDF film). But there are possibilities that with the change of the frame material or the shape and size of the piezoelectric material the energy harvesting capability of the AEMM model changes. In this section, four different combination of the cells are studied.

4.8.1 Case Studies of the AEMM Models with Different Conditions

Here the studies are conducted on a unit cell of AEMM model. The unit cell has a dimension of (38mmX38mmX25mm). The piezoelectric materials used are PZT-5H (cylinder and disc form) and PVDF film. The frame materials used are concrete and PVC.

Two orientations of the cells are considered for this study as upright and rotated(ref- Figure 4.17). the core resonator is a lead ball.

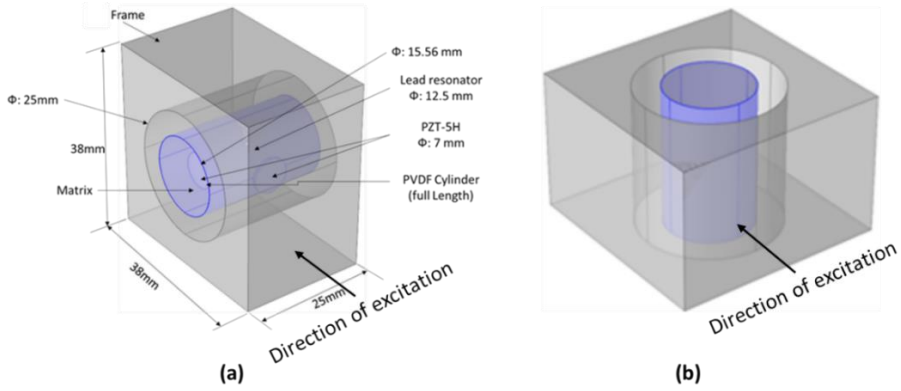

Figure 4. 17: 3D view of the unit cell in (a) rotated (b) upright position

The material properties of the cell constituents are given in table 4.2. The properties of PVDF and PZT-5H are stated earlier.

Table 4. 2:Material properties of the cell constituents

Material	Concrete	PVC	Lead	Rubber
Young's Modulus (Pa)	$11.2X10^9$	$25X10^6$	$14X10^9$	$0.9942X10^6$
Poisson's ratio	0.20	0.40	0.42	0.47
Density(Kg/m^3)	2010	1420	11350	1600

For this study, basically, four combinations are considered, as

1. **PVDF wrap**: the PVDF film is wrapped around the core resonator.
2. **PVDF cylinder**: PVDF film is placed inside the rubber matrix in a cylinder form. The length of the cylinder is varied to see the possible outcomes.

3. **PZT-5H cylinder**: a cylinder form of the PZT-5H(dia. 6mm height 12mm) is used. The cylinder acts as both the resonator and the piezoelectric material. PVDF cylinder is also coupled with this PZT cylinder in one of the cases.
4. **PZT-5H disc and PVDF cylinder:** PVDF in the form of cylinder coupled with PZT-5H discs are considered. The lead ball acts as a core resonator.

All these cases are studied with concrete and PVC frame. The orientation of the frame was changed from upright to rotated for each case. The cases are shown in details in Table 4.3..

Table 4. 3 Cases of the AEMM cell study conditions

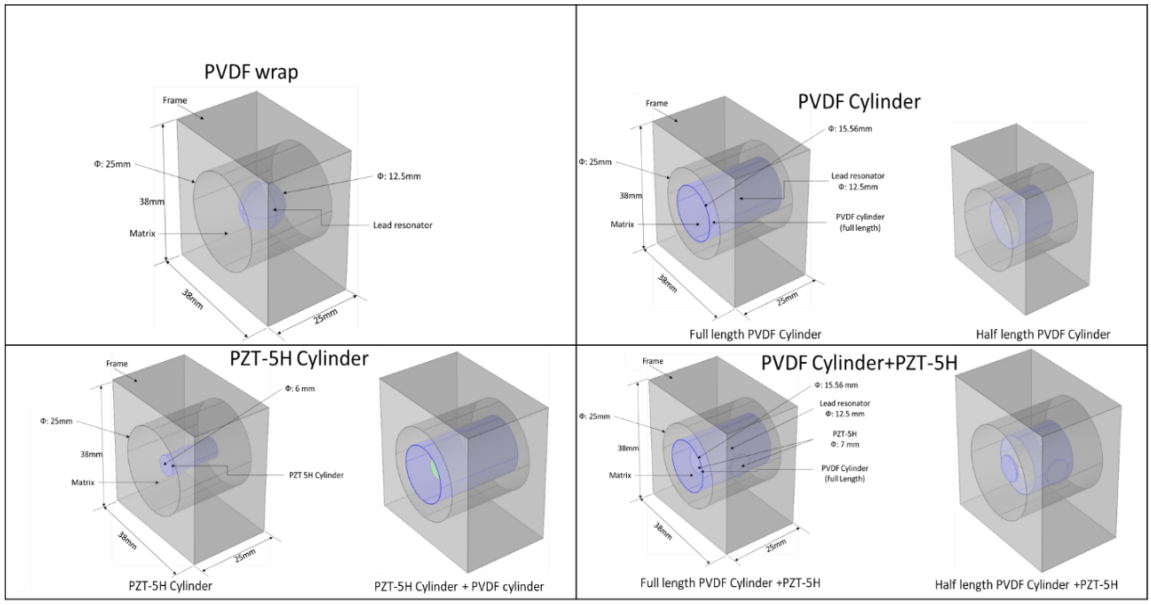

4.8.2 Results and Discussion

Finite element simulation tool COMSOL was used to run the simulations on these unit cells. Each of the cases with two types of orientation was simulated. The studies show that the resonance frequency and the output power differs with the frame material. Also, the output power is different with the orientation of the frame. The results are compared in table 4.4 and table 4.5 below.

From these results, it can be seen that for all of the cases, the power output is higher for the rotated orientation. The reason behind this phenomenon is the effect of the gravitational force. Apart from the applied desired excitation, this gravitational force also acts as a form of excitation. This helps to apply strain to the PVDF film or the PZT discs. So, this multi-directional strain results in higher output power. For most of the cases, the resonance frequency stays the same. A slight shift in some cases is the result of the gravitational force.

Table 4. 4: Case studies with PVC frame

Serial no.	Case Studies	Power output (mW)	Resonance frequency (Hz)
1.	PVDF film wrapped around the resonator	0.0840	460
2.	PVDF cylinder (full length Cylinder)	i.Upright: 0.722 ii.Rotated: 3.622	560 600
3.	PVDF cylinder (half-length cylinder)	i.Upright: 0.25 ii.Rotated: 0.647	510 530
4.	Full length PVDF cylinder + PZT	i.Upright: 0.135 ii.Rotated: 0.694	650 650
5.	Half-length PVDF Cylinder +PZT	i.Upright: 0.014 ii.Rotated: 0.109	540 530
6.	PVDF cylinder + Cylinder PZT	i.Upright: 2.8 ii.Rotated: 3.83	720 720
7.	PZT Cylinder	i.Upright: 4.2 ii.Rotated: 3.83	560 720

From the results found from the study of the concrete frame, it can be seen that the overall power output scenario is a bit different than that of PVC frame. The power output is comparatively low compared to the same case with PVC frame. The reason behind it is the concrete frame. The density of concrete is higher than that of PVC this allows the lower amount of deformation in the matrix. Thus, a lower amount of strain is created in the piezoelectric material. In this concrete frame also, the rotated orientation results in a higher amount of output power.

Table 4. 5: Case studies with Concrete frame

Serial no.	Case Studies	Power output (mW)	Resonance frequency (Hz)
1.	PVDF film wrapped around the resonator	0.2735	460
2.	PVDF cylinder (full length Cylinder)	i.Upright: 0.6708 ii.Rotated: 0.975	600 680
3.	PVDF cylinder (half-length cylinder)	i.Upright: 0.2588 ii.Rotated: 1.331	540 690
4.	Full length PVDF cylinder + PZT	i.Upright: 0.0526 ii.Rotated: 45.56	680 680
5.	Half-length PVDF Cylinder +PZT	i.Upright: 4.1717 ii.Rotated: 40.16	580 690
6.	PVDF cylinder + Cylinder PZT	i.Upright: 0.2976 ii.Rotated: 0.9396	800 800
7.	PZT Cylinder	i.Upright: 2.822 ii.Rotated: 20.767	590 800

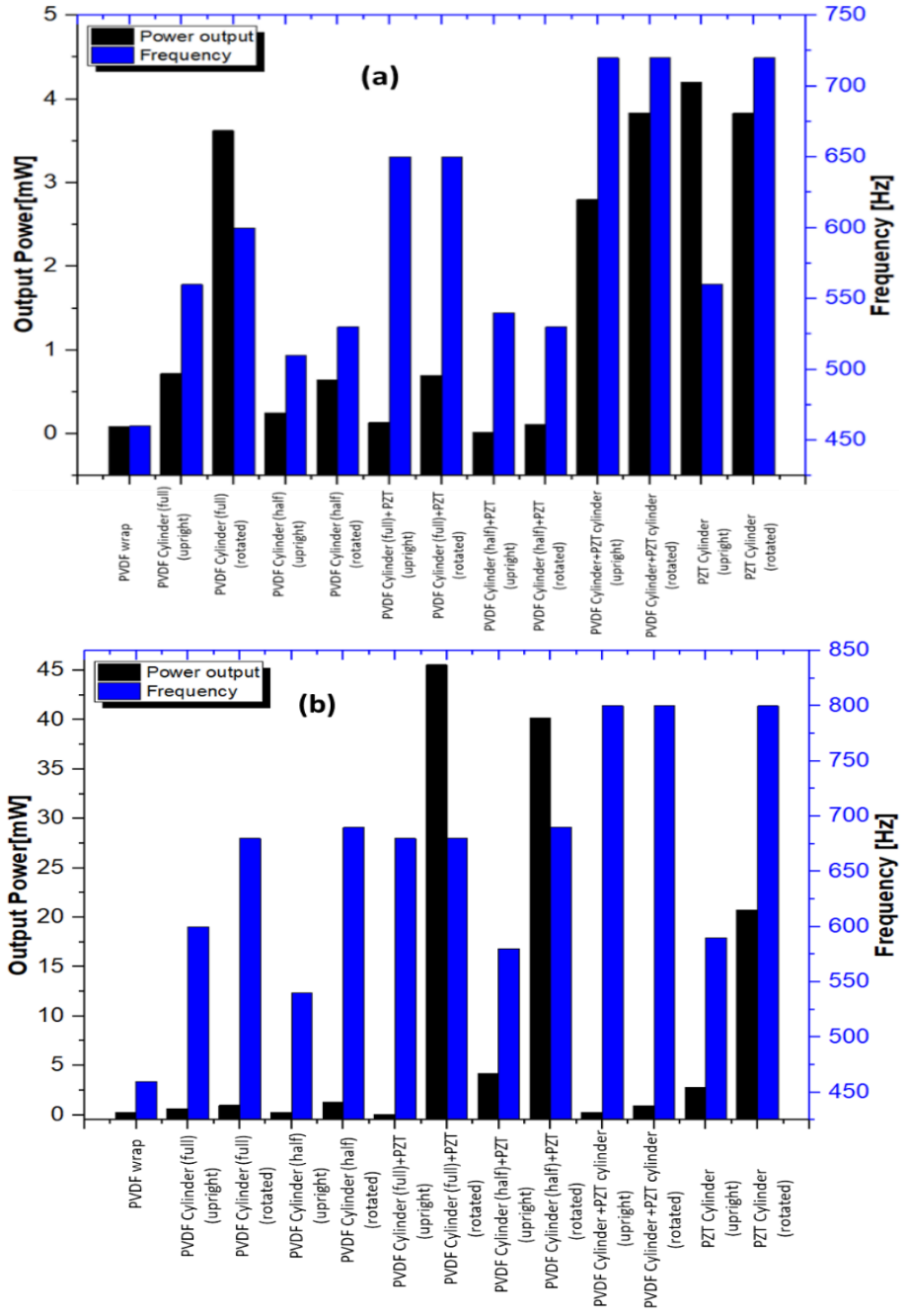

Figure 4. 18:Comparison of the output power and resonance frequency with (a) PVC (b) concrete frame

The resonance frequency for the cases with the concrete frame is much higher than that of with PVC. Due to the denser frame material, the structural stiffness increases, so the resonance frequency goes higher. Though the resonance frequencies for all the cases

are lower than 1000Hz since we are looking for even lower frequency range and the weight of the structure also matters, so, the better choice for this case would be the model with PVC frame. The output power and the resonance frequency of both the frames are compared in figure 4.18.

To summarize, this study proposes an industrial application of the AESC based on their noise filtration capabilities. It is shown that the AESC can trap a certain frequency within its soft matrix due to its unique mechanical properties. Keeping that in mind, it has been proposed to replace the traditional roadside noise barriers with walls made of AESC. A model MetaWall brick is demonstrated that can be used to build the proposed wall. This structure helps to reduce the intensity of the annoying sound by absorbing most of the incident acoustic waves which prevents the sound to reflect to the atmosphere. Acoustic pressure test shows that almost 60% noise attenuation is possible using the MetaWall noise barrier, where traditional barriers offer around 50% attenuation. In the process of filtering acoustic noise, an enormous amount of energy can be trapped inside AESC. Instead leaving these energies abandoned, possible conversion in electric potential is presented, herein. It has been found that, a significant amount of power output can be obtained from the MetaWall which can be used to power the street lights or SHM sensors.

CHAPTER 5

Plate Type Energy Harvester: Model Development and Power Generation

Proper knowledge of any structure's health ensures safety of the structure as well as reduce the maintenance cost and health and environmental effect. Continuous nondestructive structural health monitoring (SHM) using a network of sensors is the most widely used method for this purpose. The sensors used in this field needs constant power source to operate. In such scenario, in house energy harvester is a good choice for supplying power to the sensor network. Earlier researchers have demonstrated few designs of energy harvesters, but they were not optimal for variety of situations. The objective of this article is to report a newly developed plate type model of vibration-based energy harvesters which can be used to harvest power from the ambient vibrations during various stages of flight. The generated power can be used to run the nondestructive SHM sensors used in the wireless sensor network. Nondestructive Inspection (NDI) uses sensors which require approximately 600 microwatts to get actuated by generating ultrasonic wave once. Research and inspection show that the optimum operating range for an energy harvester during flight is 800-1200Hz. Keeping that in mind a new plate type energy harvester has been envisioned which operates in the optimum frequency range and harvests enough energy to power the SHM sensors during flight. Such harvester minimizes the necessity of conventional batteries and thus opens a new door toward the 21st century's green energy

solution. The energy harvesters reported here aims to improve the efficiency and stability of the previously reported harvesters. This article reveals various stages of development of the energy harvester plate with a detailed numerical investigation of the developed model using COMSOL Multiphysics software to investigate the functionality and power output of the modified model, test the presented model and optimize the power output. An experimental validation of the presented model is also performed. The numerical study shows that the best model configuration, under certain loading condition, is capable of harvesting maximum ~4.67mW of power under 10kΩ resistive load.

The device presented in this report discloses an energy harvester that is capable of harvesting energy from low frequency and small magnitude vibration. This harvester uses a flexible piezoelectric material on a flexible membrane which is excited using a resonator disc. Mechanical vibration is converted to electrical output by applying strain on the piezoelectric material. This device can be placed in places exposed to vibration so that the piezoelectric material is strained to generate voltage. To make the model feasible to use in minimal space, a very thin and light design is envisioned. The materials used for this purpose are also lighter in density. In this article, two configurations of the plate are studied: 1) single membrane model where the piezoelectric material and the resonator is attached on top of the membrane and 2) double membrane model where the resonator is sandwiched in between the two membranes and piezoelectric material is attached to both the membranes.

5.1 Selection of the Best Energy Harvesting Atmosphere

The process of structural health monitoring in airplanes have two phases. 1. On-board phase where a portable power source is required for powering the sensors and 2. Off board

phase where AC power source is available. Both the phases are equally important. During the on-board phase, the remote sensors process inspection data and signal automatically, providing a detailed health report of the aircraft. An alternative powering device for supplying power to the onboard SHM sensors is a necessity for future smart aircraft. Harvesting energy from ambient sources inside the aircraft during flight can be a solution to the powering device problem. There are various parts and joints of the aircraft such as wing, loading gear, engine sources, radar, main cabin walls etc. which undergo a higher amount of vibration during the operational mode compared to other parts. If energy harvesting devices are placed in these high vibrating parts, then these can harvest energy enough to power the SHM devices. The energy harvesting devices reported so far are not capable of fitting inside the airplane. Minimizing the size and weight of the harvester to fit in the body of the airplane can help in harvesting the required energy. In order to do that, first, the power requirement of the NDI sensors available in the market needs to be surveyed. Table 5.1 displays the power requirement of a few popular ultrasonic transducers for SHM available in the market currently.

Table 5. 1: Power requirements of common commercial energy harvesters

Company Name	Power required	Frequency range	Type
GE electronics	99.12Wh	4 MHz	Ultrasonic transducer
Ge electronics	28.86Wh	4 MHz	Ultrasonic flaw detector
Olympus	73Wh	5 MHz	Ultrasonic flaw detector
NDT systems	20.4Wh	4 MHz	Ultrasonic transducer
Zetec	71.2Wh	5 MHz	Ultrasonic transducer

Keeping this in mind, an energy harvester needs to be designed which can use the ambient vibration of the aircraft during the flight to harvest power. Few challenges that lie ahead of the design are to locate the zones of the aircraft during various stages of a flight where the maximum amount of displacement takes place. Simultaneously, an optimum frequency range needs to be finalized for harvesting maximum energy possible. The size and weight of the harvester must be small enough to be placed inside the aircraft without bothering the usual workflow.

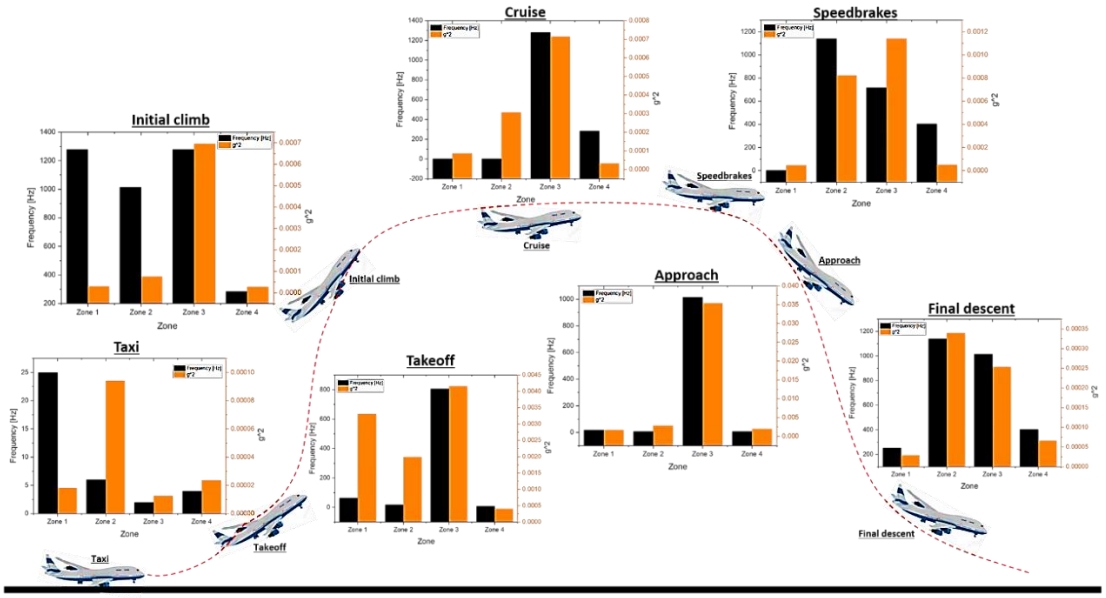

Figure 5. 1: possible energy harvesting frequency and amplitude during different stages of a flight

The entire flight time of an airplane can be divided into seven major stages such as taxi, takeoff, initial climb, cruise, speed brake, approach, and final descent (Figure 5.1). Certain research and investigation records show that the aircraft experiences a significant amount of vibration during these stages. Collected data have been analyzed at four different zones namely Radar Base, Forward Cabin Fuselage Frame, Forward Cargo Bay Rear

Bulkhead and Aft Cargo Bay Rear Bulkhead. The analysis confirms that these zones have enough displacement amplitude required to harvest energy. If energy harvesting devices are placed in these zones, they can harvest energy from the ambient vibration. Success in placing the energy harvesters ensures that the wireless sensor networks become self-sufficient. So, the in-situ power generation for the sensors can be ensured during flight.

5.2 Design Philosophy

A cantilever beam with piezoelectric materials attached to it is the most common form of vibration-based energy harvester. Most cantilever beam based energy harvesters are considered as single degree of freedom (SDOF) oscillator since most of the energy is carried by lowest harmonic vibration of the structure[151]. Although energy harvesters in the form of cantilever has many drawbacks, still it has high power output in lower amplitudes because of their high strain. The energy harvesting devices that have been reported earlier has satisfactory power output in a lower frequency range. The frequency range that is being considered for in flight energy harvesting needs an optimized cell design which can fulfill all the criteria. The main component for power harvesting is the piezoelectric material. To improve power output and optimize frequency range, various designs and forms of piezoelectric materials were investigated. In addition to PZT-5H, PVDF film has also been considered as a piezoelectric material. These cells are required to be installed inside the airplane, since the power is harvested using the ambient vibration during flight. So, the cell should be light and small. Keeping this in mind, a new form of design was developed aiming to decrease the size of the unit cell by keeping the power output and frequency range at the required level.

5.3 Design development

At the very beginning, a thin form of energy harvester is envisioned. To introduce multimodal and multi-frequency energy harvesting, a unit cell in spiral form was designed. Here thin rubber matrix was installed inside a grooved metal plate of 25mmX25mm dimension. The cell had a total thickness of 2mm. The matrix encapsulated the piezoelectric material and the resonator. For this cell, instead of the spherical resonator, a thin metal disc was used as a resonator. PVDF cylinder encircled around the disc resonator was employed as the piezoelectric material. The specialty of this cell was that the matrix, resonator and the PVDF cylinder was organized in a spiral pattern where their diameters gradually increased along the spiral. But the power output from this model turned out to be very low at the desired frequency range. Then again, another thin form of unit cell was designed. Here a unit cell with silicone membrane attached in between two PVC frames was considered. In this model, a disc of PZT was considered as both resonator and piezoelectric material. The frame has a dimension of 20mmX20mm and the total thickness of the frame is 4mm. But the resonance frequency and power output from this cell are not promising. Previous study shows that PVDF has higher efficiency compared to PZT. So, for the next modification, PVDF film is considered as the piezoelectric material. So, in the modified model, a ring of PVDF film as piezoelectric material and steel disc as resonator has been used.

Now, a thin plate type energy harvester is envisioned where the unit cell consists of a comparatively heavy metal core resonator, a very thin membrane, and a piezoelectric material. The flexible membrane is strongly attached in between two lightweight frames. The flexible membrane holds the resonator and the piezoelectric material. The resonator

and piezoelectric material are glued with the membrane firmly. The unit cell of the proposed model has PVC frame. The frame consists of two symmetrical parts. These two pieces of frames hold a thin silicon membrane in between them. There is a ring of PVDF film and a small disc of steel with which acts as the resonator for the cell. The material properties of the cell's constituents are given in table 5.1 The properties of PVDF film can be found from equation (5.1-5.3).

Table 5. 2: Material properties of the cell constituents

Material	**Density**	**Young's modulus**	**Poisson's ratio**
PVC	1420	$25X10^6$	0.40
Silicon membrane	1130	$8.896X10^6$	0.48
Steel	7850	$205X10^9$	0.28

PVDF Compliance Matrix:

$$S = \begin{bmatrix} 4.06 & -5.09 & -10.12 & 0 & 0 & 0 \\ -5.09 & 2.20 & -8.75 & 0 & 0 & 0 \\ -10.12 & -8.75 & 15.28 & 0 & 0 & 0 \\ 0 & 0 & 0 & 1.82 & 0 & 0 \\ 0 & 0 & 0 & 0 & 1.69 & 0 \\ 0 & 0 & 0 & 0 & 0 & 1.43 \end{bmatrix} \times 10^{-12}\, Pa^{-1} \ldots\ldots\ldots\ldots\ldots \textit{Eq. 5. 1}$$

PVDF Piezoelectric charge constants or the coupling matrix:

$$d = \begin{bmatrix} 0 & 0 & 0 & 0 & -0.137 & 0 \\ 0 & 0 & 0 & -0.126 & 0 & 0 \\ -0.93 & -0.67 & 2.8 & 0 & 0 & 0 \end{bmatrix} \times 10^{-12} C/N \ldots\ldots\ldots\ldots\ldots\ldots \textit{Eq. 5. 2}$$

PVDF Relative permittivity matrix:

$$\varepsilon = \begin{bmatrix} 12 & 0 & 0 \\ 0 & 12 & 0 \\ 0 & 0 & 12 \end{bmatrix} \ldots\ldots\ldots\ldots\ldots\ldots\ldots\ldots\ldots\ldots\ldots\ldots\ldots\ldots\ldots\ldots\ldots\ldots\ldots\ldots \text{Eq. 5. 3}$$

The inner diameter of the frame can be changed with the requirements of the harvested energy or the frequency. Trial and error process helped to conclude that there is a relation

between the frame diameter and the stiffness ratio. Considering a (20X20) mm unit cell with a PVDF ring with fixed diameter and changing the inner frame diameter the result output can be seen from table 5.3.

Table 5. 3: Change in resonance frequency and power output based on the frame diameter

Frame dia. (mm)	Power (μW)	Resonance frequency (Hz)
9.75	1.24	840
9.5	24.7198	900
9.25	41.58	1190

So, the relation between the resonator dia. and frame dia. can be explained by the following relations:

$$\frac{resonator\ dia.}{frame\ dia.} = higher \rightarrow \text{Higher power output and resonance frequency}$$

$$\frac{resonator\ dia.}{frame\ dia.} = lower \rightarrow \text{Lower power output and resonance frequency}$$

Now the PVDF ring needs to be placed in such a way and position where the maximum amount of displacement takes place. An eigenfrequency analysis has been performed on COMSOL for this model to find out the optimum place to place the piezoelectric material.

5.4 Position of the piezoelectric material

Each local resonance mode captures the dynamic wave energy in the membrane in unique ways inside the cell. Hence, it is expected that proper placement of a piezoelectric material, can provide a significant electric potential at the local resonance frequencies. Figure 5.2

represents the existence of multiple local resonance modes within the 1200Hz frequency limit. Unique piezoelectric material placement is essential to harvest energy from each of these modes.

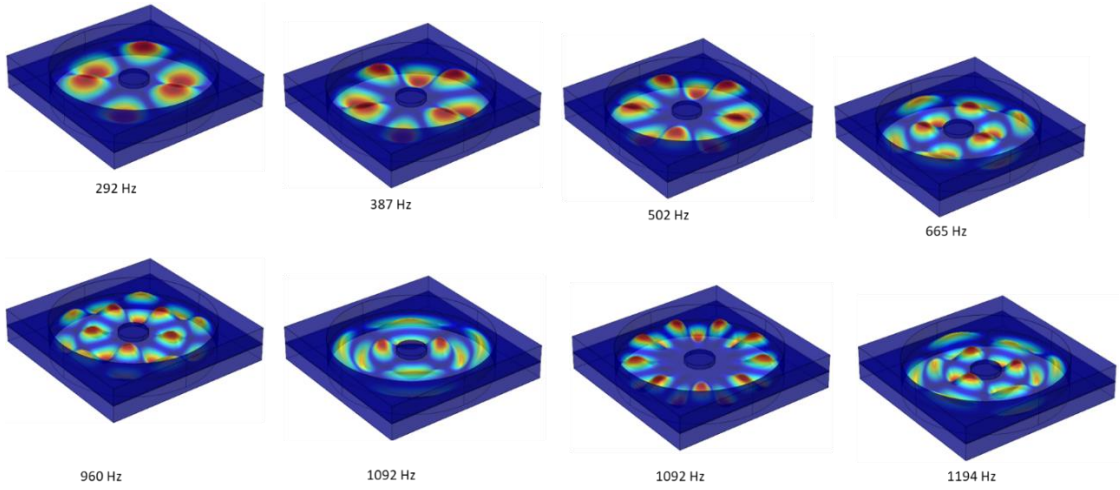

Figure 5. 2: Displacement patterns and location in the unit cell at various frequencies.

The PVDF membrane that is intended to be used in this design will be able to harvest maximum amount of energy if placed in the form of a ring. This design is chosen based on the local resonance modes generated inside the structure. Figure 5.2**Figure 5. *2*:**Displacement patterns and location in the unit cell at various frequencies. shows the places where the highest amount of displacement takes place at various frequencies, including the resonance frequencies. The PVDF ring has to be placed at the certain band where these phenomena are observed at its maximum. It can be seen that the maximum deformation is observed around the resonator in a circular ring form. So, with such PVDF film arrangement in ring form, it is possible to scavenge maximum amount of power from the plate model with unit excitation. Output power from the unit cell can be improved by optimizing geometrical and material configuration in the unit cell.

5.5 Development of Single Membrane Plate Model

5.5.1 Analytical Study of the Single Membrane Model

The final design for the unit cell of the plate uses PVDF film as a piezoelectric material and a steel disc works as the resonator. The piezoelectric material and the resonator are attached on top of a silicone membrane. The membrane is encapsulated in between two thin PVC frames. The dimension of each of these frames is (20mmX20mmX2mm). Considering the relation between the resonator dia. and frame dia. the internal radius of the frame is chosen to be 9.25mm. The thickness of the PVDF ring is 2mm with outer and inner radius to be 6mm and 4 mm respectively. The resonator has a radius of 1.7mm. 21 of these unit cells create a plate in a 3X7 matrix form. The unit cell and the plate model are shown in Figure 5.3. The piezoelectric materials in the plate are connected in parallel to harvest the maximum amount of power possible. These individual plates can be stacked together in different patterns to generate higher amount of power. The boundary condition of these structures also affects the output power.

Since, in a natural situation, vibration comes with a mixture of multiple frequencies, excitation frequency and mode of vibration can also vary based on excitation medium, placement of the harvesting device etc. Hence, it is always suggested to have as much local resonance modes as possible to have the opportunity to harvest energy in multiple frequencies and modes. For harvesting energy at various modes, specific piezoelectric material placement and loading condition is essential. It has been noticed that at a specific loading condition, rest of the local resonance modes disappear. So, it is essential to find ways to introduce additional local resonance modes and energy harvesting in multiple

frequencies, in addition to power optimization at each mode. Hence, several investigations were made to improve the energy harvesting capacity from the plate model.

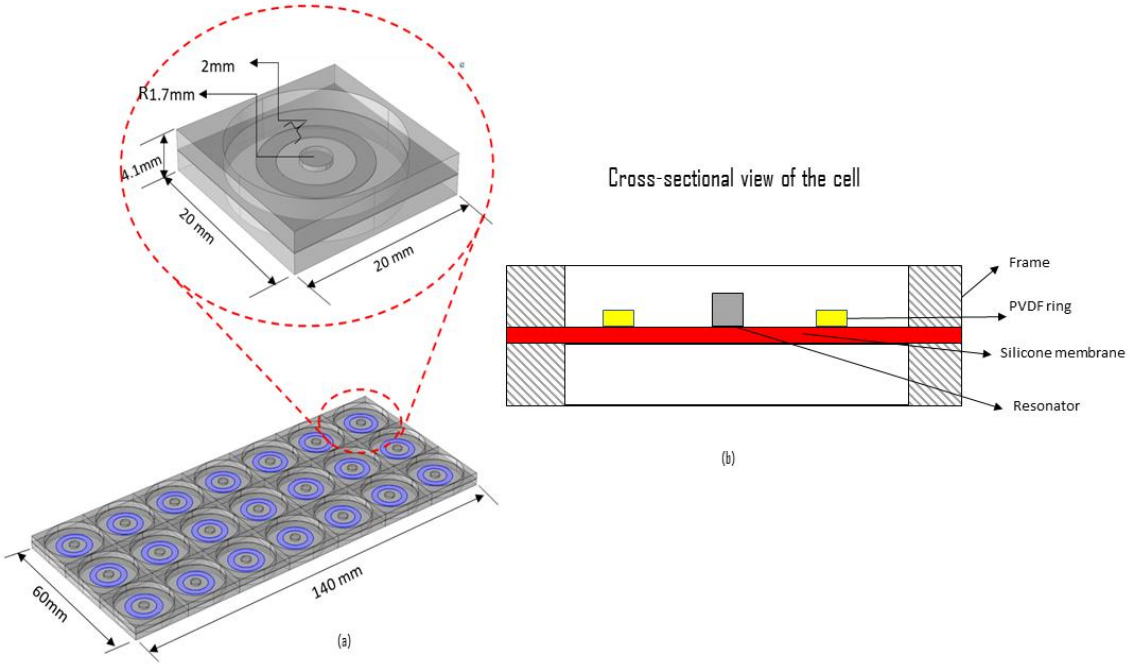

Figure 5. 3: (a) configuration of the energy harvesting plate (unit cell in inset) (b) cross sectional view of the unit cell

For the single membrane plate that is analyzed, two configurations were considered. They are free plate and cantilever plate (**Figure 5. *4*:** (a) free plate (b) stack of normal plate (c) cantilever plate (d) stack of the cantilever plateFigure 5.4). The free form does not have any constraints, i.e. has free-free boundary condition (Ref. figure5.4a). The other one is the cantilever form, which has one of its ends fixed and another end free (Ref. Figure 5.4c). These plates can be stacked together in both normal and cantilever form. Both the configuration can be seen in Figure 5.4b and d. A significant amount of space is left in between the layers while stacking the plates to accommodate enough space for deformation of the membrane. This space in between the layers also ensures that the plates vibrate freely without touching each other and interrupting the power generation process. 10 KΩ resistive

load is considered in measuring the power output in this analysis. There is a relation between power, voltage, resistance and current flow which will provide the accurate battery charging time required using these plates.

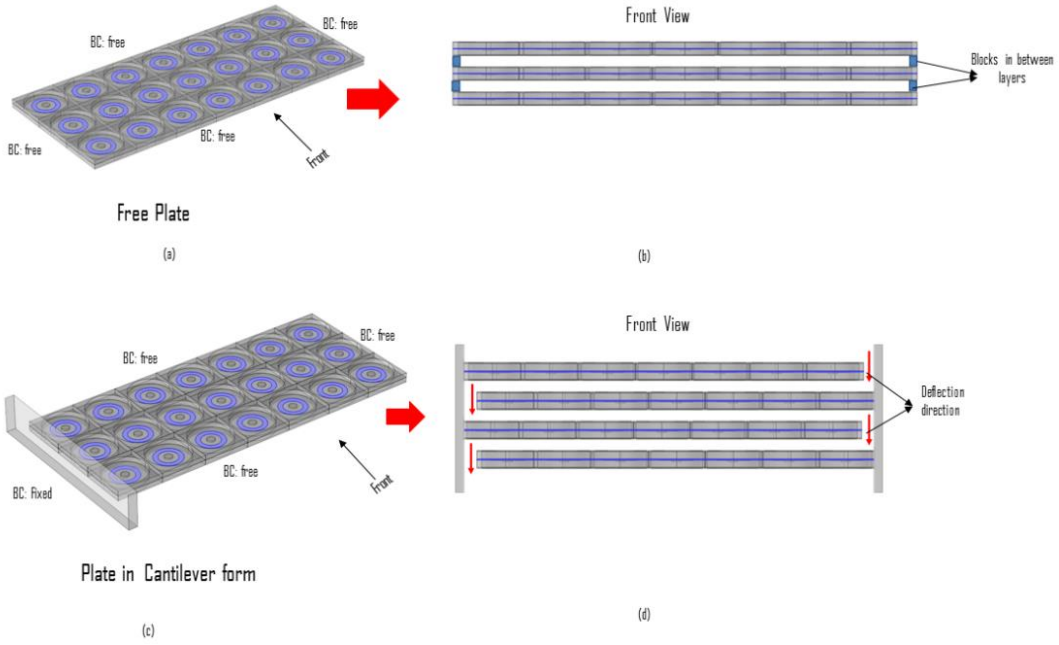

Figure 5. 4: (a) free plate (b) stack of normal plate (c) cantilever plate (d) stack of the cantilever plate

A numerical investigation has been completed on the proposed plate models using COMSOL Multiphysics. At first, 1mm excitation was provided to the plate. Both the normal and cantilever forms were considered. The optimum frequency range (800-1200Hz) was used as the excitation frequency range. The resulting output shows that both the models are capable of harvesting power within that range. More than one peak can be observed for both the cases. One interesting fact that comes into light after analysis is that the output power is much higher for the cantilever form of the plate compared to the normal plate when exposed to the same amount of displacement. Apparently, the output power is almost double for the cantilever plate than that of the normal plate. But the resonance frequencies

for both the cases remain similar. But in practical field, it is not possible to generate 1mm excitation amplitude in such high frequency range.

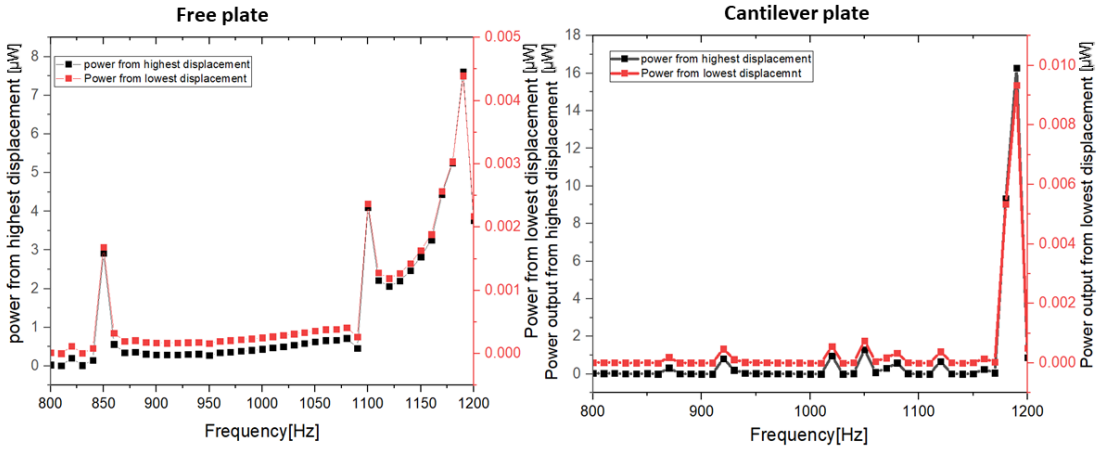

Figure 5. 5: Power output from a single plate with highest and lowest displacement amplitude (a) free plate and (b) cantilever plate

According to the data collected from an investigation operated during flight, it can be found that the maximum amount of displacement that takes place due to ambient vibrations is 0.0004278m. The lowest amount of displacement was recorded to be 1.02381e-05 m. These values have been used for the proposed model to verify its feasibility for various amount of vibration. These displacement amplitudes were applied on both the free and cantilever form of the plate. For the free plate, the maximum amount of power generated from the highest and lowest amount of displacement is found to be 7.612081µW and 4.40E-03µW respectively. Again, for the cantilever plate, the maximum and minimum amount of power generated from the highest and lowest amount of displacement was found to be 16.28µW and 9.33E-03µW. It can be seen that no matter what amount of vibration is applied to the plate, cantilever form always gives a higher amount of power output compared to the free plate. The resulting output can be seen from figure 5.5. COMSOL

Multiphysics software was used to run these simulations. If the plates can be stacked as shown in Figure 5.4, the power output can be maximized.

5.5.2. Experimental validation of the single membrane model

The concept of harvesting energy from the plate type model is experimentally validated. An experimental investigation has been performed for the energy harvesting plate model by fabricating a full-scale model of the proposed single membrane plate type energy harvester in the laboratory.

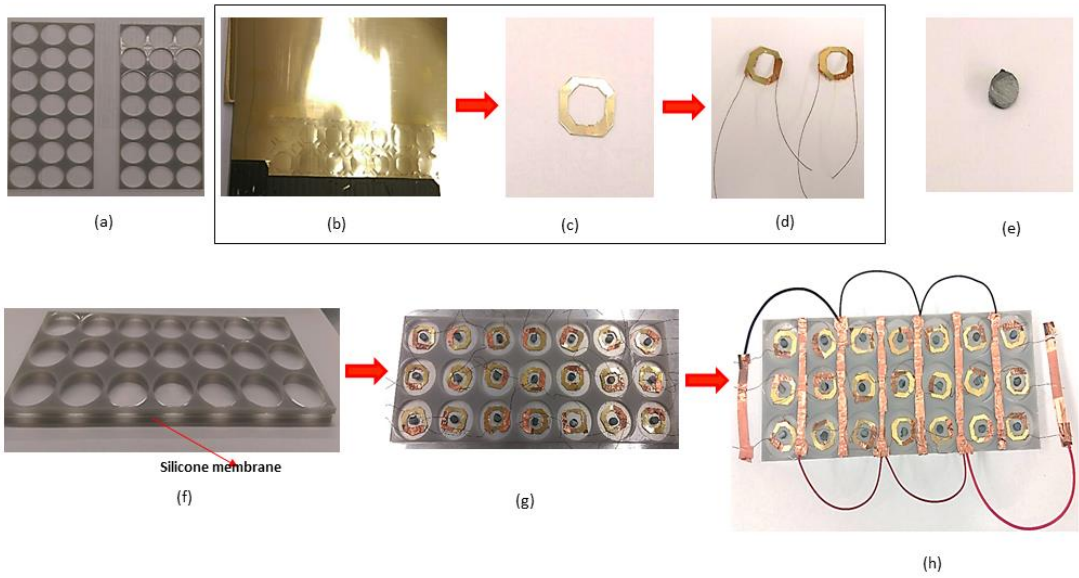

Figure 5. 6: (a) 3D printed frames; (b) Golded PVDF film; (c) PVDF ring; (d) PVDF sensors; (e) steel resonator; (f) silicone membrane attached in between the frames; (g) sensors and *resonators placed on the membrane using M-bond; (h) connections made using copper tape and wire.*

The fabrication steps are discussed as follows. First, the PVC frames are fabricated using 3D printing technique. A golded PVDF sheet of 110μm thickness from Precision Acoustics is used for the PVDF ring. The piezoelectric sensors and the resonators are attached to the silicone membrane using M-bond. Copper wire and tape is used to connect

the sensors in parallel connection. The entire model building process can be seen from Figure 5.6. A customized 3D acousto-vibration test bed is used to perform the experiments. Signal generator is used to generate frequency between 800-1200Hz. This signal passes through the power amplifier which has impedance of 50Ω with amplification rate of 10. This signal passes through a custom-made signal conditioner which eventually transfers the vibration to the shaker attached inside the acousto-vibration test bed. The shaker is used to vibrate the plate model. The output signal from the plate can be recorded from the oscilloscope. A flow chart of the entire process can be seen below. Figure 5.7 represents the entire experimental setup.

From the numerical study, the highest power output from the plate is found to be ~7.61μW at around 1190Hz frequency. From the experimental result, it can be seen that the power output follows the same pattern of the numerical model, but the total power output is lower compared to the simulated value. A normalized plot of the experimental power output is presented in figure 5.8. The resonance frequency is recorded at ~1195Hz. Two other significant peaks can be found at ~815Hz and ~1050Hz. From the experimental results, it can be seen that both the numerical and analytical models support the fact that maximum power from this model can be harvested around ~1190Hz. This experimental model also verifies that this plate type model is capable of harvesting energy under constant vibration. The shifts in the peak frequencies and power output is the outcome of many factors combined but mainly due to fabrication error.

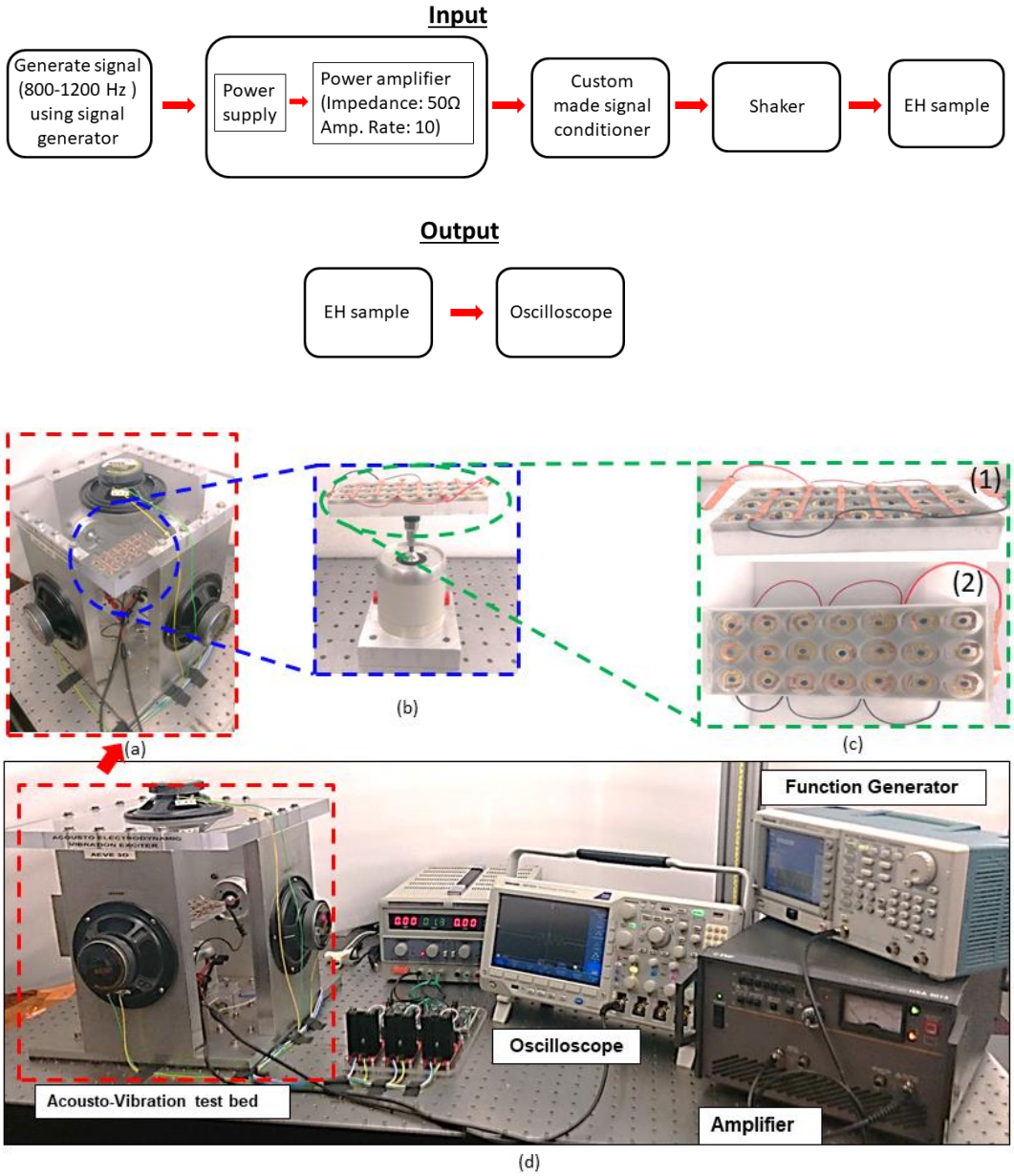

Figure 5. 7: Experimental setup for the plate model (a) EH plate placed inside the acousto-vibration test bed; (b) zoomed view of the plate attached to the shaker; (c) top and side view of the plate; (d) entire experimental setup.

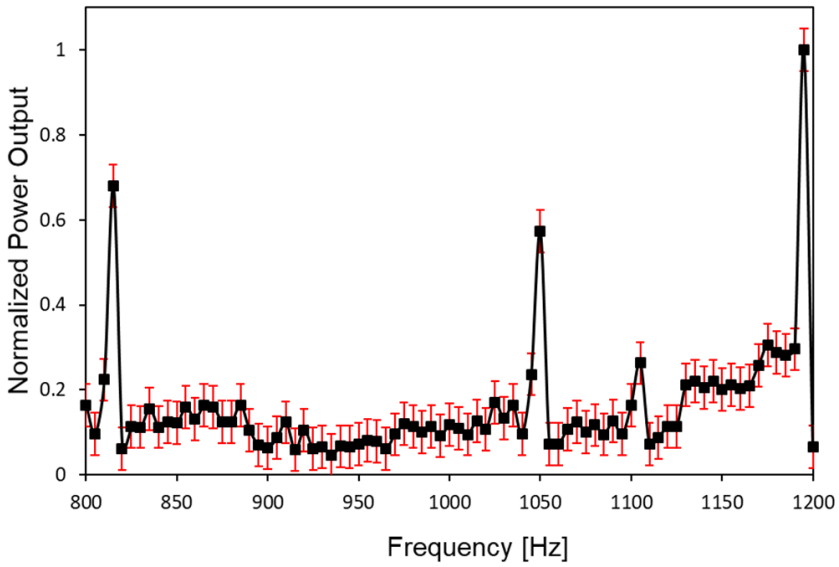

Figure 5. 8: Normalized experimental power output from the plate model

5.6 Development of the double membrane plate

In the previous section, a single membrane plate-type model has been proposed which can produce power from vibration. This design has been modified keeping the dimensions and the optimum frequency range similar in order to improve power output and make the design free of defects. The previous design had the PVDF film and the resonator attached on top of the membrane. This poses a risk of the resonator to displace or detach from the membrane during the operational phase of the cell due to constant vibration. It is essential that the resonator stays in place throughout the operational phase for the proper functionality of the harvester. So, the modified design that is proposed in this report has two layers of the silicone membrane. In order to be assured that the resonator is always secured, in this model, it is sandwiched in between the two layers of membrane. Since there are two layers of membrane, PVDF ring can be attached on both membranes. This ultimately results in higher power output. With the aim of keeping the membranes distinct

and stable, support is added in between the layers. Initially, four small blocks made of PVC are placed at each corner of the unit cell. These blocks add stability to the cell and also guarantee that the resonator stays at its place.

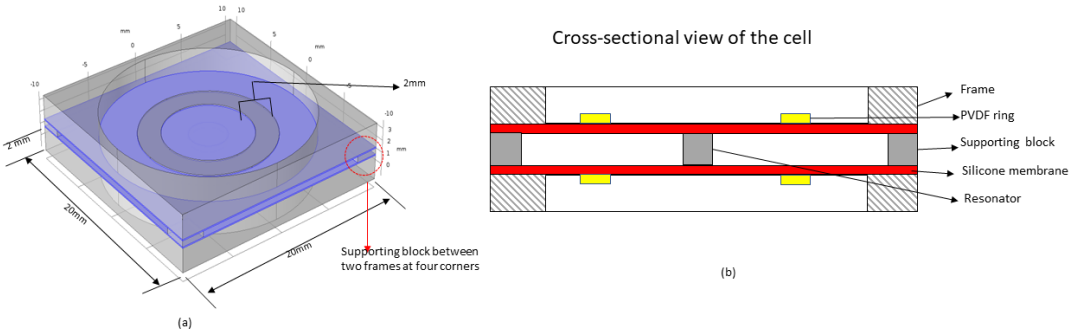

Figure 5. 9: modified design of the energy harvester (a) 3D view of the unit cell (b) cross-sectional view

In the modified model, the dimension of the frame of a unit cell is (20mmX20mmX2mm). The internal radius of the frame is 9.25mm. Piezoelectric film (PVDF) is attached to the membrane in the form of a ring. Ring thickness of the PVDF is 2mm with outer and inner radius to be 6mm and 4 mm respectively. The thickness of the PVDF film itself is 100μm. The resonator which is encapsulated in between the membrane is of 1.7mm radius. The silicone membrane in each cell has a dimension of (20mmX20mmX0.1mm). 21 of such unit cells are combined to create an energy harvesting plate in a 3X7 matrix form. 3D view of the unit cell of modified double-membrane design can be visualized in Figure 5.9 (a). Figure 5.9 (b) shows the cross-sectional view of the unit cell. The piezoelectric materials in the plate are connected in parallel to harvest the maximum amount of power possible. This model is developed in COMSOL Multiphysics software and a numerical investigation has been done. Since the optimum frequency range is well-thought-out to be 800-1200 Hz, it is kept the same for all the model simulations.

The energy harvesting plate is considered to be in cantilever form for all the cases. Material properties of the cell constituents can be found in table 5.1.

One of the main reasons for modification of this design is to ensure the stability of the cell constituents under various operating conditions. For this purpose, the corner supports are also modified. Here three configurations of the support in between layers is considered. At first, the membranes are supported by four supports at four corners(Figure 5.10a). Each block at the corner measures (2mmX2mmX0.5mm). This allows the waves to oscillate without barrier and avoid the bouncing back of the waves and creation of antiresonance. Then the supports are extended to both the sides entirely such that both sides are fully supported (Figure 5.10b). Here each supporting block is of size (20mmX2mmX0.5mm). In this form, the cell gains higher stability since the entire side is supported. In here, the other two sides remain open creating a cavity. In a further step of modification, the support is extended on all four sides of the membranes (Figure 5.10c). The width and thickness of the support are 2mm and 0.5mm respectively. This design ensures the maximum stability of the cell constituents. As there is support on all four sides, the mode shapes are uniform as there is no cavity anywhere.

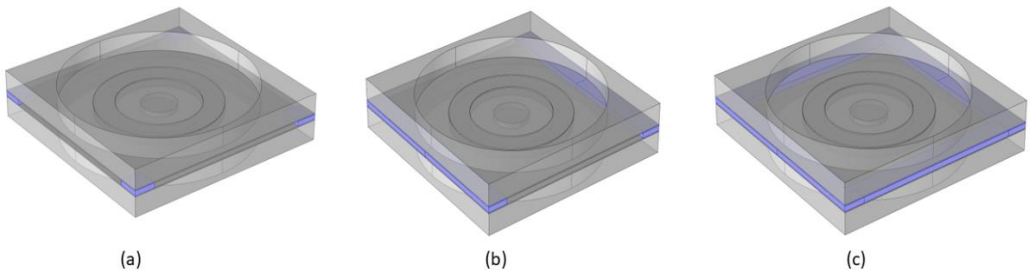

Figure 5. 10: 3D view of the unit cells of the double membrane design (a) corner support (b) 2 side support (c) all side support

In the design proposed earlier, placement of the piezoelectric material is based on the band where the resonance frequencies observe the most deformation in the membranes. The double membrane design has similar cell specifications, but still it needs to be checked whether the new cells exhibit similar deformation in similar places. For this reason, an eigenfrequency analysis is performed in COMSOL for the modified models to observe the mode shapes at various resonance frequencies of different design modifications (Figure 5.11).

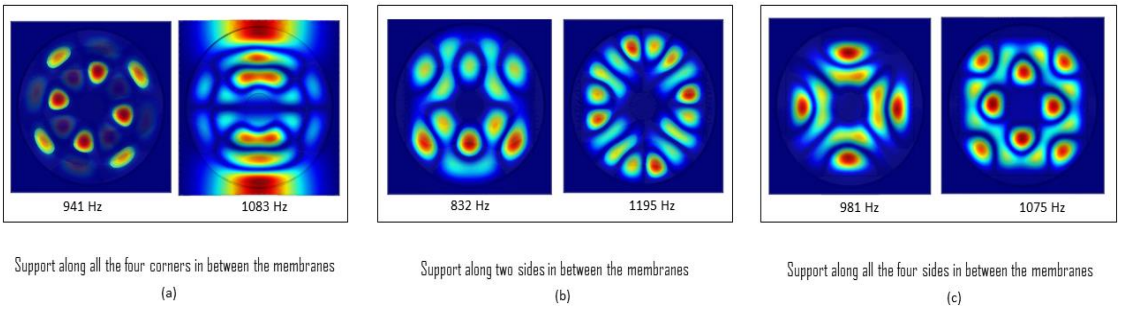

Figure 5. 11: Displacement pattern of different models in resonance frequencies in unit cells (a) corner support (b) 2 side support (c) all side support

It can be seen that all the modified designs also exhibit maximum deformation around the area where the PVDF is placed. So, the PVDF placed on top of the membrane in the form of a ring should be able to harvest the maximum amount of energy from its position.

5.6.1 Double membrane under different loading condition

In this section, the capability of harvesting electrical energy from mechanical vibrations under dynamic conditions using the double membrane plate type model is investigated. Our targeted vibration lies in the range of 800-1200Hz. Behaviors of a beam such as displacement or deformation pattern can change based on the loading condition.

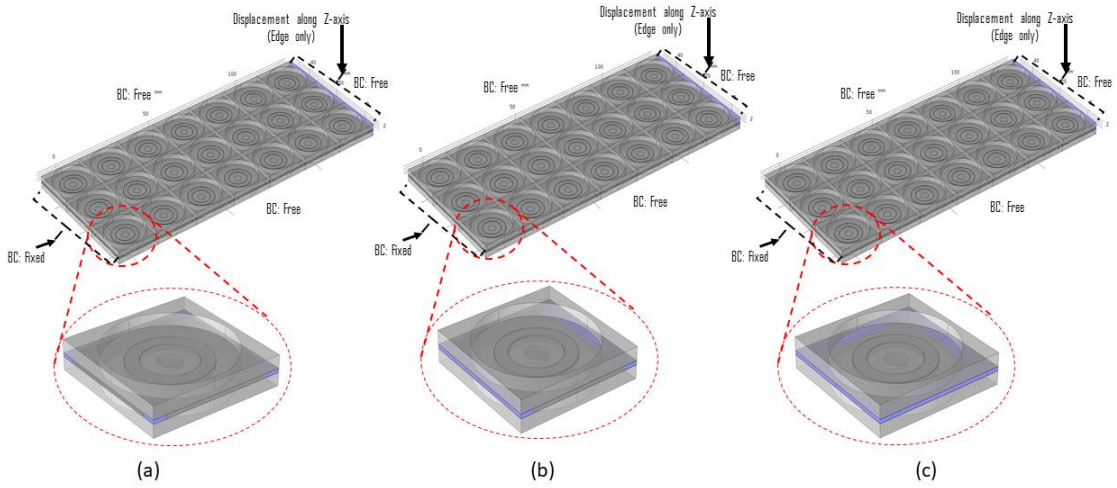

Figure 5. 12: Displacement along z-axis on the edge (a) corner support (b) 2 side support (c) all side support

In the preliminary stage of the study, 0.1mm displacement-based excitation along the z-axis is applied to the free end of the cantilever plate. A similar study is done on all 3 configurations of modified cells (Figure 5.12).

In a natural environment, it is not certain that the plate goes through the edge or point excitation each time. To check the functionality of the cell under different loading conditions, few more tests were done. This time the plate is exposed to uniformly distributed displacement amplitude of 0.1mm in entire top surface. The 3 configurations of cells are compared side by side under various loading conditions (Figure 5.13).

Again, since the design is in the form of a cantilever beam, it is also possible that the vibration is generated in the body along the fixed edge of the plate. To visualize the phenomena and power output from such condition, simulations are done where the fixed end undergoes vibration in the frequency range of 800-1200Hz where the displacement of 0.1mm is provided in the base of the host structure and the vibration pattern and power output are observed (Figure 5.14).

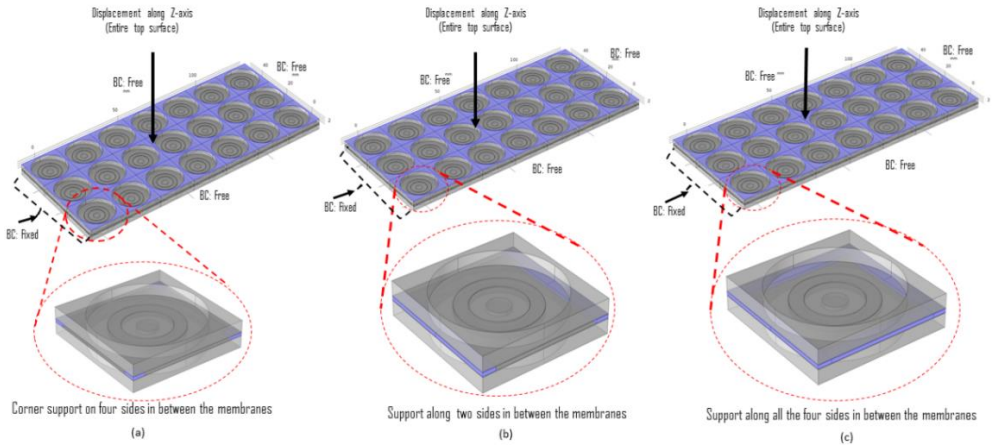

Figure 5. 13: Displacement along z-axis on the entire top surface (a) corner support (b) 2 side support (c) all side support

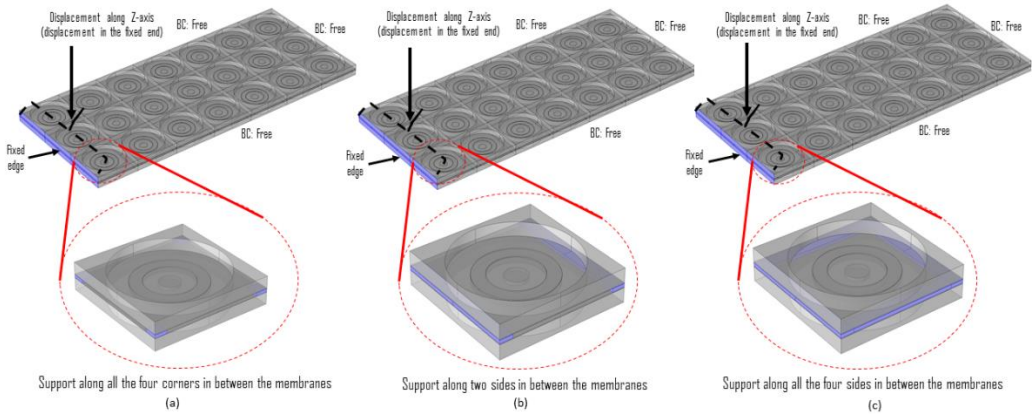

Figure 5. 14 Displacement along z-axis on the fixed end (a) corner support (b) 2 side support (c) all side support

5.6.2 Results and discussion from dynamic displacement conditions

A numerical investigation has been done on the double membrane plate models using COMSOL Multiphysics. At first, free edge displacement of the plate with corner support cell design indicates that this plate is capable of harvesting ~1.6μW of power from such vibration. The resonance frequency is found to be around 900Hz which is in the lower frequency range. There are other peaks visible nearby also, which can be another

prospective frequency for energy harvesting though they don't give promising power output (fig-5.15a). For the double-sided support cell, the power output from the entire plate reaches ~7.36μW but there are no other peaks visible so the possibility of power output from other frequencies apart from the resonance frequency is nearly nil (fig-5.15b). Finally, for the all-sided support model, multiple peaks can be visualized. But the ultimate power output from this type of cell is low (fig-5.15c). So, for the edge displacement model, the best design is the one with double-sided support based on the power output. Now, this plate needs to be checked under other conditions to observe the power output pattern.

For the second case, the cells are checked under the distributed displacement mode. In this case also, 0.1mm displacement is applied to the entire top surface of the plate. In this condition, the plate with corner support shows ~4.673mW of power output at around 1000Hz resonance frequency from the entire plate (fig-5.16a). This design also shows similar peaks around other frequencies within the targeted frequency range.

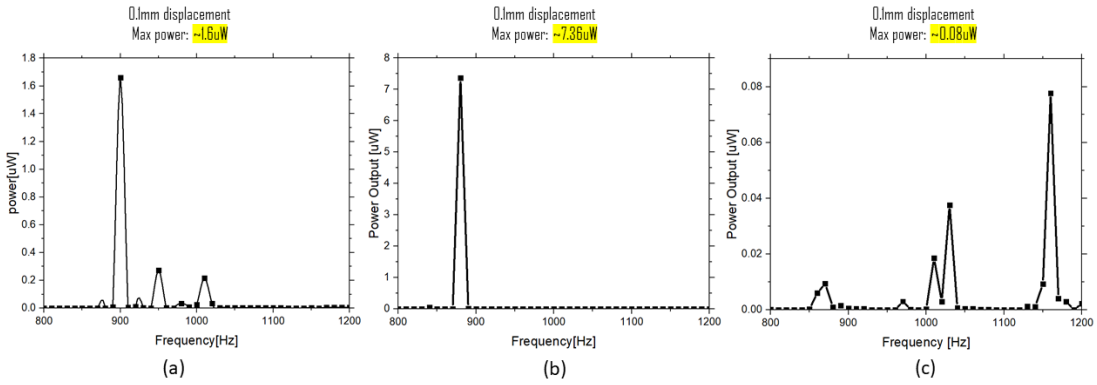

Figure 5. 15: power output from free edge displacement (a) corner support (b) 2 side support (c) all side support

Though the resonance frequency, in this case, is around 1200Hz it also has a peak at a lower frequency which is similar to the peak at the resonant frequency (fig-5.16b).

Now, for the all-sided support model, the resonance frequency comes down to ~970Hz and the output power reaches 22.57μW (fig-5.16c). There is another peak visible at a little lower frequency. So, for the case of distributed displacement, it can be seen that the best model is the one with the corner support based on the power output and the resonance frequencies.

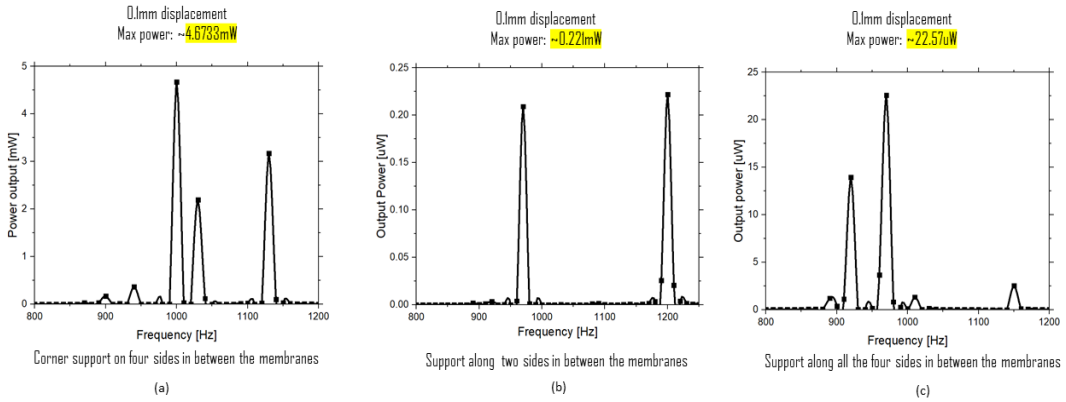

Figure 5. 16: Power output from distributed displacement (a) corner support (b) 2 side support (c) all side support

Finally, the model is tested under the base vibration condition. In this case, the base along the fixed edge is set under the vibration mode with 0.1mm displacement amplitude and the entire plate vibrates due to the vibration of the base. For this case, the corner support design has a power output of ~8.73μW at a frequency of around ~930Hz (fig-5.17a). For the double-sided support model, the power output and the resonance both decreases. The power output reaches 0.44μW and the resonance frequency reaches 830Hz (fig-5.17b). Among all the studies done, it is the lowest frequency in which this model is capable of harvesting energy. Now for the all-sided support model, the power output reaches ~26.33μW at a frequency of 1090Hz which is the highest for the all-sided design under various conditions (fig-5.17c). Based on power output the best model for the base vibration case is the cell design with four-sided support.

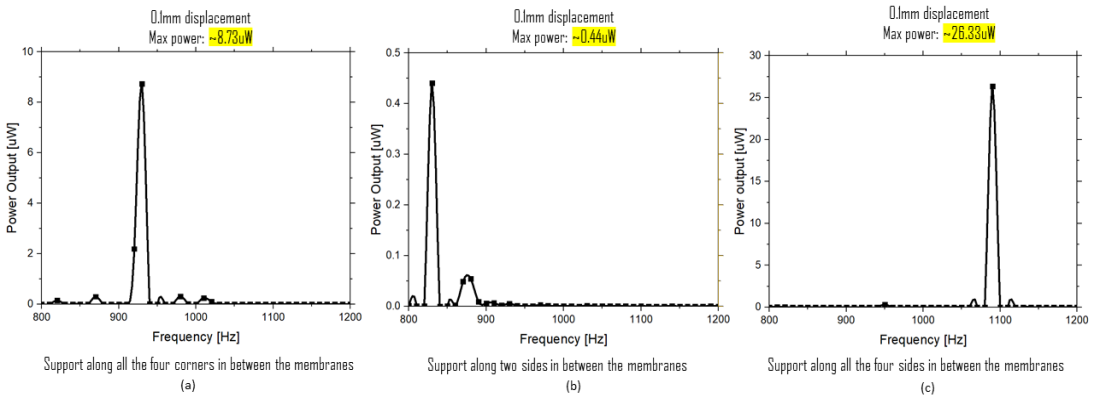

Figure 5. 17: Power output from base vibration (a) corner support (b) 2 side support (c) all side support

So far, we have studied two types of cell design of the plate type energy harvester. The design proposed first has a single membrane and the studies that have been reported later is done considering the double membrane model. A comparison between the power output, resonance frequency for single and double-membrane model under various loading configurations in the form of cantilever plate is presented in table 5.4.

Table 5. 4: Comparison between different membrane type models developed so far

Models	**Resonance Frequency [Hz]**	**Power output (uW)**
Single membrane with PZT 5H	100	40
Single membrane with PVDF ring	1190	41.58
Free-free single membrane plate	1190	7.61
Cantilever single membrane plate	1190	16.28
Double membrane with corner support (distributed Load)	1000	4670
Double membrane with 2 side support (distributed Load)	1200	221
Double membrane with all side support (distributed Load)	970	22.57
Double membrane with corner support (fixed end displacement)	930	8.37
Double membrane with 2 side support (fixed end displacement)	830	0.44
Double membrane with all side support (fixed end displacement)	1090	26.33

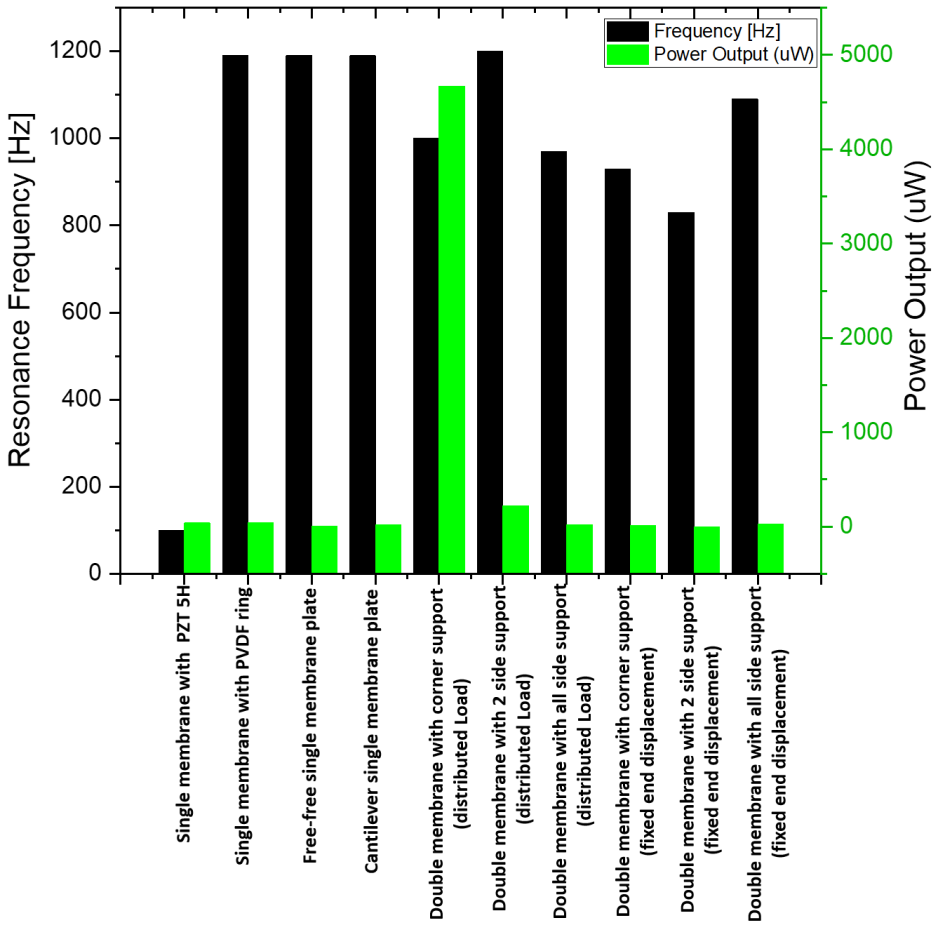

Figure 5. 18: Comparison between the resonance frequency and the power output of plate type models

A comparative chart is also presented in Figure 5.18. Comparing this double membrane model with the single membrane model, it can be seen that the double-membrane model works better than the single membrane model in many aspects. This model has been tested in various loading conditions and has displayed promising performance under all circumstances. Figure 5.18 represents the comparison between the models. It can be seen that most of the models have comparatively lower power output and higher resonance frequency. The design with double membrane and corner supports has the highest power output among all the models. Overall, the double membrane has proved to be better in all aspects.

CHAPTER 6

Performance of a Multifunctional Spiral Shaped Acoustic Metamaterial with Synchronized Low-Frequency Noise Filtering and Energy Harvesting Capability

6.1 Motivation

Environmental noise mitigation to ensure healthy surroundings is one of the leading topics in the field of acoustic research. Conventionally used noise barriers use the physics of sound absorption and reflection to minimize the level of sound on the other side of the barrier. These barriers block both noise and air flow. So advanced research is being carried out to invent noise barriers that aid airflow. Simultaneously, extensive research is also being carried out to control the acoustic fields within enclosed spaces. Damping a structure to minimize noise is a practical solution that is used typically to minimize high-frequency sound. But this approach is not always feasible for lower frequency range. In such cases, alternate solutions are required. Today noise level plays a major role in various market platforms. This has forced the industries to focus on designing precisely engineered products which has lower noise emission and meets the buyers criteria.t is required that while the size and weight is minimized, cost is also optimized.

Various methods can be employed to passively control the sound propagation. A few of the popular approaches include the use of engineered materials for sound barriers, optimal design of the barrier (height, pattern), using sound-absorbing structures, etc.

Common structures that can absorb sound include Helmholtz resonators. Helmholtz resonators (HR) are structures with a cavity and a narrow neck which can be utilized as sound-absorbing structures. Though HRs have proved to have the noise-absorbing capability, further research on this structure is still ongoing since various discordances have been reported. A diverse group of researchers has studied the effect of various HR properties and their effects on the acoustic field. Both analytically and experimentally these properties and their effects have been proved that they play an important role in controlling the sound wave. Yet there are few challenges faced in certain designs that contain the HRs.

The designs proposed so far have shown promising output in terms of noise blocking and energy harvesting both. But both of them have some shortcomings. The meta Wall is very efficient, has high strength, but it is very heavy because of the building materials used. Another downside is that it blocks airflow and line of sight. To minimize the weight, we slimmed down the design to a plate model which is slim and lightweight. But this model is not so efficient in terms of noise reduction. Similarly, the double membrane model has better efficiency in vibration-based energy harvesting compared to acoustic energy. So, a new model needs to be designed which solves all of the problems that we faced with the previous model. Keeping this in mind, a new design needs to be developed which embrace the advantages of the established models and also solves the problems associated with the existing designs.

6.2 Basic Study

Based on the motivation, in order to achieve our goal a very old sound-reducing structure Helmholtz Resonator is chosen as the initial design component. Initially, HRs of varying height are considered and studied to ensure that they are capable of filtering noise in our

desired frequency range. A very simple design of cylindrical Helmholtz resonator is chosen with PVDF film attached inside the cavity in the form of a trampoline to harvest energy. Initially 18 HRs with varying height starting from 50mm to 14.13mm are studies to visualize the sound filtering efficiency of the components. Figure 6.1 helps to visualize the Helmholtz resonator design and the transmission loss associated with the 18 resonators studied so far.

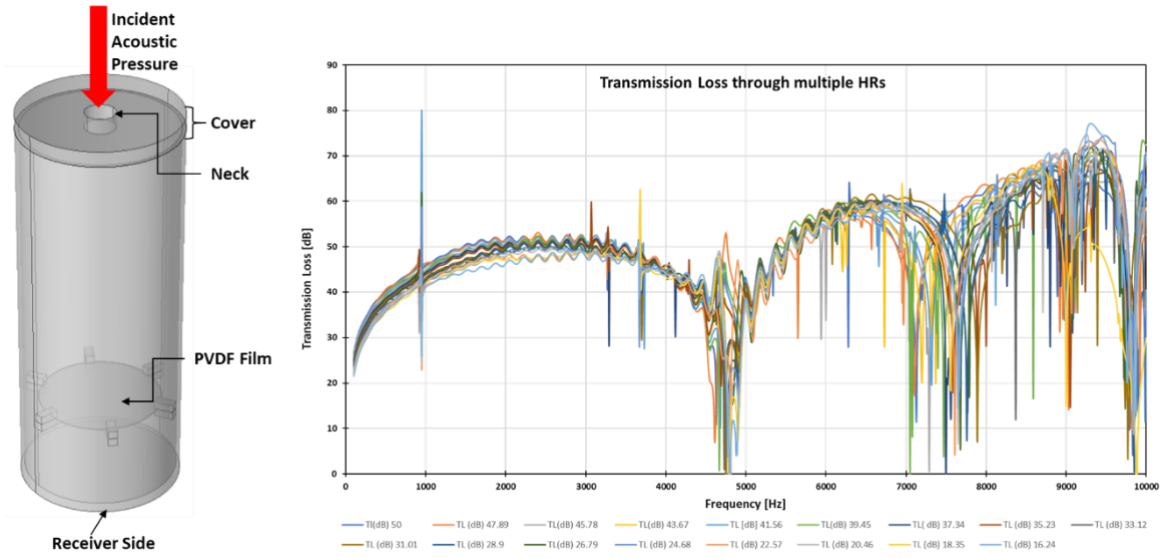

Figure 6. 1: (a) generic model of the Helmholtz resonator with PVDF trampoline (b) transmission loss analysis of various Helmholtz resonators.

The initial analysis shows that all the resonators works good in our desired frequency range (100Hz-10K Hz). There I s significant amount of transmission loss throughout our desired range. Considering the results, it is evident that further modification of the design will lead to enhanced noise filtering capability.

One of the major standards to consider the efficiency of the noise filtering material is STC rating. Any material with STC rating of 30 or higher can work as noise barrier. Keeping this in mind, the STC rating of the largest HR was calculated. It has been found

that this HR has a STC rating of 42, which is much higher than the threshold value. It is expected that assembly of multiple HRs will increase in higher STC rating and thus provide higher noise elimination. But STC ratings don't add up with added layer or element. Instead, it is calculated from a nonlinear decibel sound transmission loss measurement. A very efficient way to add multiple HRs in a confined space is to arrange them in spiral pattern. To validate the concept, initially 7 HRs with gradually changing height is assembled inside a block for numerical analysis.

6.2.1 Design Parameters

The unit cell of the spiral design is achieved by arranging Helmholtz resonators in a spiral pattern. The unit cell consists of seven cylindrical Helmholtz resonators (HR) with gradually increasing diameter and height. The smallest HR has a diameter of is 10mm and the largest one is 22mm. There is a gradual increase in diameter from 10 to 22 mm. The height of the HRs ranges from 20mm to 50mm. The cylinder heights are increased in a step of 5mm each time. The HR with the smallest diameter has the smallest height. The height and diameter increase proportionally. Though the height and diameter of the HRs are different, all of them have uniform neck height and diameter. Neck height and diameter of the HR cylinders are 2mm and 4mm respectively. All the HRs have a wall thickness of 1mm. The HRs are arranged in a spiral pattern inside a cubic block. The cubic block has a dimension of (67X62X56) mm. The block has a uniform wall thickness of 2 mm. To minimize the weight of the cell, the Helmholtz resonators and the block is composed of PVC. A PVDF film is attached inside the cylinder like a trampoline to harvest energy from the cell.

Table 6. 1: Material properties of cell constituents

Material	Density [kg/m^3]	Elastic Modulus [Pa]	Poisson's ratio	Relative permittivity
PVC	1760	2.9e09	0.32	4.0
PVDF	1780	2.0-4.0	0.3	12-13

The position of the PVDF film is also uniform throughout the changing HR dimensions. It is placed 10mm above the bottom surface of the cylinders irrespective of their height. This position of the PVDF film ensures that the maximum amount of acoustic pressure is focused on the film and thus enforcing maximum stress on the film. The material properties of the cell constituents are expressed in. The cell design is demonstrated in further detail in Figure 6.2. Figure 6.2 (a) shows the 3D view of the unit cell where the arrangements of the Helmholtz resonators within the cubic block can be observed.

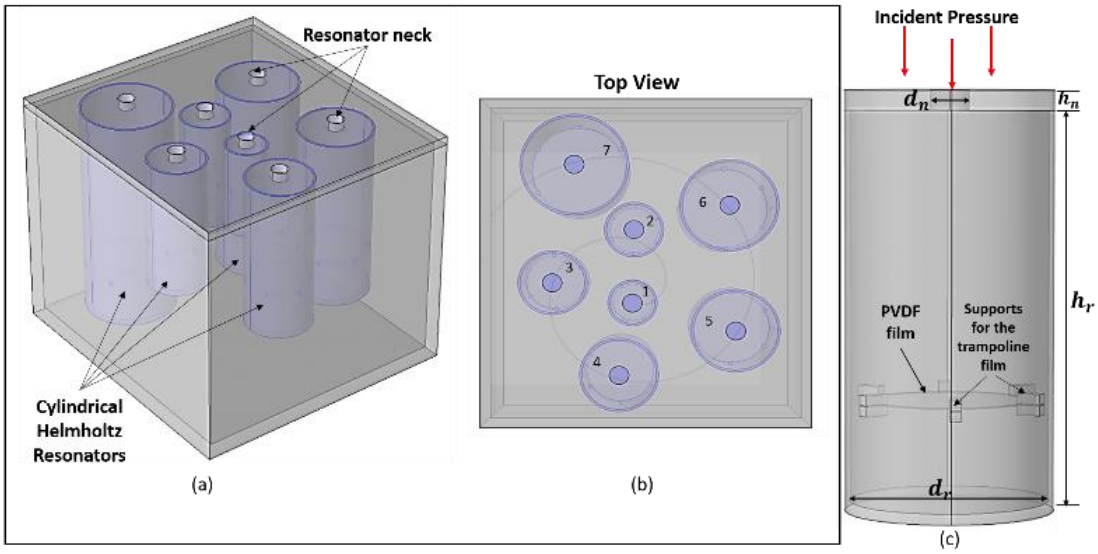

Figure 6. 2: (a) 3D view of the unit cell (b) top view of the unit cell with the spiral arrangement of the Helmholtz resonators (c) overall model of the individual Helmholtz Resonator used in the unit cell.

Figure 6.2 (b) helps to visualize the cell from the top view, where the spiral arrangement can be observed better. The HRs are numbered from 1 to 7 according to their size, 1 being the smallest to 7 being the largest in terms of dimension. The use of PVC has made the cell lighter in weight. The total weight of this unit cell is only 52.5grams which is very low compared to the conventional noise barrier material weight. Figure 6.2 (c) portrays the configuration of the individual HR used in the unit cell. From this figure, the position of the PVDF film inside the cylinder in the form of a trampoline can be seen. The diameter and height of the HR are expressed as d_r and h_r while the neck diameter and height are expressed as d_n and h_n. The incident pressure is applied perpendicular to the face of the neck.

6.2.2 Analytical model Development

According to Ryoo and Jeon[152] when N number of HRs with different resonance frequencies are arranged in a plane the equivalent impedance can be expressed as the reciprocal of the sum of admittance of each HR. In the spiral metamaterial, the HRs are arranged in the same plane so according to Ryoo and Jeon, the equivalent acoustic impedance of the cell can be expressed as:

$$\boldsymbol{Z_M} = \frac{\mathbf{1}}{\sum_{i=1}^{N} \boldsymbol{Y_{HR,i}}} = \frac{\mathbf{1}}{\sum_{i=1}^{N} \frac{\mathbf{1}}{\boldsymbol{Z_{HR,i}}}} \quad \text{Eq 6. 1}$$

Here Z is the acoustic impedance of the cell and Y is the admittance of the Helmholtz resonators (i=1,2,3…etc). In this study, the model is evaluated based on the sound pressure level at the incident and receiver side. The sound Pressure level is defined as the ratio of sound pressure and reference pressure on the logarithmic scale. It can be expressed as

$$SPL = 20log\frac{P}{P_0} \quad \text{Eq 6. 2}$$

SPL is used in this study to analyze the transmission loss from the cell incident to the receiver side. The classic formula for acoustic transmission loss is expressed as:

$$TL = 10log\frac{W_i}{W_t} \quad \text{Eq 6. 3}$$

Here, W_i and W_t are the incident and transmitted wave power. The transmission loss between the incident and the receiver side of the cell is computed in this study. The single-layer piezoelectric PVDF trampoline shown in figure-6.1 can experience the bending deflection similar to a disc. Since the piezoelectric phase works in 31-mode operation for the present configuration, the piezoelectric constitutive equations are

$$\begin{aligned} S_1 &= s_{11}^E T_1 + d_{31}E_3 \\ D_3 &= \varepsilon_{33}^T E_3 + d_{31}T_1 \end{aligned} \quad \text{Eq 6. 4}$$

where S_1 and T_1 are the strain and stress in the radial direction of a piezoelectric layer respectively; D_3 and E_3 are the electric displacement and electric field respectively; s_{11}^E, d_{31}, and ε_{33}^T are the elastic compliance at a constant electric field, the transverse piezoelectric coefficient, and the permittivity at a constant stress of the piezoelectric layer respectively.

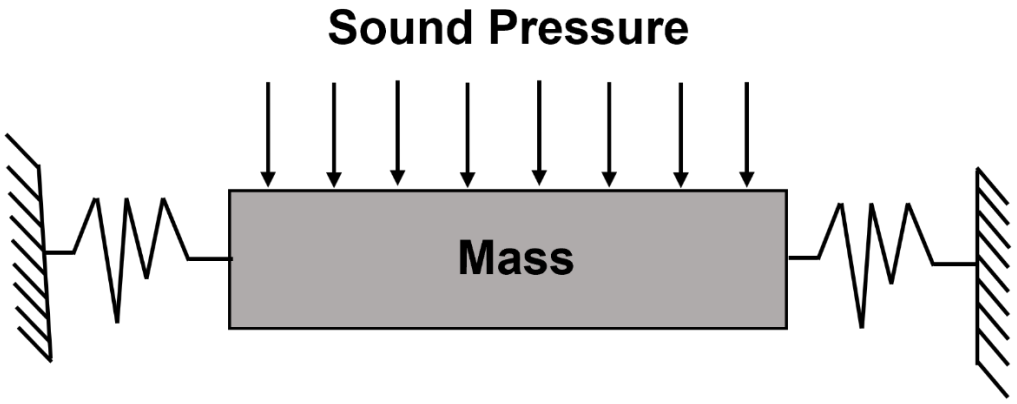

Figure 6. 3: The mass spring model of the Helmholtz resonator

For the Helmholtz resonator, the air in the neck part can be regarded as a mass vibrating with the incident sound waves, while the air in the container is expanded and shrunk due to the vibrations of the air through the neck. Then, it can be seen as a spring mass system, as shown in Figure 6.3. The basic resonance frequency of the HR in response to the incident sound pressure crossing the neck is given as

$$f = \frac{c}{2\pi}\sqrt{\frac{A_n}{VL_n}} \quad \text{Eq 6. 5}$$

$$A_n = \pi r_n^2 \quad \textit{Eq 6. 6}$$

$$V = \pi r^2 h \quad \textit{Eq 6. 7}$$

where f is the basic resonance frequency of the HR, c is the speed of sound in the air, $A_n$is the cross-section area of the neck, V is the volume of cavity, $L_n$is the effective length of neck, $r_n$is the radius of the neck, h is the height of the cylinder cavity and r is the radius of the cylindrical HR. The HR in the system is utilized to amplify the sound pressure with the proximity of noise at the resonance frequency. When the HR is excited at the resonance frequency, the incident sound pressure is amplified resonantly to obtain the peak value of the sound pressure output in the cavity. The pressure amplification factor A stands for the ratio of the sound pressure in the cavity to the incident sound pressure, which is represented as

$$A = \frac{P_{cavity}}{P_{incident}} \quad \textit{Eq 6. 8}$$

When the HR is excited by an incident sound wave at the basic resonance frequency, the acoustic energy is harvested in the form of a resonant standing wave inside the HR. The energy harvesting model for the membrane is already discussed in Chapter 3.

6.2.3 Numerical Model Analysis

To confirm the theoretical model developed in the previous section, finite element analysis (FEA) is performed using COMSOL Multiphysics. The unit cell is exposed to acoustic impedance boundary conditions. The sound source is employed in the form of a plane wave which is located at the top surface of the air tunnel. Li[153] suggested that for the case of Helmholtz resonators, placement of the piezoelectric material closer to the neck opening is more effective, but considering the fact that our Helmholtz resonators are very small, the PVDF film is placed closer to the bottom surface of the cylinder. To evaluate the effectiveness of the model for charging batteries of various power, the model is tested under various load resistances.

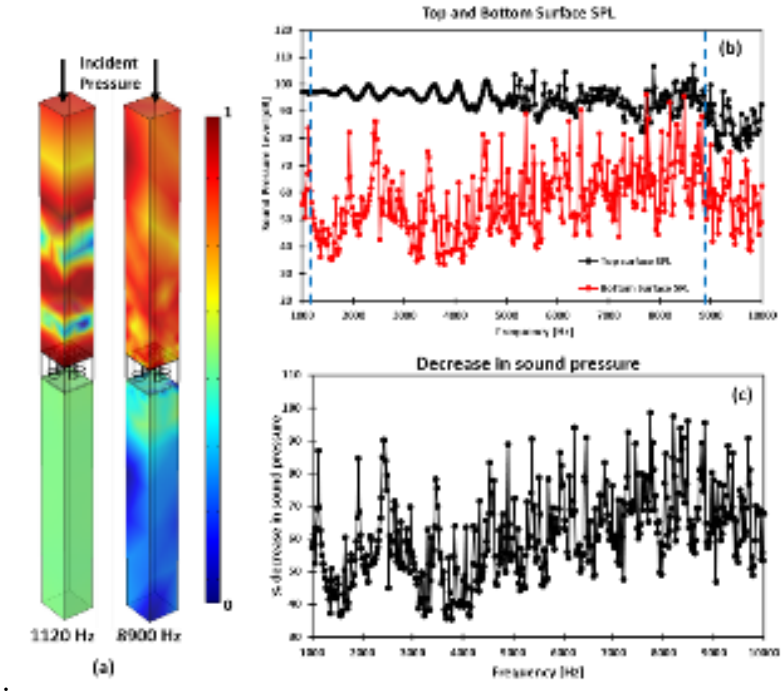

Figure 6. 4: (a) Change in sound pressure level on either side of the noise absorbing cell at two different frequencies; (b) Sound pressure level on the top & bottom surface of the unit cell; (c) Percent decrease in the sound pressure level through the unit cell.

In the acoustics module, this problem fits three boundary conditions such as sound hard boundary, plane wave radiation, and incident pressure of 1Pa (94dB). At the sound

hard boundary, the normal component of the acceleration is zero. On the other hand, the plane wave radiation makes sure that the outgoing sound wave has a minimal reflection. The plane wave radiation is suited to far-field boundaries which are applied to the model. Based on equation (4) it is evident that the transmission loss is not dependent on incident pressure, so the third boundary condition should not affect the results.

Figure 6.4 (a) helps to visualize the sound pressure level from the numerical simulation model. It is clear that the sound pressure is very low in the receiver side compared to the incident part and portrays the effectiveness of the cell in minimizing the sound pressure level at various frequencies. The sound pressure level on the incident side (top surface) and reception side (bottom surface) can be seen from Figure 6.4 (b). It is clear from the plot that the sound pressure level is much lower in the bottom surface compared to the top surface for the frequency range of interest. Figure 6.4(c) represents the percent decrease in the sound pressure level for the employment of the noise filtering cell. A decrease in the sound pressure level is observed to be at least 35% or higher. This result suggests that this unit cell is suitable for use in the field of noise filters.

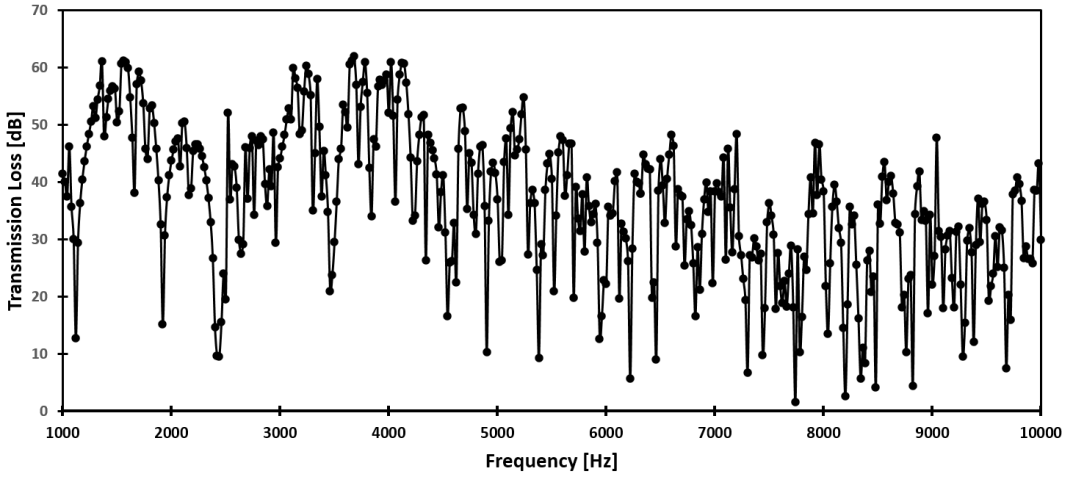

Figure 6. 5: Transmission loss from incident face to the receiver face of the unit cell.

In this study, the transmission loss (TL) is evaluated by measuring the sound power levels for the model and implementing the TL equation. Figure 6.5 explains the transmission loss through the unit cell in the frequency range of interest. Since there is a presence of multiple HRs, so a huge amount of transmission loss can be observed at multiple frequencies throughout the range. The mode which occurs at around ~1120Hz has a dip in the TL curve. The difference in the TL at this mode is approximately 17.23dB. As multiple HRs are used in this design and each of them has different eigenmodes, so a similar dip in the TL curve is imminent throughout the curve at various frequencies. This makes this model capable of filtering noise in a large frequency range including high and low frequencies. A maximum TL of 32.67dB can be obtained from the entire cell.

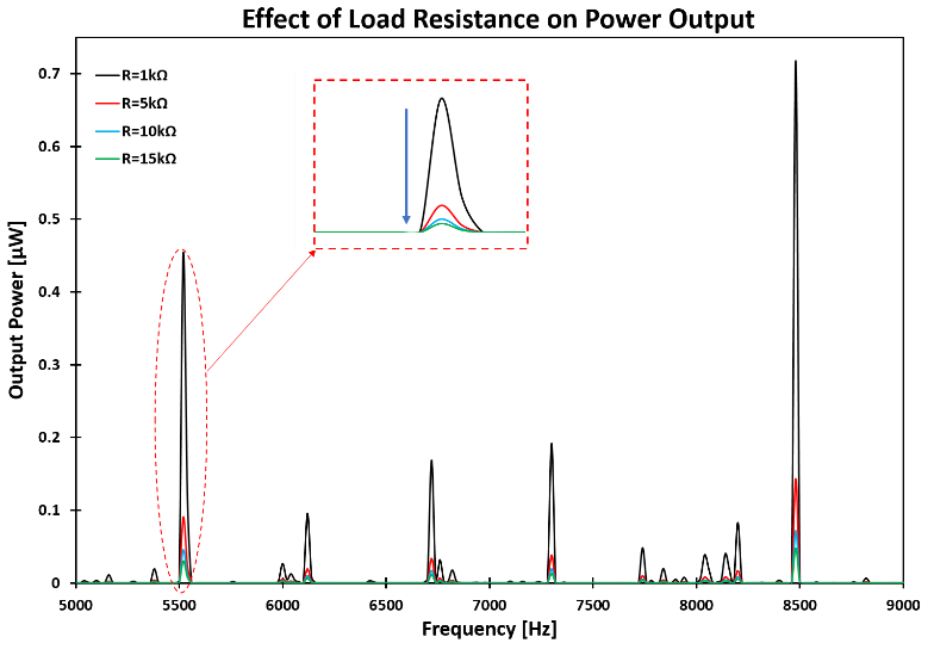

Figure 6. 6: Effect of load resistance on power output from the unit cell due to sound pressure incidence

Using currently available energy harvesting (EH) technologies in the market, it is possible to deliver a small fraction of the electrical power generated in a cell to the load, such as a battery or an inverter. One major drawback of this process is the impossibility of

impedance matching between the load and the EH cell. This mismatch is generated because these two impedances are determined by entirely different and independent factors. The loss of electric power in the system reduces the efficiency of the model. Since this is a multifunctional metamaterial cell and we have the piezoelectric film installed inside the HRs, so it is possible to harvest energy from the incident acoustic pressure. The size of the entire cell is pretty small, but the power output from this cell is exceptionally promising. Figure 6.6 explains the output power spectrum for the entire cell in response to 1 Pa incident pressure at various loading conditions. It can be seen that the output power decreases with the increase in resistive loading. The zoomed-in view in inset helps to visualize this phenomenon. If 1kΩ resistive loading is applied to the model, then a maximum ~ 0.7μW of power can be harvested from this unit cell. In this case, the piezoelectric trampolines in various HRs are connected in parallel to harvest the maximum amount of power possible.

6.3 Proposed solution of the problems using spiral acoustic metamaterial

As discussed earlier, one of the major problems with the previous designs is that they block air flow. Keeping this in mind, the proposed model is designed is such a way that it aids air flow. There are two conditions for a soundproof window where air passes through freely: (a) strong diffraction and (b) negative bulk modulus of the resonators that attenuates the acoustic wave. Strong diffraction makes the wave diffuse into the resonator According to Huygen's principle, every point of a wave front acts as a source of a secondary wave that spreads out in all directions. The envelope of all the secondary waves is the new wave front. A common bottle-type Helmholtz resonator is not suitable for the purpose. Wang et al showed that in an air hole in the center of a cell's body

can maximize the diffraction effect. When the wavelength of the incoming wave is much larger than the size of the holes, it will be diffracted strongly into the holes. Acoustic waves are created by compressibility or elasticity of the medium. Youngs modulus is a one-dimensional, shear modulus is a two-dimensional, and bulk modulus is a three-dimensional compressibility for shear waves. But in principle they are identical. The speed of an acoustic wave in fluid depends on the fluids compressibility and inertia.. The resonance of accumulated waves in the resonator reacts against the applied pressure at some specific frequency ranges. The negative modulus is then realized by passing the acoustic wave through the resonators. This principle is the same with muffler's. By this procedure the amplitude of the sound wave is attenuated exponentially. This is the fundamental mechanism of the attention of acoustic waves by the effective negative bulk modulus. For the soundproof with air flow, the two conditions must both be satisfied.

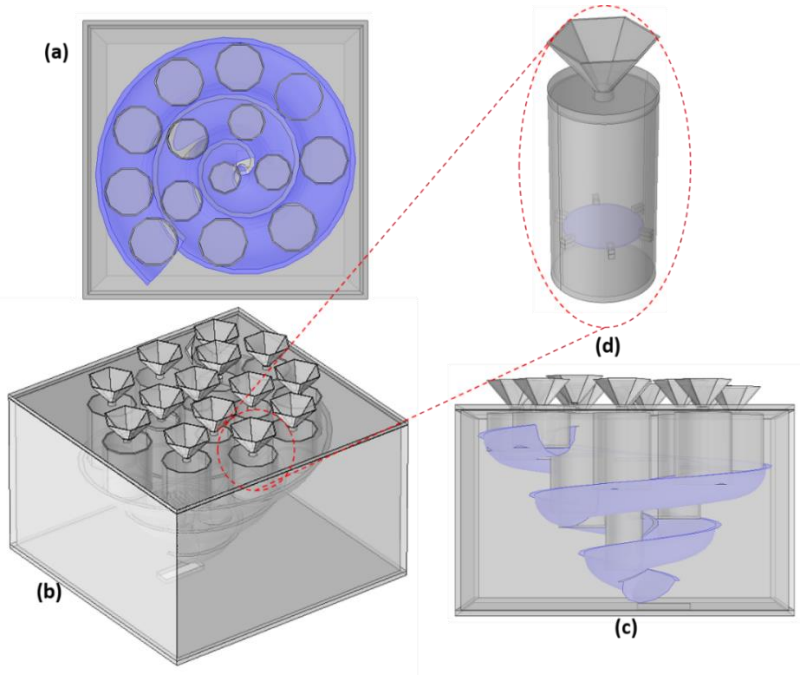

Figure 6. 7: Schematic representation of the Proposed Model (a) top view; (b) unit cell of the design block; (c) spiral groove viewed from the side; (d) unit Helmholtz resonator with hexagonal funnel attachment.

Table 6. 2: Models developed so far

Model Name	Design
MetaWall	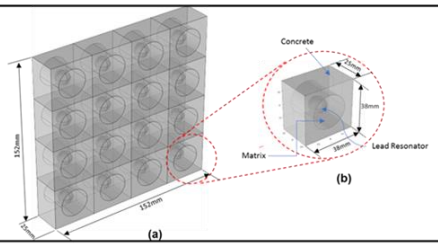
Single Membrane Design	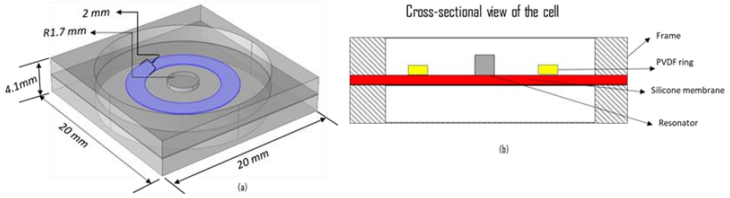
Double Membrane Design	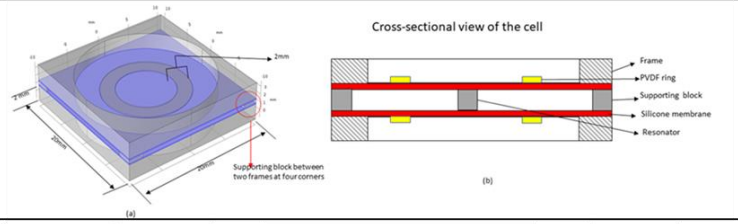
Proposed Spiral Design	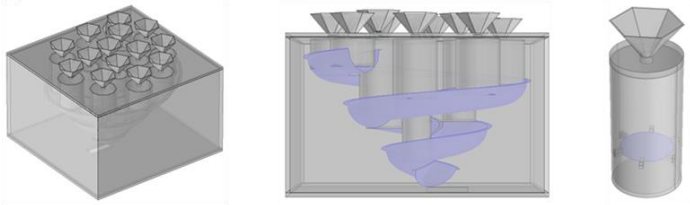

The smaller air hole and lower resonant frequency guarantee the wider frequency range of soundproofing. The larger air hole helps to pass through the air without losing the pressure but it lowers the cutoff frequency. Since the resonators are arrangesd in a spiral pattern with gradually decreasing radius, there will be opening at the top and bottom of the spiral channel to aid air flow. Such spiral pattern will also help to minimize the sound level. Wang et al used conical structures in their design which helps to increase the power output. Following their suggestion, the proposed design uses a funnel on top of each Helmholtz resonator to localize the acoustic waves on top of the PVDF film. This is envisioned to

increase power output from the cells. The projected model is displayed in **Table 6. *2*:** Models developed so fartable 6.2.

This unit cell includes a spiral channel with gradually decreasing diameter places inside a cubic block. The spiral channel has two openings on either side of the block. Helmholtz resonators of varying height with trampoline PVDF film are placed along the spiral channel according to their height. A hexagonal funnel is placed on top of each helmholtz resonator to localize the acoustic pressure. The model is made of PVC, so it is lightweight compared to any other cell of the same dimension. The openings on both side of the channel allows air to flow freely.

Table 6. 3: Pros and Cons of the Previous designs

Ser. No.	**Design**	**Advantages of the Design**	**Disadvantages of the Design**	**Overcoming the disadvantages in the proposed design**
1.	MetaWall	1. Strong and stable 2. High sound absorption capacity 3. Low frequency vibration energy harvesting	1. Blocked air flow 2. Blocked visibility 3. Heavy 4. Works in low frequency range	Needs a lightweight design with enhanced air flow.
2.	Single Membrane Model	1. Lightweight 2. Wide frequency range 3. Miniature design	1. Low power output 2. Low stability of the resonator 3. Vulnerable due to narrow thickness. 4. Not suitable as noise barrier material	Needs a design with higher stability and power output.
3.	Double Membrane Model	1. Strong and stable 2. Works under different loading conditions 3. Comparatively higher power output	1. Blocks air flow and visibility 2. Harvested energy from acoustic source is lower compared to	Needs a design with higher acoustic energy harvesting capability and high absorption coefficient.

		4. Multiple resonance frequencies within the studied range	energy harvested from vibration. 3. Low absorption coefficient	
4.	Proposed Spiral Model	1. Stable 2. Noise filtration in wide frequency range 3. Spiral design allows maximum sound minimization	At this moment, the proposed final full-scale design is yet to be validated.	1. Lightweight 2. Works in a very wide frequency range 3. Sturdy 4. Can be 3D printed 5. Aids air flow 6. Do not block line of sight 7. Aesthetically impressive 8. Higher efficiency 9. Multifunctional 10. Higher absorption coefficient and STC rating

Table 6.3 shows the models that have been developed by us so far. These models have some deficiencies in each of them. It is expected that the newly envisioned design will solve the problems with the existing design. Table 6.3 highlights the pros and cons of the previously reported designs. It also points out the factors that can be overcomed using the proposed design.

6.4 Numerical analysis

To confirm the theoretical model developed in the previous section, finite element analysis (FEA) is performed using COMSOL Multiphysics. The unit cell is exposed to acoustic impedance boundary conditions. The sound source is employed in the form of a plane wave which is located at the top surface of the air tunnel. To evaluate the effectiveness of the

model for charging batteries of various power, the model is tested under various load resistances.

In the acoustics module, this problem fits three boundary conditions such as sound hard boundary, plane wave radiation, and incident pressure of 1Pa (94dB). At the sound hard boundary, the normal component of the acceleration is zero. On the other hand, the plane wave radiation makes sure that the outgoing sound wave has a minimal reflection. The plane wave radiation is suited to far-field boundaries which are applied to the model. Based on equation (6.4) it is evident that the transmission loss is not dependent on incident pressure, so the third boundary condition should not affect the results.

For the electric circuit module, a Wheatstone bridge circuit with four diodes and a capacitor. 10kΩ resistive load is also added to the models. Figure 6.8 shows the power output and the circuit diagram of the energy harvesting model.

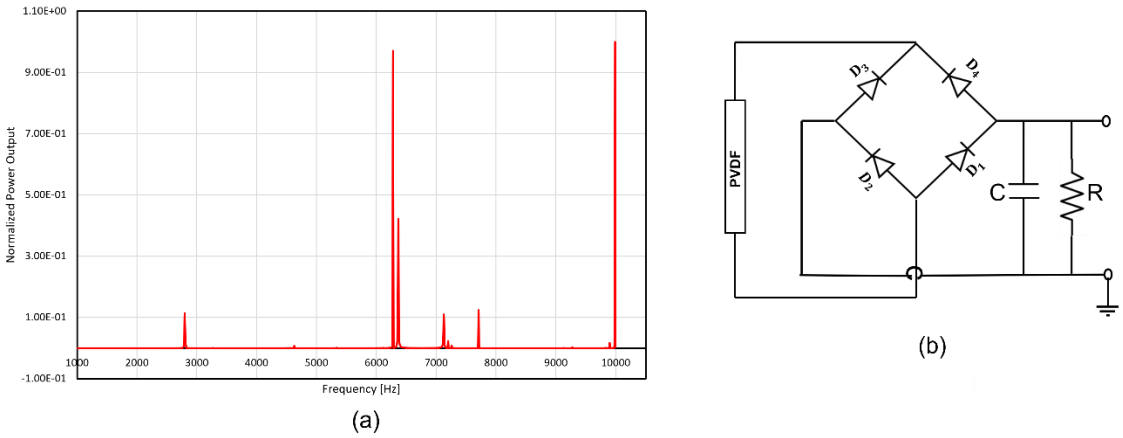

Figure 6. 8: (a) normalized power output from the spiral model (b) circuit used for harvesting power.

The PVDF film was fixed inside the cylindrical HR in the form of a trampoline to receive the resonant sound wave in the resonator. The deformation of the PVDF film

caused by the sound pressure generates electricity. From the measured voltage, the output power was obtained using the formula $\frac{V^2}{R}$ with an optimized resistance of 10kΩ. For this model, the output power is calculated to be ~24.27nW.

In this chapter, a renewable low frequency spiral acoustic energy harvesting noise barrier is systematically developed. The proposed model provides a practical method of energy supply for low power electronic devices along a high noise concentration area at the same time block unwanted noise. For the purposes of noise reduction and electricity generation, the proposed system converts sound energy to electricity using a Helmholtz resonator and a PVDF (Polyvinylidene Fluoride) film. Also, there is a spiral channel to aid air flow. The horns attached to the top of the HRs help to concentrate the air pressure on the PVDF film. Hence, the spiral acoustic energy harvesting noise barrier can be used to replace the conventional noise barriers near highways and residential areas in the future. Further, advanced analysis and modification of the model can be done to make it feasible for a wide range of applications.

CHAPTER 7

Conclusion

At the beginning of this research, several objectives were constructed to progress towards the aim of proposing an alternative solution mitigate noise in transport systems and at the same time harvest power utilizing the trapped noise energy. This aim was developed from the review of current industrial practices, which identified their shortcomings for effective noise control. The review then focused on the different classes of acoustic metamaterial, unveiling a cautiously designed acoustic metamaterial as the solution that might be a viable option because it could achieve good acoustical performance at a wide range of frequencies. The final design that is developed so far shows promising output. At the same dimension and weight, the acoustical performance of traditional acoustical treatments would not be comparable.

To summarize the progress done so far, first this research proposes an application of the AESC based on their noise filtration capabilities. It is shown that the AESC can trap a certain frequency within its soft matrix due to its unique mechanical properties. Keeping that in mind, it has been proposed to replace the traditional roadside noise barriers with walls made of AESC. A model MetaWall brick is demonstrated that can be used to build the proposed wall. This structure helps to reduce the intensity of the annoying sound by absorbing most of the incident acoustic waves which prevent the sound to reflect to the atmosphere. Acoustic pressure test shows that almost 60% noise attenuation is possible

using the MetaWall noise barrier. It has been found that a significant amount of power output can be obtained from the MetaWall which can be used to power the streetlights or SHM sensors. Keeping pace with the modern minimization trend, the energy harvester is proposed to be minimized to a much smaller size, as thin as a plate. The prospect, in this case, is very bright as these models can harvest smart amount of power from ambient frequency as low as 100Hz. The next step in this this study proposes a novel design of plate type energy harvester to harvest power from the ambient vibrations of an airplane during flight. Numerical and experimental validation of the model confirms that this model works fine under various loading condition. After further analysis, it can be concluded that the best possible design for such energy harvester would be the double membrane model. Though it has lower power output in some loading conditions, it is the only model that ensures that the resonator is stable at all phases of operation. Moreover, it has the highest stability and its displacement pattern at various frequencies is also uniform. Considering all these aspects, it is proposed that the double membrane model is the best model and can be considered for in-flight energy harvesting to power the SHM sensors. Taking a step forward, an advanced design is proposed as a noise filtering unit cell which addresses the shortcomings found in the previous models. Here, multiple Helmholtz resonators of varying dimensions, arranged in a spiral pattern is proposed. This assembly is placed inside a square box to ensure better noise control, higher stability, and easy arrangement in the form of an array to form a metasurface which can be used in places where noise filtering is a challenge. This model also includes piezoelectric PVDF film in the form of a trampoline to harvest electrical energy from incident sound pressure. The initial study

confirms that this cell is capable of filtering noise and at the same time harvest energy simultaneously.

In conclusion, the objectives crafted at the start of this research has been established partially, leading to a spiral acoustic metamaterial that could potentially be an alternative solution for noise control in industrial and transport systems after further development and optimization. At the present form, the spiral cell was shown to be a feasible upgrade of the noise barriers commonly found around us, not to mention that it is highly versatile and can be easily customized for any noise environment. Being only a proof-of-concept, it is no doubt that the spiral Meta-block still has room for design improvement which is expected to be developed in near future.

7.1 Major Contributions

1. Three designs (AEMM, Plate type harvester and spiral HR block) are proposed to model the sound absorbing filters in targeted frequency range.
2. AEMM is presented to use the trapped frequencies inside the metamaterial in harvesting electrical energy with filtration of acoustic wave using band gap phenomena. It has been confirmed that the proposed design of AEMM can perform within the targeted frequency.
3. Comprehensive predictive mathematical model for the plate type energy harvester is developed. This model can be used to calculate the voltage and power output of the energy harvester for various range of frequency and resistive load. This model can be used for any shape and design.
4. AEMM based energy harvesting procedure is presented and significantly higher power output is recorded compared to the existing harvesters of the similar type.

5. A plate type harvester is designed which is very thin and lightweight and is eligible to be used in aircraft during flight.
6. A design with the potential solution for blocked air flow in noise barriers is proposed.
7. Various novel applications of the noise absorber, plate models and the spiral model are proposed.

7.2 Future Prospective studies

1. Using the developed mathematical models, various designs can be verified and scaled down to micro or nano levels.
2. Optimize the precise frequency selection ability of the proposed models.
3. The spiral model could be improved and thus encourage the development of the noise barrier metamaterials with air flow capability.
4. Fluid flow through the spiral model could be studied further for an even more efficient model.
5. Further study is necessary to increase the sound filtering and energy harvesting capability At the same time measures should be taken to decrease the production cost.
6. Perform necessary study to implement the models in respective applications those are proposed in this dissertation

References

[1] S. Elliott, "Active noise and vibration control in vehicles," in *Vehicle noise and vibration refinement*: Elsevier, 2010, pp. 235-251.

[2] J. Tichy, "Current and future issues of active noise control," *Journal of the Acoustical Society of Japan (E)*, vol. 12, no. 6, pp. 255-262, 1991.

[3] R. J. Silcox, H. C. Lester, and S. B. Abler, "An evaluation of active noise control in a cylindrical shell," 1989.

[4] C. Dorling, G. Eatwell, S. Hutchins, C. Ross, and S. C. SUTCLIFFE, "A demonstration of active noise reduction in an aircraft cabin," *Journal of Sound and Vibration*, vol. 128, no. 2, pp. 358-360, 1989.

[5] S. Elliott, P. Nelson, I. Stothers, and C. Boucher, "Preliminary results of in-flight experiments on the active control of propeller-induced cabin noise," *Journal of Sound and Vibration*, vol. 128, no. 2, pp. 355-357, 1989.

[6] S. Elliot, P. Nelson, I. Stothers, and C. Boucher, "In-flight experiments on the active control of propeller-induced cabin noise," *Journal of Sound and Vibration*, vol. 140, no. 2, pp. 219-238, 1990.

[7] V. Martin, P. Vignassa, and B. Peseux, "Numerical vibro-acoustic modelling of aircraft for the active acoustic control of interior noise," *Journal of sound and vibration*, vol. 176, no. 3, pp. 307-332, 1994.

[8] C. D. Kestell, B. S. Cazzolato, and C. H. Hansen, "Active noise control in a free field with virtual sensors," *The Journal of the Acoustical Society of America*, vol. 109, no. 1, pp. 232-243, 2001.

[9] S. K. Lee, S. M. Lee, and O. D. Kang, "Active sound design of a passenger car based on adaptive order filter," in *INTER-NOISE and NOISE-CON Congress and Conference Proceedings*, 2014, vol. 249, no. 8, pp. 437-440: Institute of Noise Control Engineering.

[10] S.-H. Oh, H.-s. Kim, and Y. Park, "Active control of road booming noise in automotive interiors," *The Journal of the Acoustical Society of America*, vol. 111, no. 1, pp. 180-188, 2002.

[11] M. A. Botto, J. Sousa, and J. S. da Costa, "Intelligent active noise control applied to a laboratory railway coach model," *Control Engineering Practice*, vol. 13, no. 4, pp. 473-484, 2005.

[12] X. Liu, J. Xu, Z. Jiang, and X. Wang, "Application Study of Active Noise Control Technology for Rail Transit Vehicles," in *International Conference on Electrical and Information Technologies for Rail Transportation*, 2017, pp. 163-173: Springer.

[13] P. N. Samarasinghe, W. Zhang, and T. D. Abhayapala, "Recent advances in active noise control inside automobile cabins: Toward quieter cars," *IEEE Signal Processing Magazine*, vol. 33, no. 6, pp. 61-73, 2016.

[14] C. Fuller and J. Jones, "Experiments on reduction of propeller induced interior noise by active control of cylinder vibration," 1987.

[15] M. Simpson, T. Luong, C. Fuller, and J. Jones, "Full-scale demonstration tests of cabin noise reduction using activevibration control," *Journal of Aircraft*, vol. 28, no. 3, pp. 208-215, 1991.

[16] G. Mathur and B. Tran, "Aircraft cabin noise reduction tests using active structural acoustic control," in *15th Aeroacoustics Conference*, 1993, p. 4437.
[17] J. Pan, S. Elliott, and K.-H. Baek, "Analysis of low frequency acoustic response in a damped rectangular enclosure," *Journal of Sound and Vibration*, vol. 223, no. 4, pp. 543-566, 1999.
[18] J. Pan and C. H. Hansen, "Active control of noise transmission through a panel into a cavity. III: Effect of the actuator location," *The Journal of the Acoustical Society of America*, vol. 90, no. 3, pp. 1493-1501, 1991.
[19] J. Pan, C. Hansen, and D. Bies, "Active control of noise transmission through a panel into a cavity: I. Analytical study," *The Journal of the Acoustical Society of America*, vol. 87, no. 5, pp. 2098-2108, 1990.
[20] C. R. Fuller, S. Snyder, C. Hansen, and R. Silcox, "Active control of interior noise in model aircraft fuselages using piezoceramic actuators," *AIAA journal*, vol. 30, no. 11, pp. 2613-2617, 1992.
[21] J. Sun, M. Norris, D. Rossetti, and J. Highfill, "Distributed piezoelectric actuators for shell interior noise control," 1996.
[22] S. Zhou, C. Liang, and C. Rogers, "Integration and design of piezoceramic elements in intelligent structures," *Journal of Intelligent Material Systems and Structures*, vol. 8, no. 4, pp. 363-373, 1997.
[23] A. Grewal, D. Zimcik, L. Hurtubise, and B. Leigh, "Active cabin noise and vibration control for turboprop aircraft using multiple piezoelectric actuators," *Journal of intelligent material systems and structures*, vol. 11, no. 6, pp. 438-447, 2000.
[24] D. Palumbo, R. Cabell, B. Sullivan, and J. Cline, "Active structural acoustic control of interior noise on a Raytheon 1900D," 2000.
[25] C. Niezrecki and H. H. Cudney, "Feasibility to control launch vehicle internal acoustics using piezoelectric actuators," *Journal of Intelligent Material Systems and Structures*, vol. 12, no. 9, pp. 647-660, 2001.
[26] P. Sas and W. Dehandschutter, "Active structural and acoustic control of structure-borne road noise in a passenger car," *Noise & Vibration Worldwide*, vol. 30, no. 5, pp. 17-27, 1999.
[27] F. Fahy and C. Schofield, "A note on the interaction between a Helmholtz resonator and an acoustic mode of an enclosure," *Journal of Sound and Vibration*, vol. 72, no. 3, pp. 365-378, 1980.
[28] A. Cummings, "The effects of a resonator array on the sound field in a cavity," *Journal of Sound and Vibration*, vol. 154, no. 1, pp. 25-44, 1992.
[29] P. L. Driesch, "Acoustic control in enclosures using optimally designed Helmholtz resonators," 2002.
[30] W. Neise and G. Koopmann, "Reduction of centrifugal fan noise by use of resonators," *Journal of Sound and Vibration*, vol. 73, no. 2, pp. 297-308, 1980.
[31] L. Franco, "Low frequency noise control in car cabin by means of the luggage compartment resonator," *Applied Acoustics*, vol. 32, no. 1, pp. 23-34, 1991.
[32] G. Kamci, I. Basdogan, A. Koyuncu, and I. Yilmaz, "Vibro-acoustic modeling of a commercial vehicle to reduce the interior noise level," 2009: Inter-Noise.
[33] S. Kopuz and N. Lalor, "Analysis of interior acoustic fields using the finite element method and the boundary element method," *Applied Acoustics*, vol. 45, no. 3, pp. 193-210, 1995.
[34] A. Seifzadeh, A. Pietrzyk, P. Göransson, and R. Ramakrishnan, "Effect of coupling between passenger compartment and trunk of a car on coupled system natural frequencies using acoustic frequency response function," *Applied acoustics*, vol. 76, pp. 310-318, 2014.
[35] A. Oktav, "The Effects of Trunk Cavity and Air-Gaps in the Acoustic Response of a Passenger Vehicle," *Archives of Acoustics*, vol. 42, 2017.

[36] A. Oktav, G. Anlaş, and Ç. Yılmaz, "The effect of the folding rear-seat aperture in the acoustic response of a sedan car," *Proceedings of the Institution of Mechanical Engineers, Part D: Journal of Automobile Engineering*, vol. 231, no. 2, pp. 253-266, 2017.
[37] E. Laudien and G. Niesl, "Noise level reduction inside helicopter cabins," 1990.
[38] L. Zhao and S. Zhou, "Compact acoustic rainbow trapping in a bioinspired spiral array of graded locally resonant metamaterials," *Sensors*, vol. 19, no. 4, p. 788, 2019.
[39] A. Isozaki, H. Takahashi, H. Tamura, T. Takahata, K. Matsumoto, and I. Shimoyama, "Parallel Helmholtz resonators for a planar acoustic notch filter," *Applied Physics Letters*, vol. 105, no. 24, p. 241907, 2014.
[40] Y. Wang *et al.*, "A renewable low-frequency acoustic energy harvesting noise barrier for high-speed railways using a Helmholtz resonator and a PVDF film," *Applied energy*, vol. 230, pp. 52-61, 2018.
[41] S.-K. Tang, "A review on natural ventilation-enabling façade noise control devices for congested high-rise cities," *Applied Sciences*, vol. 7, no. 2, p. 175, 2017.
[42] A. Selamet and I. Lee, "Helmholtz resonator with extended neck," *The Journal of the Acoustical Society of America*, vol. 113, no. 4, pp. 1975-1985, 2003.
[43] D. Yang, X. Wang, and M. Zhu, "The impact of the neck material on the sound absorption performance of Helmholtz resonators," *Journal of sound and Vibration*, vol. 333, no. 25, pp. 6843-6857, 2014.
[44] A. Doria, "A simple method for the analysis of deep cavity and long neck acoustic resonators," *Journal of Sound and Vibration*, vol. 4, no. 232, pp. 823-833, 2000.
[45] A. J. Tadeu and D. M. Mateus, "Sound transmission through single, double and triple glazing. Experimental evaluation," *Applied Acoustics*, vol. 62, no. 3, pp. 307-325, 2001.
[46] Z. Yang, J. Mei, M. Yang, N. Chan, and P. Sheng, "Membrane-type acoustic metamaterial with negative dynamic mass," *Physical review letters*, vol. 101, no. 20, p. 204301, 2008.
[47] M. Yang, G. Ma, Z. Yang, and P. Sheng, "Coupled membranes with doubly negative mass density and bulk modulus," *Physical review letters*, vol. 110, no. 13, p. 134301, 2013.
[48] L. Y. L. Ang, Y. K. Koh, and H. P. Lee, "Broadband sound transmission loss of a large-scale membrane-type acoustic metamaterial for low-frequency noise control," *Applied Physics Letters*, vol. 111, no. 4, p. 041903, 2017.
[49] X. Cai, Q. Guo, G. Hu, and J. Yang, "Ultrathin low-frequency sound absorbing panels based on coplanar spiral tubes or coplanar Helmholtz resonators," *Applied Physics Letters*, vol. 105, no. 12, p. 121901, 2014.
[50] T. Cavalieri, A. Cebrecos, J.-P. Groby, C. Chaufour, and V. Romero-García, "Three-dimensional multiresonant lossy sonic crystal for broadband acoustic attenuation: Application to train noise reduction," *Applied Acoustics*, vol. 146, pp. 1-8, 2019.
[51] S. Kumar, P. Bhushan, O. Prakash, and S. Bhattacharya, "Double negative acoustic metastructure for attenuation of acoustic emissions," *Applied Physics Letters*, vol. 112, no. 10, p. 101905, 2018.
[52] Y. Li and B. M. Assouar, "Acoustic metasurface-based perfect absorber with deep subwavelength thickness," *Applied Physics Letters*, vol. 108, no. 6, p. 063502, 2016.
[53] Y. Zhu, X. Fan, B. Liang, J. Cheng, and Y. Jing, "Ultrathin acoustic metasurface-based Schroeder diffuser," *Physical Review X*, vol. 7, no. 2, p. 021034, 2017.
[54] C. Zhang and X. Hu, "Three-dimensional single-port labyrinthine acoustic metamaterial: Perfect absorption with large bandwidth and tunability," *Physical Review Applied*, vol. 6, no. 6, p. 064025, 2016.
[55] S. Huang, X. Fang, X. Wang, B. Assouar, Q. Cheng, and Y. Li, "Acoustic perfect absorbers via spiral metasurfaces with embedded apertures," *Applied Physics Letters*, vol. 113, no. 23, p. 233501, 2018.

[56] I. Prasetiyo, E. N. Wongso, and J. Sarwono, "Developing Sub-wavelength Sound Absorber Based on Coiled Up Tube Resonator," *Journal of Engineering and Technological Sciences,* vol. 51, no. 3, pp. 323-336, 2019.
[57] S. Ning, F. Yang, C. Luo, Z. Liu, and Z. Zhuang, "Low-frequency tunable locally resonant band gaps in acoustic metamaterials through large deformation," *Extreme Mechanics Letters,* vol. 35, p. 100623, 2020.
[58] Y. Chen and L. Wang, "Periodic co-continuous acoustic metamaterials with overlapping locally resonant and Bragg band gaps," *Applied Physics Letters,* vol. 105, no. 19, p. 191907, 2014.
[59] F. Casadei, T. Delpero, A. Bergamini, P. Ermanni, and M. Ruzzene, "Piezoelectric resonator arrays for tunable acoustic waveguides and metamaterials," *Journal of Applied Physics,* vol. 112, no. 6, p. 064902, 2012.
[60] R. Ahmed, D. Madisetti, and S. Banerjee, "A sub-wavelength scale acoustoelastic sonic crystal for harvesting energies at very low frequencies (<∼ 1 kHz) using controlled geometric configurations," *Journal of Intelligent Material Systems and Structures,* vol. 28, no. 3, pp. 381-391, 2017.
[61] F. Mir, M. Saadatzi, R. U. Ahmed, and S. Banerjee, "Acoustoelastic MetaWall noise barriers for industrial application with simultaneous energy harvesting capability," *Applied Acoustics,* vol. 139, pp. 282-292, 2018.
[62] C. Cai, Z. Wang, Y. Chu, G. Liu, and Z. Xu, "The phononic band gaps of Bragg scattering and locally resonant pentamode metamaterials," *Journal of Physics D: Applied Physics,* vol. 50, no. 41, p. 415105, 2017.
[63] S. Wen, Y. Xiong, S. Hao, F. Li, and C. Zhang, "Enhanced band-gap properties of an acoustic metamaterial beam with periodically variable cross-sections," *International Journal of Mechanical Sciences,* vol. 166, p. 105229, 2020.
[64] A. O. Krushynska, V. G. Kouznetsova, and M. G. Geers, "Towards optimal design of locally resonant acoustic metamaterials," *Journal of the Mechanics and Physics of Solids,* vol. 71, pp. 179-196, 2014.
[65] C. Lim, "Elastic waves propagation in thin plate metamaterials and evidence of low frequency pseudo and local resonance bandgaps," *Physics Letters A,* vol. 383, no. 23, pp. 2789-2796, 2019.
[66] C. Lim, "Dissipative Multiresonant Pillared and Trampoline Metamaterials with Amplified Local Resonance Bandgaps and Broadband Vibration Attenuation," *Journal of Vibration and Acoustics,* pp. 1-18, 2020.
[67] R. U. Ahmed and S. Banerjee, "Low frequency energy scavenging using sub-wave length scale acousto-elastic metamaterial," *AIP Advances,* vol. 4, no. 11, p. 117114, 2014.
[68] X. Ao and C. Chan, "Far-field image magnification for acoustic waves using anisotropic acoustic metamaterials," *Physical Review E,* vol. 77, no. 2, p. 025601, 2008.
[69] M. M. Indaleeb, H. Ahmed, M. Saadatzi, and S. Banerjee, "Deaf band-based prediction of Dirac cone in acoustic metamaterials," *Journal of Applied Physics,* vol. 127, no. 6, p. 064903, 2020.
[70] M. M. Indaleeb, S. Banerjee, H. Ahmed, M. Saadatzi, and R. Ahmed, "Deaf band based engineered Dirac cone in a periodic acoustic metamaterial: A numerical and experimental study," *Physical Review B,* vol. 99, no. 2, p. 024311, 2019.
[71] X. Wen *et al.*, "Observation of acoustic Landau quantization and quantum-Hall-like edge states," *arXiv preprint arXiv:1807.08454,* 2018.
[72] W. Zhou, Y. Su, W. Chen, and C. Lim, "Voltage-controlled quantum valley Hall effect in dielectric membrane-type acoustic metamaterials," *International Journal of Mechanical Sciences,* vol. 172, p. 105368, 2020.

[73] S. Yves, G. Lerosey, and F. Lemoult, "Structure-composition correspondence in crystalline metamaterials for acoustic valley-Hall effect and unidirectional sound guiding," *EPL (Europhysics Letters)*, vol. 129, no. 4, p. 44001, 2020.
[74] L. Fu and C. L. Kane, "Superconducting proximity effect and Majorana fermions at the surface of a topological insulator," *Physical review letters*, vol. 100, no. 9, p. 096407, 2008.
[75] H. Zhang, C.-X. Liu, X.-L. Qi, X. Dai, Z. Fang, and S.-C. Zhang, "Topological insulators in Bi 2 Se 3, Bi 2 Te 3 and Sb 2 Te 3 with a single Dirac cone on the surface," *Nature physics*, vol. 5, no. 6, pp. 438-442, 2009.
[76] Y. Chen *et al.*, "Experimental realization of a three-dimensional topological insulator, Bi2Te3," *science*, vol. 325, no. 5937, pp. 178-181, 2009.
[77] T. Lee and H. Iizuka, "Bragg scattering based acoustic topological transition controlled by local resonance," *Physical Review B*, vol. 99, no. 6, p. 064305, 2019.
[78] H. Xue, Y. Yang, F. Gao, Y. Chong, and B. Zhang, "Acoustic higher-order topological insulator on a kagome lattice," *Nature materials*, vol. 18, no. 2, pp. 108-112, 2019.
[79] M. Weiner, X. Ni, M. Li, A. Alù, and A. B. Khanikaev, "Demonstration of a third-order hierarchy of topological states in a three-dimensional acoustic metamaterial," *Science Advances*, vol. 6, no. 13, p. eaay4166, 2020.
[80] H. Peng and P. F. Pai, "Acoustic metamaterial plates for elastic wave absorption and structural vibration suppression," *International Journal of Mechanical Sciences*, vol. 89, pp. 350-361, 2014.
[81] Z. He, X. Xiao, and E. Li, "Design for structural vibration suppression in laminate acoustic metamaterials," *Composites Part B: Engineering*, vol. 131, pp. 237-252, 2017.
[82] H. Liu, T. Wu, and Z. Li, "Theoretical modelling and effectiveness study of rail vibration absorber for noise control," *Journal of Sound and Vibration*, vol. 323, no. 3-5, pp. 594-608, 2009.
[83] X. Xiao, Z. He, E. Li, and A. Cheng, "Design multi-stopband laminate acoustic metamaterials for structural-acoustic coupled system," *Mechanical Systems and Signal Processing*, vol. 115, pp. 418-433, 2019.
[84] Y. Yu, L. Tong, and G. Zhao, "Layout optimization of viscoelastic damping for noise control of mid-frequency vibro-acoustic systems," *Structural and Multidisciplinary Optimization*, pp. 1-18, 2020.
[85] Q. Feng, L. Fan, L. Huo, and G. Song, "Vibration reduction of an existing glass window through a viscoelastic material-based retrofit," *Applied Sciences*, vol. 8, no. 7, p. 1061, 2018.
[86] S. Valvano, C. Orlando, and A. Alaimo, "Design of a noise reduction passive control system based on viscoelastic multilayered plate using PDSO," *Mechanical Systems and Signal Processing*, vol. 123, pp. 153-173, 2019.
[87] O. Puscasu, N. Counsell, M. R. Herfatmanesh, R. Peace, J. Patsavellas, and R. Day, "Powering Lights with Piezoelectric Energy-Harvesting Floors," *Energy Technology*, vol. 6, no. 5, pp. 906-916, 2018.
[88] J. Lueke, M. Rezaei, and W. Moussa, "Investigation of folded spring structures for vibration-based piezoelectric energy harvesting," *Journal of Micromechanics and Microengineering*, vol. 24, no. 12, p. 125011, 2014.
[89] H. Liu, C. Lee, T. Kobayashi, C. J. Tay, and C. Quan, "A new S-shaped MEMS PZT cantilever for energy harvesting from low frequency vibrations below 30 Hz," *Microsystem technologies*, vol. 18, no. 4, pp. 497-506, 2012.
[90] W. Liu, M. Han, B. Meng, X. Sun, X. Huang, and H. Zhang, "Low frequency wide bandwidth MEMS energy harvester based on spiral-shaped PVDF cantilever," *Science China Technological Sciences*, vol. 57, no. 6, pp. 1068-1072, 2014.

[91] X. Bai, Y. Wen, P. Li, J. Yang, X. Peng, and X. Yue, "Multi-modal vibration energy harvesting utilizing spiral cantilever with magnetic coupling," *Sensors and Actuators A: Physical*, vol. 209, pp. 78-86, 2014.
[92] N. Zhao *et al.*, "Three-dimensional piezoelectric vibration energy harvester using spiral-shaped beam with triple operating frequencies," *Review of Scientific Instruments*, vol. 87, no. 1, p. 015003, 2016.
[93] Ö. Zorlu and H. Külah, "A MEMS-based energy harvester for generating energy from non-resonant environmental vibrations," *Sensors and Actuators A: physical*, vol. 202, pp. 124-134, 2013.
[94] F. Ewere and G. Wang, "Performance of galloping piezoelectric energy harvesters," *Journal of Intelligent Material Systems and Structures*, vol. 25, no. 14, pp. 1693-1704, 2014.
[95] Z. Yan, W. Sun, T. Tan, and W. Huang, "Nonlinear analysis of galloping piezoelectric energy harvesters with inductive-resistive circuits for boundaries of analytical solutions," *Communications in Nonlinear Science and Numerical Simulation*, vol. 62, pp. 90-116, 2018.
[96] T. Tan and Z. Yan, "Analytical solution and optimal design for galloping-based piezoelectric energy harvesters," *Applied Physics Letters*, vol. 109, no. 25, p. 253902, 2016.
[97] J. Wang, L. Geng, S. Zhou, Z. Zhang, Z. Lai, and D. Yurchenko, "Design, modeling and experiments of broadband tristable galloping piezoelectric energy harvester," *Acta Mechanica Sinica*, pp. 1-14, 2020.
[98] R. C. Dash, D. K. Maiti, and B. N. Singh, "Dynamic stability and performance analysis of a galloping-based piezoelectric energy harvester for different order representations of the aerodynamic force," *International Journal of Non-Linear Mechanics*, vol. 121, p. 103463, 2020.
[99] S. Sun and W. T. Peter, "Modeling of a horizontal asymmetric U-shaped vibration-based piezoelectric energy harvester (U-VPEH)," *Mechanical Systems and Signal Processing*, vol. 114, pp. 467-485, 2019.
[100] R. Hosseini and M. Nouri, "Shape design optimization of unimorph piezoelectric cantilever energy harvester," *Journal of Computational Applied Mechanics*, vol. 47, no. 2, pp. 247-259, 2016.
[101] A. Jemai, F. Najar, M. Chafra, and Z. Ounaies, "Modeling and parametric analysis of a unimorph piezocomposite energy harvester with interdigitated electrodes," *Composite Structures*, vol. 135, pp. 176-190, 2016.
[102] S. Zeng, C. Zhang, K. Wang, B. Wang, and L. Sun, "Analysis of delamination of unimorph cantilever piezoelectric energy harvesters," *Journal of Intelligent Material Systems and Structures*, vol. 29, no. 9, pp. 1875-1883, 2018.
[103] Y. Tsujiura, E. Suwa, T. Nishi, F. Kurokawa, H. Hida, and I. Kanno, "Airflow energy harvester of piezoelectric thin-film bimorph using self-excited vibration," *Sensors and Actuators A: Physical*, vol. 261, pp. 295-301, 2017.
[104] H. G. Yeo, X. Ma, C. Rahn, and S. Trolier-McKinstry, "Efficient piezoelectric energy harvesters utilizing (001) textured bimorph PZT films on flexible metal foils," *Advanced Functional Materials*, vol. 26, no. 32, pp. 5940-5946, 2016.
[105] N. Alsaadi and M. A. Sheeraz, "Design and optimization of bimorph energy harvester based on Taguchi and ANOVA approaches," *Alexandria Engineering Journal*, vol. 59, no. 1, pp. 117-127, 2020.
[106] F. Cottone, L. Gammaitoni, H. Vocca, M. Ferrari, and V. Ferrari, "Piezoelectric buckled beams for random vibration energy harvesting," *Smart materials and structures*, vol. 21, no. 3, p. 035021, 2012.

[107] J. Choi, I. Jung, and C.-Y. Kang, "A brief review of sound energy harvesting," *Nano energy*, vol. 56, pp. 169-183, 2019.
[108] J. Li, X. Zhou, G. Huang, and G. Hu, "Acoustic metamaterials capable of both sound insulation and energy harvesting," *Smart Materials and Structures*, vol. 25, no. 4, p. 045013, 2016.
[109] X. Wang, J. Xu, J. Ding, C. Zhao, and Z. Huang, "A compact and low-frequency acoustic energy harvester using layered acoustic metamaterials," *Smart Materials and Structures*, vol. 28, no. 2, p. 025035, 2019.
[110] S. Qi, M. Oudich, Y. Li, and B. Assouar, "Acoustic energy harvesting based on a planar acoustic metamaterial," *Applied Physics Letters*, vol. 108, no. 26, p. 263501, 2016.
[111] M. Yuan, Z. Cao, J. Luo, and Z. Pang, "Helix structure for low frequency acoustic energy harvesting," *Review of Scientific Instruments*, vol. 89, no. 5, p. 055002, 2018.
[112] M. Yuan, Z. Cao, J. Luo, and R. Ohayon, "Acoustic metastructure for effective low-frequency acoustic energy harvesting," *Journal of Low Frequency Noise, Vibration and Active Control*, vol. 37, no. 4, pp. 1015-1029, 2018.
[113] M. Yuan, Z. Cao, J. Luo, and Z. Pang, "Low frequency acoustic energy harvester based on a planar Helmholtz resonator," *AIP Advances*, vol. 8, no. 8, p. 085012, 2018.
[114] A. Yang *et al.*, "Enhanced acoustic energy harvesting using coupled resonance structure of sonic crystal and Helmholtz resonator," *Applied Physics Express*, vol. 6, no. 12, p. 127101, 2013.
[115] S.-H. Kim and S.-H. Lee, "Air transparent soundproof window," *AIP Advances*, vol. 4, no. 11, p. 117123, 2014.
[116] X. Wu *et al.*, "High-efficiency ventilated metamaterial absorber at low frequency," *Applied Physics Letters*, vol. 112, no. 10, p. 103505, 2018.
[117] C. Shen, Y. Xie, J. Li, S. A. Cummer, and Y. Jing, "Acoustic metacages for sound shielding with steady air flow," *Journal of Applied Physics*, vol. 123, no. 12, p. 124501, 2018.
[118] L.-j. Li, B. Zheng, L.-m. Zhong, J. Yang, B. Liang, and J.-c. Cheng, "Broadband compact acoustic absorber with high-efficiency ventilation performance," *Applied Physics Letters*, vol. 113, no. 10, p. 103501, 2018.
[119] H.-l. Zhang, Y.-f. Zhu, B. Liang, J. Yang, J. Yang, and J.-c. Cheng, "Omnidirectional ventilated acoustic barrier," *Applied Physics Letters*, vol. 111, no. 20, p. 203502, 2017.
[120] R. Ghaffarivardavagh, J. Nikolajczyk, S. Anderson, and X. Zhang, "Ultra-open acoustic metamaterial silencer based on Fano-like interference," *Physical Review B*, vol. 99, no. 2, p. 024302, 2019.
[121] J. W. Jung, J. E. Kim, and J. W. Lee, "Acoustic metamaterial panel for both fluid passage and broadband soundproofing in the audible frequency range," *Applied Physics Letters*, vol. 112, no. 4, p. 041903, 2018.
[122] S. Onder and Z. Kocbeker, "Importance of the green belts to reduce noise pollution and determination of roadside noise reduction effectiveness of bushes in Konya, Turkey," *Turkey. World Academy of Science, Engineering, and Technology*, vol. 66, no. 6, pp. 11-14, 2012.
[123] G. R. Watts and N. S. Godfrey, "Effects on roadside noise levels of sound absorptive materials in noise barriers," *Applied Acoustics*, vol. 58, no. 4, pp. 385-402, 1999/12/01/ 1999.
[124] M. E. Nilsson, M. Andéhn, and P. Leśna, "Evaluating roadside noise barriers using an annoyance-reduction criterion," *The Journal of the Acoustical Society of America*, vol. 124, no. 6, pp. 3561-3567, 2008.
[125] M. R. Monazzam and S. M. B. Fard, "Performance of passive and reactive profiled median barriers in traffic noise reduction," *Journal of Zhejiang University-SCIENCE A*, journal article vol. 12, no. 1, pp. 78-86, January 01 2011.

[126] X. Wang, D. Mao, W. Yu, and Z. Jiang, "Sound barriers from materials of inhomogeneous impedance," *The Journal of the Acoustical Society of America,* vol. 137, no. 6, pp. 3190-3197, 2015.
[127] M. Naderzadeh, M. R. Monazzam, P. Nassiri, and S. M. B. Fard, "Application of perforated sheets to improve the efficiency of reactive profiled noise barriers," *Applied Acoustics,* vol. 72, no. 6, pp. 393-398, 2011/05/01/ 2011.
[128] Z. Chen, B. Guo, Y. Yang, and C. Cheng, "Metamaterials-based enhanced energy harvesting: A review," *Physica B: Condensed Matter,* vol. 438, pp. 1-8, 2014.
[129] S. A. Cummer, J. Christensen, and A. Alù, "Controlling sound with acoustic metamaterials," *Nature Reviews Materials,* vol. 1, p. 16001, 2016.
[130] A. Can, L. Leclercq, J. Lelong, and D. Botteldooren, "Traffic noise spectrum analysis: Dynamic modeling vs. experimental observations," *Applied Acoustics,* vol. 71, no. 8, pp. 764-770, 2010.
[131] C. Buratti and E. Moretti, "Traffic noise pollution: spectra characteristics and windows sound insulation in laboratory and field measurements," *Journal of Environmental Science and Engineering,* vol. 4, no. 12, 2010.
[132] W. Choi, Y. Jeon, J.-H. Jeong, R. Sood, and S.-G. Kim, "Energy harvesting MEMS device based on thin film piezoelectric cantilevers," *Journal of Electroceramics,* vol. 17, no. 2, pp. 543-548, 2006.
[133] Z. Wang and Y. Xu, "Vibration energy harvesting device based on air-spaced piezoelectric cantilevers," *Applied Physics Letters,* vol. 90, no. 26, p. 263512, 2007.
[134] A. Erturk and D. J. Inman, "An experimentally validated bimorph cantilever model for piezoelectric energy harvesting from base excitations," *Smart materials and structures,* vol. 18, no. 2, p. 025009, 2009.
[135] Z. Chen, Y. Yang, Z. Lu, and Y. Luo, "Broadband characteristics of vibration energy harvesting using one-dimensional phononic piezoelectric cantilever beams," *Physica B: Condensed Matter,* vol. 410, pp. 5-12, 2013.
[136] S. Gonella, A. C. To, and W. K. Liu, "Interplay between phononic bandgaps and piezoelectric microstructures for energy harvesting," *Journal of the Mechanics and Physics of Solids,* vol. 57, no. 3, pp. 621-633, 3// 2009.
[137] M. Carrara, M. Cacan, J. Toussaint, M. Leamy, M. Ruzzene, and A. Erturk, "Metamaterial-inspired structures and concepts for elastoacoustic wave energy harvesting," *Smart Materials and Structures,* vol. 22, no. 6, p. 065004, 2013.
[138] H. Lv, X. Tian, M. Y. Wang, and D. Li, "Vibration energy harvesting using a phononic crystal with point defect states," *Applied Physics Letters,* vol. 102, no. 3, p. 034103, 2013.
[139] L.-Y. Wu, L.-W. Chen, and C.-M. Liu, "Acoustic energy harvesting using resonant cavity of a sonic crystal," *Applied Physics Letters,* vol. 95, no. 1, p. 013506, 2009.
[140] J.-C. Hsu, "Local resonances-induced low-frequency band gaps in two-dimensional phononic crystal slabs with periodic stepped resonators," *Journal of Physics D: Applied Physics,* vol. 44, no. 5, p. 055401, 2011.
[141] P. Sheng, X. X. Zhang, Z. Liu, and C. T. Chan, "Locally resonant sonic materials," *Physica B: Condensed Matter,* vol. 338, no. 1–4, pp. 201-205, 10// 2003.
[142] R. U. Ahmed and S. Banerjee, "Wave propagation in metamaterial using multiscale resonators by creating local anisotropy," *International Journal of Modern Engineering,* vol. 13, no. 2, p. 51, 2013.
[143] R. Ahmed and S. Banerjee, "Predictive electromechanical model for energy scavengers using patterned piezoelectric layers," *Journal of Engineering Mechanics,* vol. 141, no. 2, p. 04014113, 2014.
[144] R. Ahmed, F. Mir, and S. Banerjee, "A review on energy harvesting approaches for renewable energies from ambient vibrations and acoustic waves using piezoelectricity," *Smart Materials and Structures,* vol. 26, no. 8, p. 085031, 2017.

[145] R. U. Ahmed, A. Adiba, and S. Banerjee, "Energy scavenging from acousto-elastic metamaterial using local resonance phenomenon," in *Active and Passive Smart Structures and Integrated Systems 2015*, 2015, vol. 9431, p. 943106: International Society for Optics and Photonics.
[146] G. Ma, M. Yang, S. Xiao, Z. Yang, and P. Sheng, "Acoustic metasurface with hybrid resonances," *Nature materials*, vol. 13, no. 9, p. 873, 2014.
[147] M. I. Hussein, "Reduced Bloch mode expansion for periodic media band structure calculations," in *Proceedings of the Royal Society of London A: Mathematical, Physical and Engineering Sciences*, 2009, vol. 465, no. 2109, pp. 2825-2848: The Royal Society.
[148] M. R. U. Ahmed, "Bio-inspired design of mechanical band pass sensor with the ability to scavenge energy," University of South Carolina, 2015.
[149] R. Ahmed, D. Madisetti, and S. Banerjee, "A sub-wavelength scale acoustoelastic sonic crystal for harvesting energies at very low frequencies (<∼1 kHz) using controlled geometric configurations," *Journal of Intelligent Material Systems and Structures*, vol. 28, no. 3, pp. 381-391, 2017/02/01 2016.
[150] M. Saadatzi, M. N. Saadatzi, R. Ahmed, and S. Banerjee, "An electro-dynamic 3-dimensional vibration test bed for engineering testing," in *Industrial and Commercial Applications of Smart Structures Technologies 2017*, 2017, vol. 10166, p. 101660D: International Society for Optics and Photonics.
[151] A. H. Hosseinloo and K. Turitsyn, "Design of vibratory energy harvesters under stochastic parametric uncertainty: a new optimization philosophy," *Smart Materials and Structures*, vol. 25, no. 5, p. 055023, 2016.
[152] H. Ryoo and W. Jeon, "Dual-frequency sound-absorbing metasurface based on visco-thermal effects with frequency dependence," *Journal of Applied Physics*, vol. 123, no. 11, p. 115110, 2018.
[153] B. Li, J. H. You, and Y.-J. Kim, "Low frequency acoustic energy harvesting using PZT piezoelectric plates in a straight tube resonator," *Smart Materials and Structures*, vol. 22, no. 5, p. 055013, 2013.

Appendix A: Matlab code used for Plate type harvester

```
%%%%%%%%%%% Multiple Resistance with Patch  %%%%%%%%%%%
% Code by Fariha Mir and Sourav Banerjee November 2021

%%  INPUT VARIABLES ONLY
Es=8.89e6;                                  % Es = elastic modulus of substrate
structure
Ep=5.7e9;                                   % Ep = elastic modulus of piezoelectric
coating
mus=0.48;                                   % mu_s = shear modulus of substrate
structure
mup=0.35;                                   % mu_p = shear modulus of
piezoelectric coating
q0=0;%5000;
r_r=0.00170; % readius of the resonator
tr=0.005; % thickness of the resonator
ms=5800;    %kg/m^3
mp=3400;    %kg/m^3
m_r=8050;    %kg/m^3
                % kg/m^2
```

```
hs=0.001;                                   % hs = thickness of Substrate-Host
structure (meter)
hp=0.001;                                   % hp = thickness of piezoelectric
layer (meter)
a=0.20;                                     % a = Length of piezoelectric layer
(meter)
b=0.20;                                     % b = Width of piezoelectric layer
(meter)
Wb=0.001;%0.002;                            % Wb = amplitude of the
transverse vibration
Num_Xpatch=1;
Num_Ypatch=1;
Num_Xmode=5;
Num_Ymode=5;
TotalPatch=Num_Xpatch*Num_Ypatch;
n1=a/Num_Xpatch;                            % n = Patch Length/Width
(meter) (Considering Square Patch)
n2=b/Num_Ypatch;
%RL=[100 400];%R=TotalPatch.*RL;            % R = Resistive
load (ohm)
%R=RL;
%Num_Freq=size(freq,2);
%d31=-220/1000000000000;                    % unit pF
```

```
d31=-70/1000000000000;
pi=22/7;
i=sqrt(-1);
gi=[0.015 0.02 0.025]';
hsp=((hs^3) - ((hs+2*hp)^3))/24;
%gi=gi;%xin/TotalPatch;
ep33=12*8.854/1000000000000;                    % eps_p33 = permittivity
matrix of the PZT layer
theta=0;

%% CALCULATION START HERE..... DO NOT CHANGE.
hpc=(hs/2)+(hp/2);                              % hpc = distance of the center
plane of the PZT from the neutral axis of the system

ma=(ms+mp)/2;          % average mass kg/m^3
mr=m_r*(pi*r_r^2)*tr;  % mass of the resonator
%m=ma*(hs+hp)/1000000000000000   % mg/mm^2  in mm
%m=mr+(ma*(hs+hp)*a*b);                 % kg/m^2
m=(ma*(hs+hp));

c11p=Ep/(1-(mup^2));
c12p=(Ep*mup)/(1-(mup^2));
c21p=c12p;
```

```
c22p=c11p;


d32=d31;

e31=(d31*c11p)+(d32*c12p);

e32=e31;


V31=(e31*(hp+hs))/2;   % Revised 05/22/14                    % unit C/m

V32=(e31*(hp+hs))/2;   % Revised 05/22/14

Ds=Es/(24*(1-(mus^2)));

Dp=Ep/(24*(1-(mup^2)));


Yp=-((Dp*((hs+(2*hp))^3))-(Dp*(hs^3)));          %correction

Ys=-(2*Ds*(hs^3));

Yc=-(2*Ds*(1-mus)*(hs^3))-(Dp*(1-mup)*(((hs+(2*hp))^3)-(hs^3)));


Zi1=Ys+Yp;

Zi2=2*((Ys*mus)+(Yp*mup)+Yc);


Cp11=c11p;

Cp12=c12p;

C=d31*(Cp11+Cp12);


for r=1:Num_Xmode;
```

```
    for s=1:Num_Ymode;
        coefr=((r*pi)/a)^4;
        coefs=((s*pi)/b)^4;

        k_rs(r,s)=((Zi1*(coefr+coefs))+(Zi2*((sqrt(coefr))*(sqrt(coefs)))));
        wrs(r,s)=imag(sqrt(k_rs(r,s)/m));
    end
end

        mat=[((((pi/a)^4)+((pi/b)^4))*hsp)/(2*m*wrs(1,1)))
((2*(((pi/a)^2)*((pi/b)^2))*hsp)/(2*m*wrs(1,1))) (1/(2*m*wrs(1,1))) ;...
            (((((pi/a)^4)+((2*pi/b)^4))*hsp)/(2*m*wrs(1,2)))
((2*(((pi/a)^2)*((2*pi/b)^2))*hsp)/(2*m*wrs(1,2)))  (1/(2*m*wrs(1,2))) ; ...
            (((((2*pi/a)^4)+((2*pi/b)^4))*hsp)/(2*m*wrs(2,2)))
((2*(((2*pi/a)^2)*((2*pi/b)^2))*hsp)/(2*m*wrs(1,2))) (1/(2*m*wrs(2,2)))];
        c=inv(mat)*gi;

Csrx=c(1);
Csry=c(2);
Ca=c(3);

ita33=ep33-(2*(d31^2)*(Cp11+Cp12));
cap33=(ita33*a*b)/hp;
```

```
for k=1:Num_Xpatch;
for j=1:Num_Ypatch;
   x(k)=(k-1)*n1;
   y(j)=(j-1)*n2;

for r=1:Num_Xmode;
   for s=1:Num_Ymode;

      Cox(r,s,k)=((cos((pi*r*(x(k)+n1))/a))-(cos((pi*r*(x(k)))/a)));  % revised removed
(4/a*b)
      Coy(r,s,j)=((cos((pi*s*(y(j)+n2))/b))-(cos((pi*s*(y(j)))/b)));  % revised removed
(4/a*b)
      Six(r,s,k)=((sin((pi*r*(x(k)+n1))/a))-(sin((pi*r*(x(k)))/a)));
      Siy(r,s,j)=((sin((pi*s*(y(j)+n2))/b))-(sin((pi*s*(y(j)))/b)));
%

   end
end
end
end

for r=1:Num_Xmode;
```

```
   for s=1:Num_Ymode;
       coefr=((r*pi)/a)^4;
       coefs=((s*pi)/b)^4;


ziz(r,s)=((Csrx*(((coefr)+(coefs))))+(2*Csry*(sqrt(coefr))*(sqrt(coefr)))+Ca)/(2*m*(wrs
(r,s)));
%       xii(r,s)=(ziz(r,s))/(2*m*(wrs(r,s)));
%        zi(r,s)=Ca/(2*m*(omg_rs(r,s)));

   end
 end



%% Location of the Patch
x_2 =0.12;
x_1=0.08;
y_2=0.12;
y_1=0.08;

% x_2 =a;%0.12;
% x_1=0; %0.08;
```

```
% y_2=b;%0.12;
% y_1=0;%0.08;
%% Loop to solve
R_L=[100 200 400 600 800 1000 5000 10000 20000];
i=sqrt(-1);
for q=1:length(R_L);                                    % Calculation for each
resistance
   %Rl=R(q);
   Rl=R_L(q);
   t=0;
   for f=800:5:1200;
   %for f=10:10:20000;                                  % Calculation for each
frequency
       omg=f;
       t=t+1;
       w(t)=f/1000;

       A1=(i*omg*cap33+(1/Rl));
%       for k=1:Num_Xpatch;                              % Calculation for each X
patch starts here
%           for j=1:Num_Ypatch;                          % Calculation for each Y
patch starts here
%               x(k)=n1*k-n1;
```

```
%               y(j)=n2*j-n2;


        A8=0;
             A9=0;
            for r=1:Num_Xmode;
               for s=1:Num_Ymode;


                  co_r=((r*pi)/a)^4;
                  co_s=((s*pi)/b)^4;
                  phi=16/((pi^2)*r*s);
                  zerodamp=0;

c_rs(r,s)=hsp*((Csrx*(((co_r)+(co_s))))+(2*Csry*(sqrt(co_r))*(sqrt(co_r))))+Ca;


xii(r,s)=((hsp*(((Csrx*(co_r+co_s))+(2*Csry*sqrt(co_s)*sqrt(co_r)))))+Ca)/(2*m*wrs(r,
s));
                  %zi(r,s)=(zerodamp+Ca)/(2*m*(omg_rs(r,s)));
                  cosXm= cos((r*pi*x_2)/a)-cos((r*pi*x_1)/a);
                  cosYn= cos((s*pi*y_2)/b)-cos((s*pi*y_1)/b);
%                    sinXm= sin((r*pi*x_2)/a)-sin((r*pi*x_1)/a);
%                    sinYn= sin((s*pi*y_2)/b)-sin((s*pi*y_1)/b);
                  sinXm=cosXm;
                  sinYn=cosYn;
```

```
%A2(k,j)=C*hpc*(((a*b))/((pi^2)*r*s))*Cox(r,s,k)*Coy(r,s,j)*(sqrt(co_r)+sqrt(co_s));
                A2=C*hpc*(4*a*b/((pi^2)*r*s))*((sqrt(co_r))+(sqrt(co_s)));
                %I=m*(omg^2); %-(i*Ca*omg);
                I=m*(omg^2)-(i*Ca*omg);
                A3=i*phi*omg*((I*Wb)+(q0*exp(i*theta)));
                A4=m*((-(omg^2))+(2*i*xii(r,s)*omg*wrs(r,s))+(wrs(r,s)^2));
                A5=A3/A4;
                A6=A2*A5;
                %VCS=(V31*((b*r)/(a*s))*Cox(r,s,k)*(1-
cos(pi*s)))+(V32*((a*s)/(b*r))*Coy(r,s,j)*(1-cos(pi*r)));

%VCS=(V31*((pi*r)/a)*Cox(r,s,k)*Siy(r,s,k))+(V32*((pi*s)/b)*Coy(r,s,j)*Six(r,s,k));
                VCS=(V31*((pi*r)/a)*cosXm*sinYn)+(V32*((pi*s)/b)*cosYn*sinXm);
                 %VCS=(V31*((pi*r)/a)*Cox(r,s,k))+(V32*((pi*s)/b)*Coy(r,s,j))
                %VCS=V31+V32;
                A7=(A2*(i*omg*(VCS)))/A4;
                A8=A8+A6;
                A9=A9+A7;
            end
        end
```

```
        Voltage(q,t)=(A8/(A1-A9))/1000;   %in mV
        P0(q,t)=(((Voltage(q,t)*1000)^2)/Rl)/1000000; % mV to V and then W to micro
Watt
%% Non-PZT zone FRF summation

%FRF_sum(q,t)=sum(sum(FRF(q,t,:,:)))/TotalPatch;                    % FRF
summation for all Patches.
%FRF_sumAbs(q,t)=sum(sum(abs(FRF(q,t,:,:))));                       % FRF
summation for all Patches.
    end
    FRF(q,:)=Voltage(q,:)./((w).^2);
end
save('FRFfunction305.mat','FRF','Num_Xpatch','Num_Ypatch');
% Plotting Srarts here....
% plot(w,abs(FRF_model(1,:)));
% xlabel('Frequency(KHz)','FontSize',14,'FontAngle','italic','Color',[0 0 0]);
% ylabel('FRF_model','FontSize',14,'FontAngle','italic','Color',[0 0 0]);
figure(10)
plot(w,abs(Voltage(1,:)),'m-','Linewidth',2);hold on
plot(w,abs(Voltage(2,:)),'b--','Linewidth',2);hold on
plot(w,abs(Voltage(3,:)),'Linewidth',2,'Color',[0.3 0.8 0.8]);hold on
plot(w,abs(Voltage(4,:)),'r-','Linewidth',2);hold on
plot(w,abs(Voltage(5,:)),'k-.','Linewidth',2);hold on
```

```
plot(w,abs(Voltage(6,:)),'k-','Linewidth',2);hold on
plot(w,abs(Voltage(7,:)),'Linewidth',2,'Color',[0.1 0.8 0.1]);hold on
plot(w,abs(Voltage(8,:)),'Linewidth',2,'Color',[0.3 0.3 0.1]);hold on
plot(w,abs(Voltage(9,:)),'Linewidth',2,'Color',[0.6 0.3 0.1]);hold on

%axis ([0 200 0 0.015])
xlabel('Frequency(KHz)','FontSize',14,'FontAngle','italic','Color',[0 0 0]);
ylabel('Voltage Output (mV)','FontSize',14,'FontAngle','italic','Color',[0 0 0]);
title('Frequency Respose Function','FontSize',14,'FontAngle','italic','Color',[0 0 0]);
%legend('1K Ohm','4K Ohm','8K Ohm','12K Ohm','16K Ohm','20K Ohm','30K
Ohm','40K Ohm');
legend('100 Ohm','200 Ohm','300 Ohm','400 Ohm','800Ohm','1K Ohm','5K Ohm','10K
Ohm','20K Ohm','FontSize',8);
figure(20)
plot(w,abs(FRF(1,:)),'m-','Linewidth',2);hold on
plot(w,abs(FRF(2,:)),'b--','Linewidth',2);hold on
plot(w,abs(FRF(3,:)),'Linewidth',2,'Color',[0.3 0.8 0.8]);hold on
plot(w,abs(FRF(4,:)),'r-','Linewidth',2);hold on
plot(w,abs(FRF(5,:)),'k-.','Linewidth',2);hold on
plot(w,abs(FRF(6,:)),'k-','Linewidth',2);hold on
plot(w,abs(FRF(7,:)),'Linewidth',2,'Color',[0.1 0.8 0.1]);hold on
plot(w,abs(FRF(8,:)),'Linewidth',2,'Color',[0.3 0.3 0.1]);hold on
plot(w,abs(FRF(9,:)),'Linewidth',2,'Color',[0.6 0.3 0.1]);hold on
```

```
% plot(w,abs(FRF_sum(5,:)),'k-.','Linewidth',2);hold on
% plot(w,abs(FRF_sum(6,:)),'k-','Linewidth',2);hold on
%plot(w,abs(FRF_sum(3,:)),'Linewidth',2,'Color',[0.3 0.8 0.8]);hold on
% plot(wo,abs(V0(6,:)),'Linewidth',2,'Color',[0.3 0.8 0.1]);hold on
%axis ([0 200 0 0.015])
xlabel('Frequency(KHz)','FontSize',14,'FontAngle','italic','Color',[0 0 0]);
ylabel('|Volt/w^2|','FontSize',14,'FontAngle','italic','Color',[0 0 0]);
title('Frequency Respose Function','FontSize',14,'FontAngle','italic','Color',[0 0 0]);
legend('100 Ohm','200 Ohm','300 Ohm','400 Ohm','800Ohm','1K Ohm','5K Ohm','10K
Ohm','20K Ohm','FontSize',8);
%legend('400');
%legend('100','200','300','400');
figure(30)
plot(w,abs(P0(1,:)),'m-','Linewidth',2);hold on
plot(w,abs(P0(2,:)),'b--','Linewidth',2);hold on
plot(w,abs(P0(3,:)),'Linewidth',2,'Color',[0.3 0.8 0.8]);hold on
plot(w,abs(P0(4,:)),'r-','Linewidth',2);hold on
plot(w,abs(P0(5,:)),'k-.','Linewidth',2);hold on
plot(w,abs(P0(6,:)),'k-','Linewidth',2);hold on
plot(w,abs(P0(7,:)),'Linewidth',2,'Color',[0.1 0.8 0.1]);hold on
plot(w,abs(P0(8,:)),'Linewidth',2,'Color',[0.3 0.3 0.1]);hold on
plot(w,abs(P0(9,:)),'Linewidth',2,'Color',[0.6 0.3 0.1]);hold on
% plot(wo,abs(P0(5,:)),'k-.','Linewidth',2);hold on
```

```
% plot(wo,abs(P0(6,:)),'k-','Linewidth',2);hold on
% plot(wo,abs(P0(7,:)),'Linewidth',2,'Color',[0.1 0.8 0.1]);hold on
% plot(wo,abs(P0(8,:)),'Linewidth',2,'Color',[0.3 0.3 0.1]);hold on
%axis ([0 200 0 0.015])
xlabel('Frequency(KHz)','FontSize',14,'FontAngle','italic','Color',[0 0 0]);
ylabel('Power (\muW)','FontSize',14,'FontAngle','italic','Color',[0 0 0]);
title('Frequency Respose Function','FontSize',14,'FontAngle','italic','Color',[0 0 0]);
%legend('1K Ohm','4K Ohm','8K Ohm','12K Ohm','16K Ohm','20K Ohm','30K
Ohm','40K Ohm');
legend('100 Ohm','200 Ohm','300 Ohm','400 Ohm','800Ohm','1K Ohm','5K Ohm','10K
Ohm','20K Ohm','FontSize',8);
%legend('100 Ohm','200 Ohm','300 Ohm','400 Ohm','800Ohm','1K Ohm','FontSize',8);
%legend('300', '900', '1500', '2100', '3000', '4500', '6000');
%legend('100' , '1000', '3000', '4000', '5000' , '6000');
```